Super-enhanced stimulated Raman scattering and particle guidance in hollow-core photonic crystal fibres

Antonopoulos, Grigorios

Award date:
2006

Awarding institution:
University of Bath

SUPER-ENHANCED STIMULATED RAMAN SCATTERING AND PARTICLE GUIDANCE IN HOLLOW-CORE PHOTONIC CRYSTAL FIBRES

Submitted by Grigorios Antonopoulos
for the degree of
Doctor of Philosophy
of the University of Bath
2006

ProQuest LLC
789 East Eisenhower Parkway
P.O. Box 1346
Ann Arbor, MI 48106-1346

ABSTRACT

This thesis describes the application of hollow-core photonic crystal fibres (HC-PCFs) in super-enhanced gas-based stimulated Raman scattering (SRS) and laser-induced particle guidance. In HC-PCFs light propagates in an air-core (by means of photonic bandgap guidance), in a well-confined mode and over very long distances. Compared to conventional techniques, this brings about a huge improvement in the figure-of-merit for linear and nonlinear light/matter interactions inside the fibre core.

For such applications, changing the refractive index contrast of the fibre is sometimes required and this has an effect on the transmission properties of the fibre. This effect is experimentally studied and refractive index scaling of the photonic bandgap is demonstrated.

Moreover, HC-PCFs filled with hydrogen were used for SRS. A dramatic reduction in the Stokes threshold energy from previously reported results (by a factor of 10^2 for vibrational SRS and 10^6 for rotational SRS) was observed. Furthermore, a comb-like spectrum of nine purely rotational SRS bands was generated. Also, the very long interaction lengths achievable when using a HC-PCF, together with the low input power requirements, introduce a novel regime in SRS dynamics: transient SRS was observed, both theoretically and experimentally, for pulse widths far exceeding the Raman dephasing time.

Finally, the enhanced efficiency of laser-induced particle guidance in HC-PCFs is demonstrated. By calculating the magnitude of optical forces acting on the particle inside the fibre, an increase in the guidance length by six orders of magnitude is found to occur compared with other techniques.

Αφιερωμένο στους γονείς μου, Γιάννη και Μίρκα, και στον αδερφό μου, Χρήστο.

ACKNOWLEDGEMENTS

First and foremost I would like to thank Fetah Benabid for being an invaluable friend, colleague and supervisor. Fetah has been there for me literally every step of the way, in and out of the lab. Without him this thesis would simply not have been written.

My sincere gratitude goes to Philip Russell for making it possible for me to work in the Optoelectonics Group (now Photonics and Photonic Materials Centre) and for overseeing this work. I would also like to thank Jonathan Knight for all his help throughout this research.

Many people have contributed to this work. Alan George had an important part in the design of various pieces of equipment, especially the fibre cells. Tim Birks inspired the work on index scaling and also proof-read the relevant chapter. David Bird and Tom Hedley devised a valuable plane-wave method and code (used extensively in this work) for modelling bandgap fibres. Geraud Bouwmans and Brian Mangan, apart from being good friends, also fabricated some of the fibres used in the experiments. John Pottage (also a good friend) spent a lot of time proof-reading the entire thesis. To all these people I extend my sincere appreciation.

There are many other friends I made during my time in the group. Apart from those mentioned already, and in no particular order, these are: Arturo Ortigosa, Will Reeves, George Kakarantzas, William Wadsworth (who also made crucial suggestions on the index scaling experiments), Fabio Biancalana, Georges Humbert, Nicolas Joly, Sergio Leon-Saval, Caroline Malbaux, Gabriele Bolognini, Ravi Kumar, Feng Luan – to all of you, thanks for being there, it made things so much better.

Last, but definitely not least, I would like to thank Konstantinos Samartzis for being my best friend. Finally, I would like to dedicate this thesis to my family, my parents and my brother.

Contents

List of Figures

List of Tables

Chapter 1

Preface

In a hollow-core photonic crystal fibre (HC-PCF) light is guided in air, in a well-confined, good-quality, diffractionless mode over long distances. Filling the core of such a fibre with different materials opens up intriguing new possibilities for the interaction between light and matter. This thesis focuses on the study of the application of HC-PCF in ultra-enhanced light/matter interactions, such as gas-based stimulated Raman scattering and laser-induced manipulation of particles.

1.1 Historical overview

Since their first successful demonstration in the 1960's [1], optical fibres have revolutionised the field of telecommunications. They are ideal for transmission of signals as they are made of relatively cheap materials (silica glass), which are also non-conductive; thus, contrary to electric wires, they can be used without the risk of external electromagnetic interference. In addition, the attenuation rates of state-of-the-art optical fibres are now extremely low ($\sim$0.2 dB/km), easily achieving long-haul signal transmission, especially when used in combination with intermediate amplifiers.

Despite their excellent performance in the transmission of optical signals, conventional optical fibres suffer from several limitations. First, light in an optical fibre propagates in a bulk medium, glass, and so suffers form both absorption

losses (from the constituents of the glass itself and from impurities) and radiative attenuation (Rayleigh scattering from density fluctuations frozen in the fibre). Secondly, the strict geometry and refractive index profile of standard optical fibres impose a certain frequency dispersion on the propagating field that cannot be easily engineered for different requirements and applications. Finally, there has always been a desire for greater versatility in the fibre design for better performance in more specialised applications, such as high power delivery, tailored nonlinearity, sensing, high birefringence and the hosting of different materials, to mention a few. It was these motivations that finally led to the emergence of a new class of fibre, the photonic crystal fibre (PCF). In a PCF the fibre core is surrounded by a microstructured cladding, usually consisting of a periodic array of air holes in silica. Such a cladding is a two-dimensional photonic crystal, hence the term PCF. When the core index of a PCF is higher than that of the cladding, waveguiding still takes place via total internal reflection at the core/cladding interface just as with step-index optical fibres. However the great versatility in the design of the PCF structure gives the fibre a wealth of new properties that have found many interesting applications. Moreover, most PCFs are made of a single material (silica) and this makes the engineering of the fibre properties much easier than for conventional optical fibres.

The idea of a hollow-core photonic crystal fibre first emerged in the early 1990's [2], when it was realised that light can be confined in air by means of a photonic bandgap (PBG). This is a frequency region where light cannot propagate in a photonic crystal. It was a new departure in the field of optics, as it introduced the idea of bandgaps for light propagating out of the periodicity plane of the photonic crystal. Until that time, the existence of frequency stop-bands in periodic dielectric structures was only predicted for in-plane propagation in photonic crystals with a strong refractive index contrast [3, 4, 5]. In HC-PCFs, the air core is surrounded by a two-dimensional periodic cladding that exhibits photonic bandgaps for certain ranges of the propagation constant of the core modes; light is, thus, confined in the air core. Moreover, it was theoretically demonstrated that photonic bandgaps for out-of-plane propagation can exist in structures with such a low refractive index contrast as silica and air [6]. This finally led to the fabrication of the first working HC-PCF in 1999 [7].

HC-PCFs are interesting in many ways. On a fundamental level, there is basic scientific interest in the photonic bandgap that the fibre exhibits. Furthermore,

in a HC-PCF light is guided in air; this can potentially mean low levels of nonlinearity, delivery of high-power pulses and the transmission of frequencies that cannot propagate in glass. It also offers diffractionless propagation of light in air in a good quality well-confined mode over distances that can now reach the order of kilometres [8]. This opens up a new 'highway' for light/matter interactions, both linear (such as laser-induced guidance of atoms and particles [9, 10]) and nonlinear (for example, gas-based nonlinear optics [11, 12]).

1.2 Outline of the thesis

Chapter 2 is a brief introduction to HC-PCF. It is not meant to be a thorough overview, but rather to emphasize the novelty of the bandgap waveguiding mechanism and the usual means of describing and studying such fibres through plots of bandgap fingers and the density-of-states. The last section of the chapter shows how the availability of a low-loss, small-core waveguide in which light propagates in air can offer a significant enhancement in the linear and nonlinear interaction between light and matter inside the waveguide compared with other techniques.

Chapters 3-6 present original work done either entirely by the author or in which the author had a major contribution.[1] When replacing the air in a HC-PCF with another material for applications in light/matter interactions, it is useful to know what happens to the transmission properties of the fibre. Chapter 3 deals with the experimental investigation of refractive index scaling in photonic bandgap fibres. It shows that by reducing the index contrast of a HC-PCF from its initial silica/air value, the fibre bandgap shifts in frequency, obeying a simple refractive index scaling law. At the same time, photonic bandgap guidance in liquid is experimentally demonstrated.

Chapters 4, 5 and 6 present results that make use of the high figure-of-merit (FOM) of a HC-PCF for light/matter interactions. Chapter 4 deals with vibrational stimulated Raman scattering (SRS) in a HC-PCF that has a wide transmission spectrum and is filled with hydrogen gas. Very low-threshold generation of SRS bands is demonstrated, while the behaviour of these bands with propagation distance and input pump power is investigated.

[1] Appendix D on page 127 presents a list of the author's publications

Chapter 5 focuses on purely rotational stimulated Raman scattering (SRS) in a bandgap-guiding hydrogen-filled HC-PCF with a narrower transmission spectrum than the previous fibre. A comb-like rotational SRS spectrum is generated at extremely low threshold. The effect of the very long interaction length and low input power on the temporal dynamics of the SRS process is investigated. Also the transmission spectrum of the fibre is used to selectively excite individual SRS bands.

Chapter 6 presents calculations of the optical forces on a dielectric particle that is levitated in air and guided inside a HC-PCF. The results are compared with experimental data and they demonstrate the very long particle guidance lengths attainable inside a HC-PCF.

Finally, Chapter 7 is a summary of the main results of the thesis and a look at potential future work that these results might stimulate.

Chapter 2

Introduction to hollow-core photonic crystal fibres

2.1 Waveguiding mechanisms

2.1.1 Photonic bandgap guidance

Index-guiding optical fibres

In a step-index fibre light is guided in the core by means of total internal reflection (TIR) at the core/cladding interface, as can be seen in Figure 2.1. TIR is possible because the refractive index of the doped-silica core, n_{core}, is slightly higher than the index of the cladding, $n_{cladding}$. The critical angle θ_{cr} for total internal reflection is given by [13]:

$$\theta_{cr} = \sin^{-1}\left(\frac{n_{cladding}}{n_{core}}\right) . \tag{2.1}$$

A photonic crystal fibre (PCF), on the other hand, is an optical fibre with a microstructured cladding, usually consisting of a periodic array of air holes on a silica background. This cladding forms a two-dimensional photonic crystal (PC). The distance between two successive holes in the PC cladding is called the pitch (symbol Λ). If the fibre core is also made of silica, then the fibre guides light

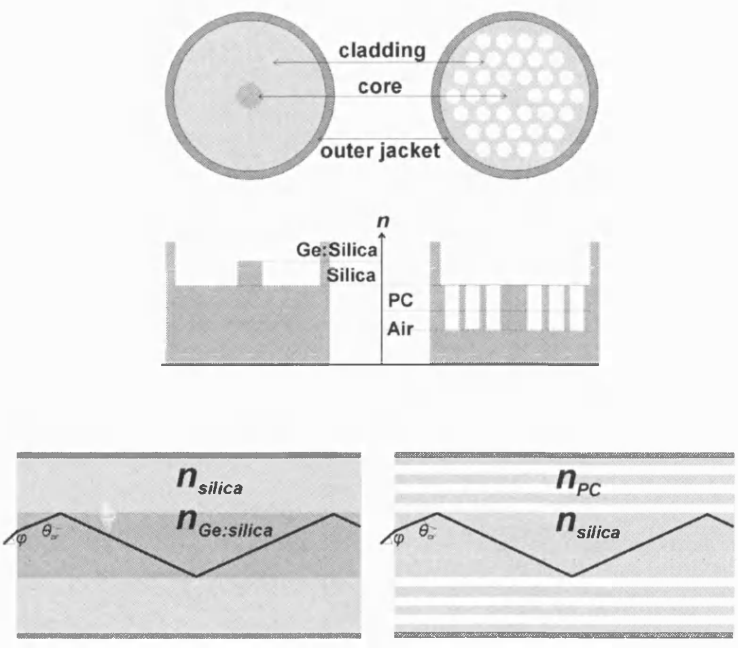

Figure 2.1: Schematic comparison between a step-index fibre and an index-guiding PCF. Top: transverse cross-sections of the fibres. Centre: index profiles. Bottom: guidance by TIR

by TIR, just like the step-index fibre described previously. Now TIR takes place at the interface between the silica core and the cladding which is made of silica and air and so has an effective index lower than the core. Fibres that guide light by means of TIR, such as step-index optical fibres and solid-core PCFs, will be henceforth called index-guiding fibres. A schematic comparison between a step-index fibre and an index-guiding PCF with a PC cladding comprising a triangular array of holes is shown in Figure 2.1. The range of structures and air-filling fractions in the fibre cladding that can be realised in PCFs gives them unique properties that have found a wide range of applications since the fabrication of the first working PCF [14]. Due to the dispersion of the effective cladding index $n_{eff}(\omega)$, PCFs can be fabricated that are endlessly single-mode, that is, they can be single-mode at all frequencies [15]. Furthermore, PCFs with novel dispersion have been fabricated [16], which exhibit notable nonlinear properties [17]. Finally, other useful geometries have produced fibres with interesting properties and applications (see, for example, [18, 19]).

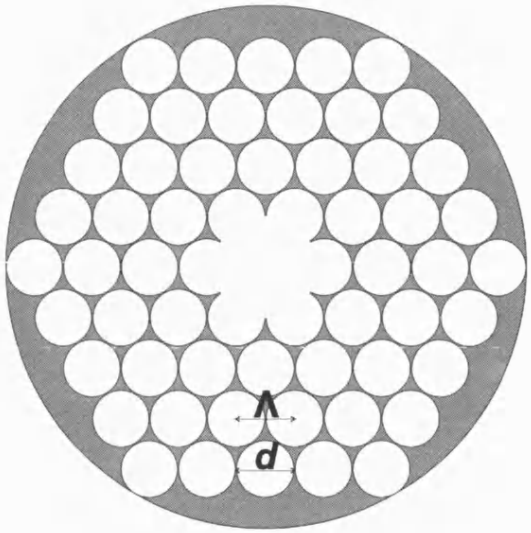

Figure 2.2: Schematic of the transverse cross-section of a hollow-core photonic crystal fibre

Hollow-core photonic crystal fibres

It is impossible to make an index-guiding optical fibre with a hollow core. The reason is that, for TIR to take place, the core index must be higher than the cladding index. The hollow-core photonic crystal fibre (HC-PCF) overcomes this limitation by using a completely novel waveguiding mechanism. In a HC-PCF, just as in an index-guiding PCF, the cladding consists of a two-dimensional photonic crystal (Figure 2.2). In most HC-PCFs the whole structure is made of silica and air. In this case, however, the PC cladding exhibits photonic bandgaps (PBGs), that is, finite frequency regions where light cannot propagate in the cladding. If these PBGs extend to a region where light can propagate in air, then it is possible to trap guided modes in a hollow core surrounded by this photonic crystal cladding. This type of waveguiding is called photonic bandgap-guidance. Light guided in the hollow core results from constructive interference after multiple Bragg reflections in the periodic layers of air and silica in the cladding.

A propagation diagram for an infinite two-dimensional photonic crystal consisting of a triangular array of air holes is drawn in Figure 2.3. Here, k_0 is the free-space wavenumber and k_z the axial component of the wavenumber. By solving the vector wave equation for this structure, in the case where light propagates out of the periodicity plane, full bandgaps were found to occur [6]; these PBGs could

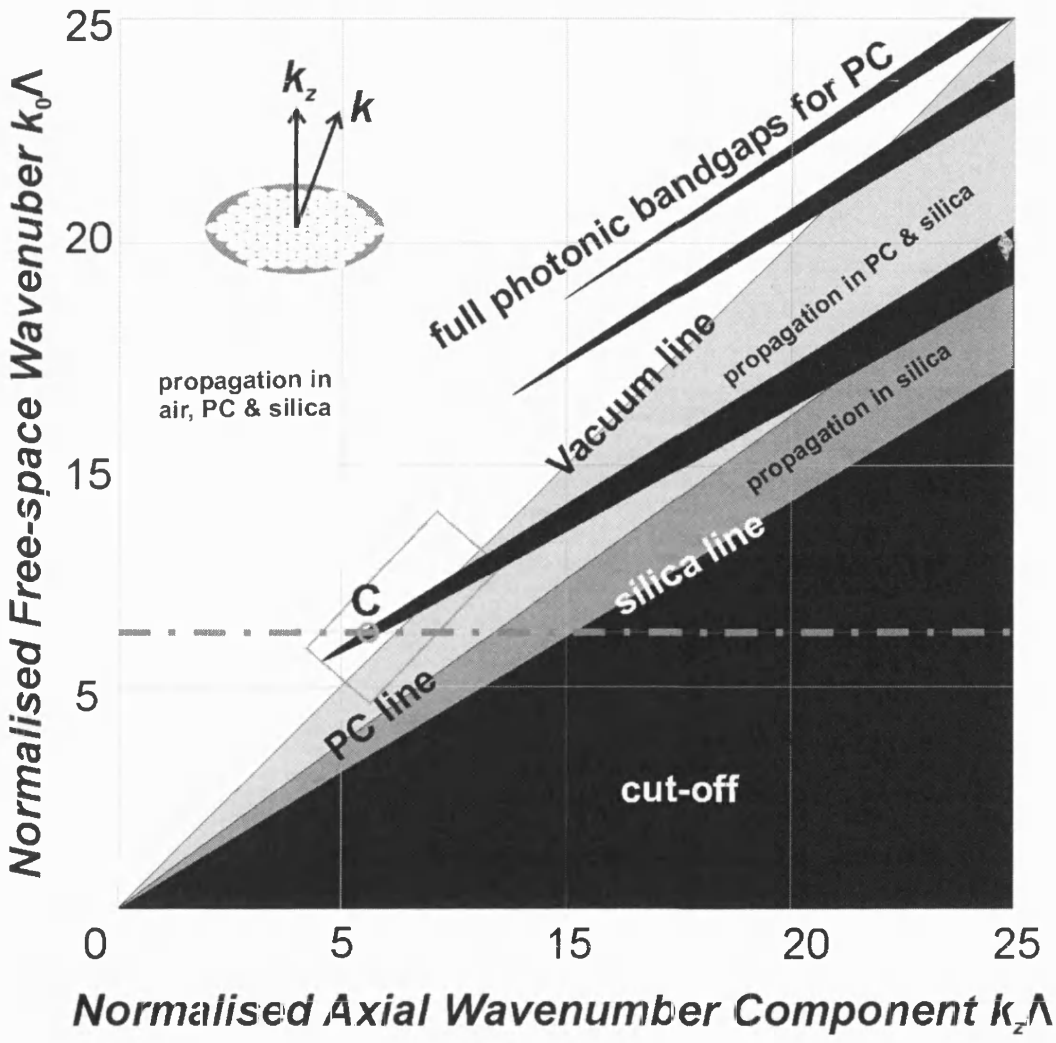

Figure 2.3: Bandgap finger plot for an infinite two-dimensional photonic crystal (like the finite one shown schematically at the top left). The small circle C marks a region where bandgap-guidance in a hollow core is possible

extend above the vacuum dispersion line $k_z\Lambda = k_0\Lambda$. Due to the shape of the PBGs on this propagation diagram, the latter is usually called a "bandgap finger plot". On this diagram the guided modes of an index-guided PCF, formed by replacing the central air hole with a solid silica rod, would be located in the region confined by the silica line $k_z\Lambda = k_0 n_{silica}\Lambda$ and the PC line of a material with the effective index of the cladding (the PC curve is shown here as a straight line for simplicity).

A hollow core, on the other hand, can be formed by omitting a number of capillaries that form the photonic crystal cladding, like the structure of Figure 2.2 (see also Section 2.4 for the fabrication of HC-PCFs). Such a low-index "defect" can support modes with axial wavevectors (called propagation constants, β)[1] within a region of the cladding bandgap above the air line (like the small circle C in Figure 2.3, for example). In this region light can propagate freely in air but is switched off in the cladding and is, therefore, confined in the hollow core; that is, photonic bandgap waveguiding occurs.

Density-of-states plots

It is very often useful to know not just the position of the PBGs of a photonic crystal cladding, but also the number of available modes that the cladding can support. Graphically this is done by density-of-states plots. Density of states (DOS) is the number of modes with propagation constants between the values β and $\beta + \delta\beta$. At the location of the bandgap the DOS is zero. Mr Tom Hedley and Prof David Bird have devised a modified plane-wave method for solving the vector wave equation for out-of-plane propagation (Equation 3.1 on page 27) and have implemented a code for generating DOS plots [20, 21]. One such DOS plot generated using this plane-wave method and code is shown in Figure 2.4. The 2-D crystal consists of a triangular array of air holes (diameter d) in silica. The crystal pitch is Λ and the ratio d/Λ is 0.99. The DOS plot axes are $k_0\Lambda$ and $(\beta - k_0 n_{core})\Lambda$ so that the plotted area focuses on a narrow strip along the core index line, similar to the rectangle shown on the plot of Figure 2.3.

[1] At a fixed frequency $\beta = k_z$. For the sake of simplicity, from now on both β and k_z will be called "propagation constants" and will be written as β

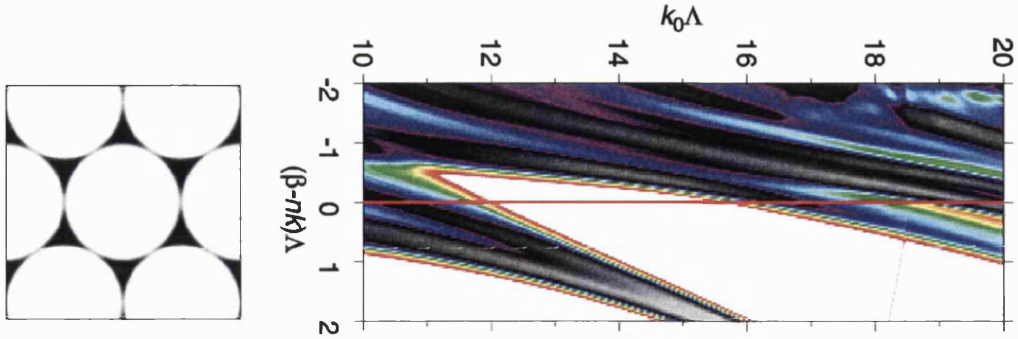

Figure 2.4: DOS plot (right) of a 2-D photonic crystal structure consisting of a triangular array of air holes in silica with $d/\Lambda = 0.99$ (left). In the DOS plot different colours represent different densities, while the white region represents a complete bandgap. The horizontal red line is the vacuum line $\beta = k_0$

2.1.2 Waveguiding by low density-of-states

A photonic bandgap is not always necessary to achieve guidance in an air-core PCF. A type of HC-PCF fabricated at the University of Bath and first reported in [11] can guide light in a hollow core even though the surrounding PCF cladding does not exhibit any photonic bandgaps at all. The fibre is shown in Figure 2.5. The cladding consists of an array of thin silica strands in air that form a Kagomé lattice. The DOS plot for the cladding of this Kagomé fibre is also shown in the same figure. Instead of a full PBG, this structure possesses an extended frequency range (26-42 $k\Lambda$) where the DOS is very low. This low-DOS range corresponds very well with the recorded transmission spectrum of the fibre, also shown in the figure. This indicates a possible correlation and this type of waveguiding can be called low density-of-states (LDOS) waveguiding. Furthermore, both experiments and calculations have shown well-confined core modes in the LDOS region of the Kagomé fibre [20].

This fibre has a very wide transmission bandwidth compared with PBG-guiding HC-PCFs; it spans almost 900 nm of wavelength (Figure 2.5(a)) and can be used in applications requiring transmission of a wide range of frequencies [11], as will be shown in Chapter 4. The lowest attenuation rate achieved with LDOS-guiding fibres has so far been about 0.3 dB/m.

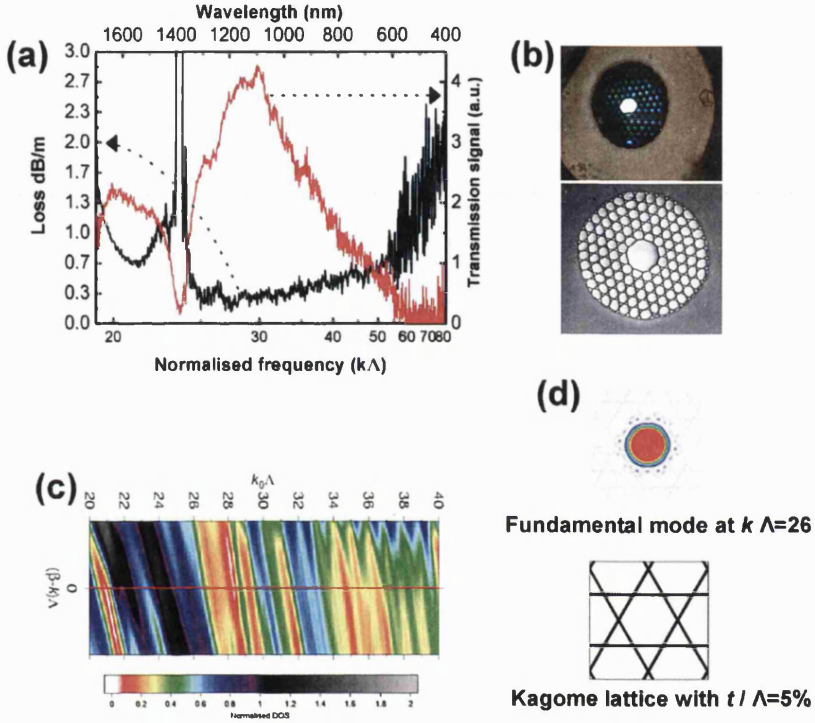

Figure 2.5: Experimental transmission spectrum (a) of the Kagomé fibre shown in (b). The wide transmission band accounts for the white colour of the core mode when the fibre is illuminated with white light as in the top right picture. The calculated DOS plot is shown in (c) for the structure of figure (d), where the calculated intensity profile of the fundamental mode is also shown. The modelled structure consists of silica webs of thickness t and the ratio t/Λ is 5%

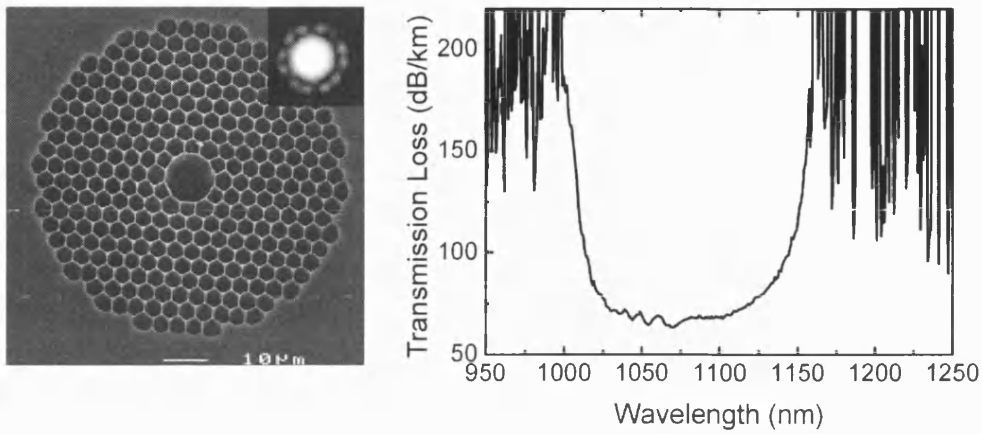

Figure 2.6: Electron micrograph of the end-face of a HC-PCF (fabricated at the University of Bath) and its attenuation spectrum (right). Also shown is the measured intensity profile of the fundamental guided core mode (inset picture)

2.2 Modal properties

2.2.1 Core modes

Guided modes are generated in a HC-PCF by introducing an air hole in a photonic crystal cladding that has PBGs extending above the air line. Different cladding structures will, therefore, produce different bandgap locations, which results in different transmission bands. Figure 2.6 shows a HC-PCF together with its transmission spectrum and the intensity profile of its fundamental (lowest-order) mode.

Qualitatively, the guided modes of a HC-PCF can be approximated to the modes of a perfectly reflecting capillary. These are described as transverse electric (TE_{nm}), transverse magnetic (TM_{nm}) and hybrid (HE_{nm}) modes. The field distributions of these modes are proportional to Bessel J functions. The indices nm stand for the mth root of the Bessel function J_{n-1} [22]. TE and TM modes have their electric or magnetic field vectors respectively transverse to the direction of propagation. In the hybrid HE modes, on the other hand, all field vectors possess a longitudinal component as well. The lowest-order mode of a dielectric capillary with bore radius R_0 is the HE_{11}, which has a radial electric field distribution $E(r)$:

$$E(r) \approx J_0\left(2.405\frac{r}{R_0}\right) , \tag{2.2}$$

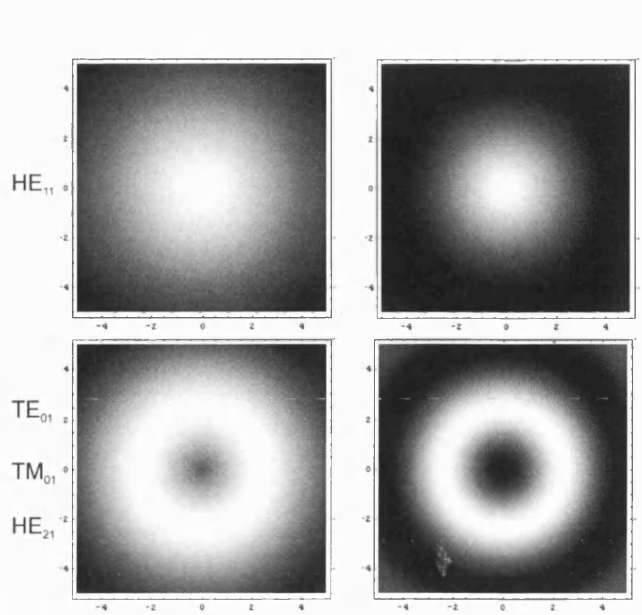

Figure 2.7: Calculated electric field (left column) and intensity distributions (right column) of the first two modes of a capillary with $R_0 = 5$ μm

with J_0 being the zero-order Bessel J function. This is found to be very similar to the fundamental mode of a HC-PCF [23]. The next higher-order modes (i.e. the degenerate TE_{01}, TM_{01} and HE_{21} modes) have a radial field distribution $E(r) \approx J_1(3.832\, r/R_0)$. The field and intensity distributions of these modes are shown in Figure 2.7.

The total number of core modes of a HC-PCF depends on the size of the core and on the range of β values spanned by the bandgap as it crosses the air line. This is illustrated in Figure 2.8. The shaded annular area in Figure 2.8(b) is the available reciprocal space for guided modes in the air core and equals $\pi(k_{tL}^2 - k_{tH}^2) = \pi(\beta_H^2 - \beta_L^2)$, where the various terms are illustrated in the figure. The reciprocal space area occupied by a single core mode is π/R_0^2, with R_0 the core radius. From these, the total number of guided core modes turns out to be [7]:

$$N_{PBG} = \frac{(\beta_H^2 - \beta_L^2)\, R_0^2}{4} \,. \tag{2.3}$$

In the above equation the 1/4 term accounts for the fact that only wavevectors with $\beta > 0$ are taken into account (propagation in the $+z$-direction).

The plane-wave method mentioned previously can also be used to give the dispersion curves $\beta(k)$ of the guided modes in the HC-PCF core, as well as the modal

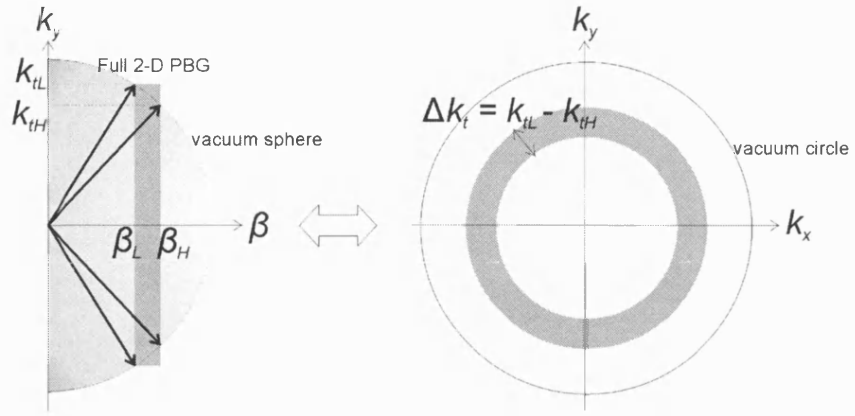

Figure 2.8: The vacuum sphere in reciprocal space (left) and the projection of the sphere on the (k_x, k_y) plane (right) for a HC-PCF with a full 2-D bandgap for the transverse wavevector $\mathbf{k_t}$

field and intensity profiles [20]. Such a dispersion curve for the fundamental core mode of a HC-PCF with a PC cladding like the one of Figure 2.2 is shown in Figure 2.9. As this is the lowest-order (highest-β) core mode with $\beta \approx k_0$, it is natural that, within the cladding bandgap, its dispersion curve will be close to the vacuum line. As the dispersion curve of the core-guided mode approaches the cladding modes (in a region like the one marked by the box on the DOS plot in the figure), light can couple into a continuum of cladding modes. However, inside the PBG there can exist another type of available mode as will be discussed in the next section.

2.2.2 Surface modes

It is well-known in solid state theory that the surface of a finite crystal acts as a defect where there are localised solutions of the electron wavefunction. These are called surface states [24]. In exactly the same manner, the interface between the photonic crystal cladding and the hollow core can support modes that are mostly concentrated on the silica region that borders the core [25]. By analogy with solid-state physics these modes are also called "surface modes".

Surface modes can have dispersion curves inside the cladding bandgap. Therefore there can be points on the dispersion plot where the guided core modes and the surface modes cross. When both modes share the same symmetry they repel each other as their dispersion lines come closer and, therefore, these crossing points are

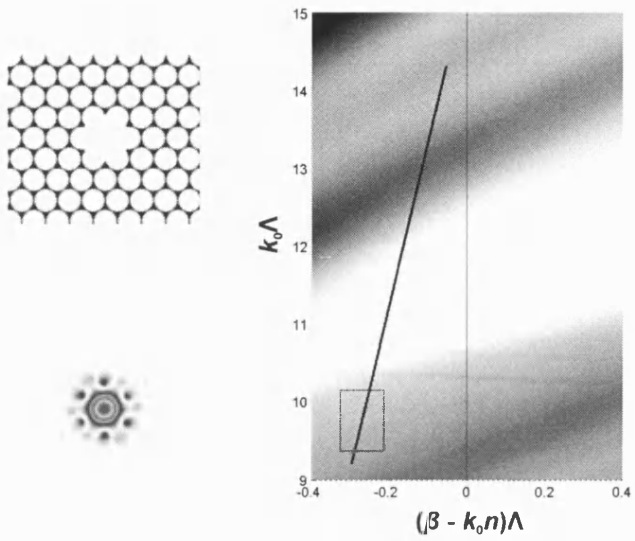

Figure 2.9: DOS plot (right) for the HC-PCF structure shown top left with the dispersion curve (black line) of the fundamental core mode. Here $d/\Lambda = 96\%$. The grey shades on the DOS plot represent different modal densities for the PC cladding, while the white region is a complete PBG. The intensity profile of the core mode (for $k_0\Lambda = 10.5$) is also shown (bottom left). The plots and figures were generated using the plane-wave method and code of [20]

referred to as "anti-crossings" (another term from solid-state physics). If there is degeneracy in β and some spatial overlap between the core and surface modes, mode coupling can occur [26], that is, transfer of energy from the core-guided mode to one of the surface modes; the latter can in turn couple into a continuum of cladding and radiation modes. In the state-of-the-art HC-PCFs this is one of the major limitations of the performance of the fibre (see Section 2.3).

Coupling to surface modes alters the dispersion curve of the core-guided mode. This is done by a process called mode splitting, which is illustrated in Figure 2.10. The blue curve shows the dispersion of an initially core-guided mode and the red curve the dispersion of a surface mode. Away from the anti-crossing region (point (a)) most of the energy is concentrated in the core mode. As the dispersion curve of the latter approaches (point (b)) the anti-crossing point, the fractioned power in the surface mode increases. At the anti-crossing point (c), the two modes are indistinguishable. After that point the initially core-guided mode has transformed into a surface mode and its dispersion curve is altered (points (d) and (e)); conversely, the initially surface-guided mode has now transformed into the core mode. These anti-crossings result in the division of the transmission

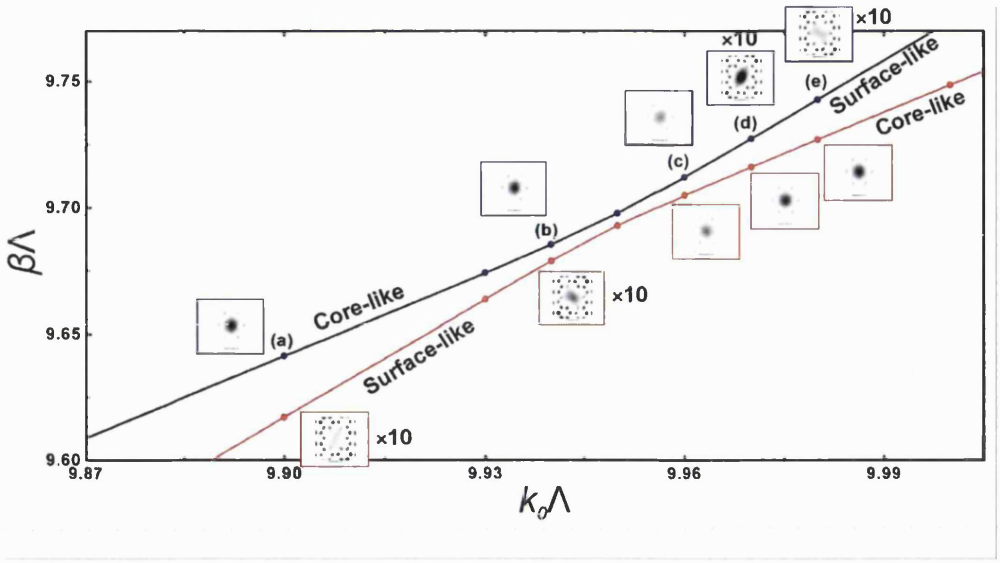

Figure 2.10: Dispersion curves of an initially core-guided mode (blue curve) and a surface mode (red curve) around an anti-crossing region. The fibre is that of Figure 2.9. The insets are the intensity profiles of the respective modes. Note that the intensity patterns of the surface-like modes are magnified by a factor of 10

spectrum of the fibre into regions of low-loss transmission separated by high-loss regions at the anti-crossing points, as can be seen, for example, at the edges of the spectrum of Figure 2.6.

2.2.3 Modal dispersion

For each guided core mode of a HC-PCF, an effective modal index can be defined as:

$$n_{mod}(\omega) = \frac{\beta(\omega)}{\omega} c \ . \tag{2.4}$$

In a purely qualitative way, the dispersion relationship $n_{mod}(\omega)$ for the fundamental mode of a HC-PCF can be described as that of a (bulk) medium that absorbs light at all frequencies apart from a single transmission line, located at the central bandgap frequency, with a bandwidth $\Delta\omega$ (Figure 2.11) [13]. As will be seen later on in Figure 5.9 on page 78, anti-crossings of the fundamental core mode with surface modes can influence the modal dispersion.

The dispersion of the propagating mode is crucial for the fibre performance,

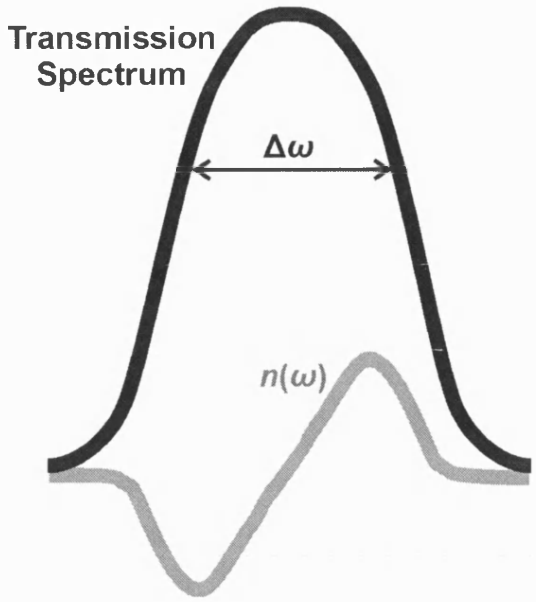

Figure 2.11: Schematic of the dispersion around a transmission band of bandwidth $\Delta\omega$

especially for the propagation of optical pulses, via the group velocity dispersion (GVD). Inside an optical fibre monochromatic fields at different frequencies will travel with different phase velocities $v(\omega) = c/n(\omega) = \omega/\beta$. A finite optical pulse consists of a range of monochromatic waves within a bandwidth $\delta\omega$ around a central frequency ω_0. The envelope of the pulse moves at the group velocity:

$$v_g(\omega_0) = \left(\frac{\partial\omega}{\partial\beta}\right)_{\omega=\omega_0} . \tag{2.5}$$

The slope of the group velocity $\partial^2\omega/\partial\beta^2$ across the available pulse bandwidth will eventually distort the pulse as the latter travels inside the waveguide. This process is called GVD. From Equation 2.4, it is obvious that GVD will depend on the dispersion $n_{mod}(\omega)$. The GVD-related quantity that is usually measured experimentally is the dispersion parameter D [27]:

$$D = \frac{\partial\left(v_g^{-1}\right)}{\partial\lambda} = \frac{\partial\beta_1}{\partial\lambda} , \tag{2.6}$$

where $\beta_1 = v_g^{-1}$ is called the group delay.

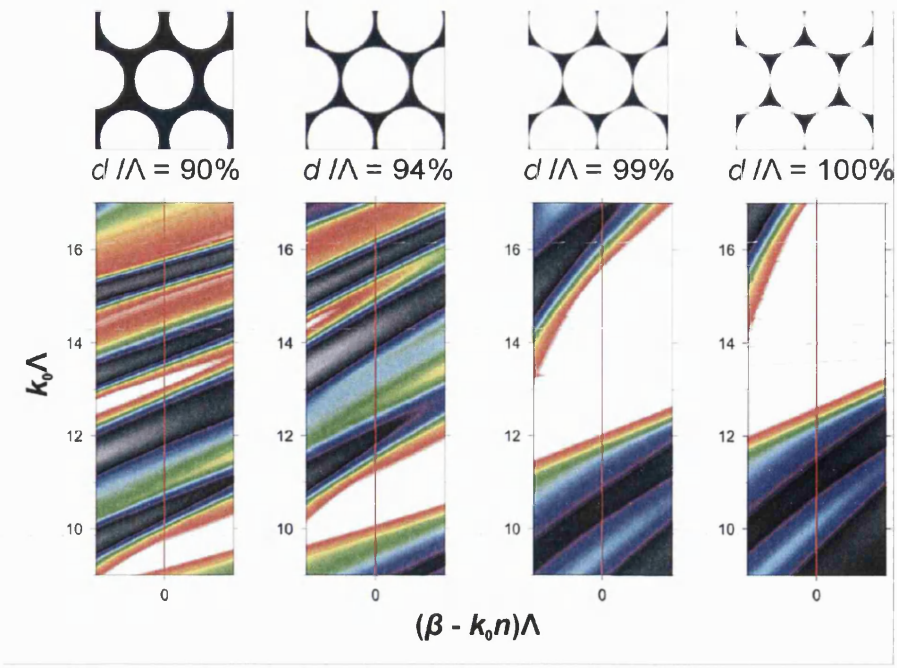

Figure 2.12: DOS plots for similar PC structures with increasing air-filling fractions, keeping the other parameters constant

2.3 State-of-the-art HC-PCFs

Conventional optical fibres have a ultimate attenuation limit of about 0.15 dB/km at the telecommunications wavelength of 1550 nm [28]. This is determined by Rayleigh scattering and absorption (mainly by transition metal ions and hydroxyl ions OH^-) in the glass and as such it cannot improve much further. In HC-PCFs, on the other hand, most of the light propagates in air where all these processes are much less pronounced. However, there are still sources of loss that relate to the bandgap-based waveguiding mechanism of HC-PCFs.

One of the requirements for low-loss guidance in a HC-PCF is that the photonic bandgap should be wide enough so as to prevent coupling of power into the cladding modes. It was realised that the size of the bandgap depends on the cladding geometry and air-filling fraction. Figure 2.12 shows the effect of the air-filling fraction of the PC structure on the generated PBGs [29]. As the ratio d/Λ increases, the bandgaps become wider. Other smaller bandgaps that occur at higher frequencies for smaller air-filling fractions disappear as the latter increases. The fact that the bandgap still grows wider for the unrealistic case of

$d/\Lambda = 1$ indicates that it is generated from the glass features at the interstitials between the air holes. It was actually found that an increase in d/Λ from 0.94 to 0.96 doubles the bandgap bandwidth [29]. Moreover, a triangular array of rounded hexagons (as in Figure 2.6) was found to result in even higher air-filling fractions than circular holes [25]. It was these findings and an optimisation of the fabrication process that led to the dramatic drop in the losses of HC-PCFs down to 1.7 dB/km [8].

There is still, however, the problem of indirect leakage from the core by the coupling of power from the core mode to surface modes. This coupling can be facilitated by scattering at the inner surface of the fibre core due to imperfections and surface roughness. Some of these imperfections have thermodynamic origins and cannot be eliminated, setting a lower limit to the ultimate performance of a HC-PCF (even though this limit is still better than conventional fibres and can theoretically be as low as 0.03 dB/km [30]).

Improved fibre design can minimise the spatial overlap of the guided core mode with the surface modes. The overlap constant varies roughly as the inverse cube of the core diameter. Larger cores have already led to significant reduction in losses [8]. A thicker core/cladding boundary relative to the boundaries within the cladding was also found to minimise the coupling [30]. Finally, the operating wavelength can affect the HC-PCF performance. The attenuation due to surface mode coupling decreases with increasing wavelength as $\propto \lambda^{-3}$, while the bulk silica absorption increases at wavelengths further into the IR due to material absorption; there is, thus, an optimum operation wavelength and at this wavelength the losses ($\sim$0.13 dB/km) can potentially be better than conventional fibres.

2.4 HC-PCF fabrication

The fabrication of silica-based HC-PCFs, just like index-guiding PCFs, is carried out by the stack-and-draw process [14]: the same structure as the microstructured fibre but on a macroscopic scale (typically 1 m long and a few centimetres diameter) is made by manually stacking silica capillaries and/or rods. A silica jacket can be used to enclose the stack. On a fibre drawing tower, this stack is heated above the glass transition temperature of silica (about 2000°C) and drawn

into preforms of a few millimetres diameter. Pressure can be applied to maintain or alter the air-filling fraction during the drawing process according to the desired end-result. In a similar manner, the preform is subsequently drawn down to the final fibre (up to about 200 μm diameter). At the final stage of the fibre drawing process the fibre is coated using a polymer coating.

2.5 Applications of hollow-core photonic crystal fibres: efficient light/matter interactions

Nonlinear interactions: gas-based nonlinear optics in a HC-PCF

The efficient nonlinear interaction between laser light and matter requires long interaction lengths, high field intensities and a transverse beam profile of good quality. Any experimental device or scheme used for such processes can be characterised by a figure-of-merit (FOM), which gives a measure of the efficiency of the interaction between light and matter. The dimensionless FOM (normalised to the operating wavelength λ) can be written as:

$$\text{FOM} = \frac{L_{eff}}{A_{eff}} \times \lambda \ , \tag{2.7}$$

with L_{eff} the effective interaction length and A_{eff} the effective area of interaction.

Now consider a free-space laser beam tightly focused onto a volume of nonlinear material as, for example, in a stimulated Raman scattering (SRS) experiment. The small effective area at the focal point results in a high beam intensity. However, the effective length for the nonlinear interaction will be severely limited by the strong diffraction of the tightly focused beam. For a Gaussian beam the interaction length can only be twice the Rayleigh range $z_R = \pi w_0^2/\lambda$ (with w_0 the beam waist radius at focus). From the definition of FOM, it is clear that the increase of the beam intensity at focus will be counter-balanced by an equal decrease in the interaction length.

A way of increasing the FOM is to place the nonlinear material in the core of a hollow waveguide. This can provide high beam intensities (through the tight

confinement of the beam in the waveguide core) and long interaction lengths. Dielectric capillaries filled with nonlinear gases have been used for this purpose [31]. In this method the beam intensity can be further increased by decreasing the size of the capillary bore. Furthermore this technique provides a good-quality beam profile when the light is coupled into the fundamental mode of the capillary.

However this technique suffers from a fundamental limitation: the dielectric capillary is an intrinsically leaky waveguide for light, with an exponential loss rate for the electric field that increases with the inverse of the cube of the bore radius. For the lowest-loss mode supported by such a dielectric capillary (HE_{11}), this loss rate is [22]:

$$\left(\frac{u_{11}}{2\pi}\right)^2 \frac{\lambda^2}{R_0^3} \frac{n^2+1}{2\sqrt{n^2-1}} , \tag{2.8}$$

with R_0 being the bore radius of the capillary and n the refractive index of the dielectric material. u_{11} is the first root of the equation $J_0(u_{11}) = 0$ (with J_0 the zero-order Bessel function) and equals 2.4. Thus the FOM (Equation 2.7) increases linearly with the bore radius:

$$\mathrm{FOM}_{capillary} = \frac{6.8\, R_0 \sqrt{n^2-1}}{\lambda\, \pi\, (n^2+1)} . \tag{2.9}$$

The effective interaction length is taken here as the inverse of the exponential loss rate. A schematic representation of the limitations of these techniques is shown in Figure 2.13(a).

The ideal host of nonlinear gases would be a lossless single-mode hollow waveguide. The HC-PCF comes close to this ideal case, with a FOM that is only limited by the fibre loss rate. If the exponential loss rate is α, the FOM of the HC-PCF becomes:

$$\mathrm{FOM}_{HC-PCF} = \frac{\lambda}{\pi R_0^2\, \alpha} . \tag{2.10}$$

The loss rate of HC-PCF has dramatically decreased in recent years to about 1.7 dB/km [8]. Figure 2.13(b) shows a comparison between the FOM of a free-space beam, a hollow capillary and HC-PCFs with different loss rates at a wavelength of 532 nm. For a HC-PCF with a loss rate of 1.7 dB/km and a core radius of 5 μm, the FOM can be higher by a factor of 10^7 than the FOM of a dielectric capillary with the same bore radius. This results in a whole new regime in the study of nonlinear interactions between light and matter. In the experiments described in Chapters 4 and 5, the use of a hydrogen-filled HC-PCF resulted in

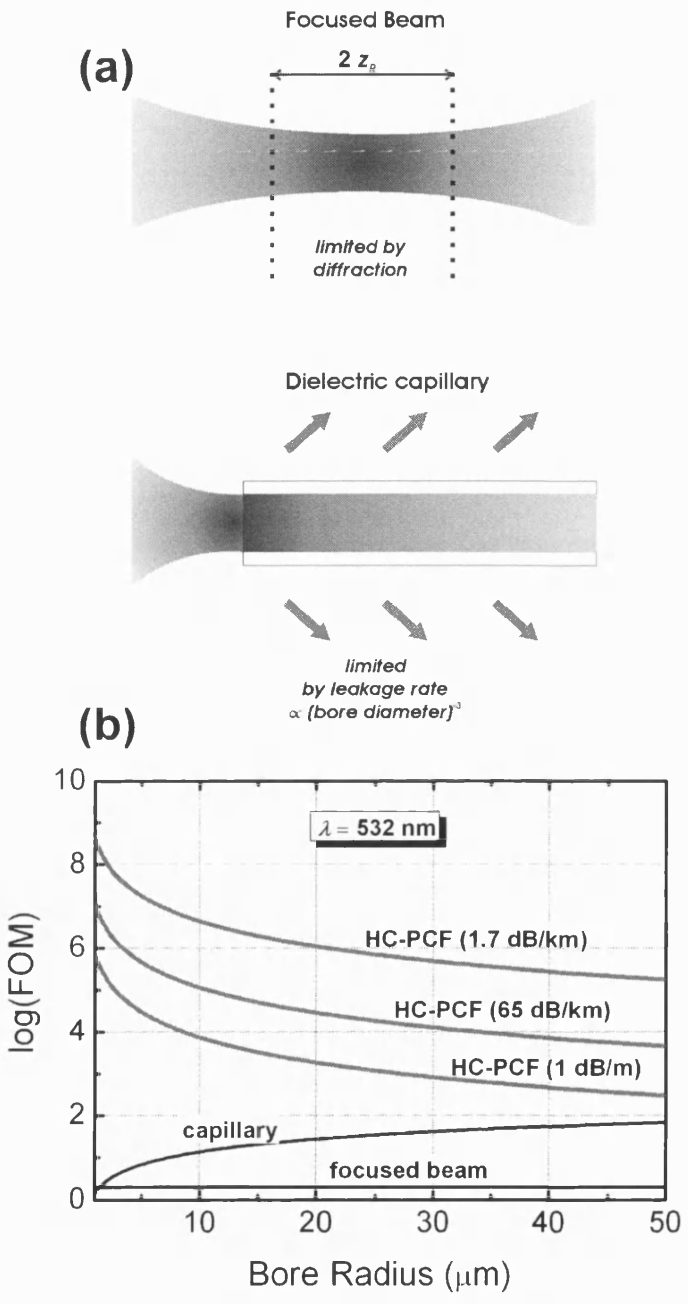

Figure 2.13: (a) Factors that limit the FOM in the case of a focused free-space beam (top) and a beam coupled into one of the modes supported by a dielectric capillary (bottom). (b) Comparative plot of the FOM of the different SRS techniques

a reduction of the threshold energy for SRS up to a factor of 10^6 compared to other conventional techniques. The other attenuation rates for HC-PCF shown in Figure 2.13(b) correspond to the fibres used in those chapters: 65 dB/km is the lowest attenuation of the bandgap HC-PCF (Figure 2.6) used for hydrogen-based SRS in Chapter 5; while 1 dB/m is the loss rate of the Kagomé HC-PCF (Figure 2.5) used in Chapter 4, again for SRS in hydrogen.

Mention should also be made to multiple-pass techniques that can also enhance the nonlinear interaction by increasing the effective length. For example the use of a gas-filled multiple-pass Fabry-Pérot cavity (FPC) in [32] produced extremely low-threshold SRS due to the significant intracavity intensity enhancement of the FBC. This even led to the first demonstration of a CW Raman laser in H_2 [33]. Efficient though it is, this technique suffers from some important limitations: firstly, the pump laser frequency must be kept tightly locked to the very sharp resonant frequency of the cavity. Also, the Stokes conversion efficiency remained very low (<5%). Finally, efficient conversion is limited to a single SRS frequency because of the doubly-resonant design of the cavity.

Linear interactions: laser-induced particle guidance and trapping

The use of optical forces to trap and guide dielectric particles was first demonstrated by Ashkin in 1970 [34] and, since then, manipulation of particles by means of radiation forces has found a variety of applications. These range widely from trapping and manipulation of biological particles such as cells, bacteria and viruses [35] to surface patterning and microengineering [36, 37] and atom trapping [38].

The radiation forces on a particle result from the momentum transfer from the light beam to the particle. They are traditionally divided into forces acting along the beam axis (axial or scattering forces), which are used for particle guidance and transportation; and forces acting in a direction transverse to the beam axis (gradient or radial forces) which are used for trapping the particle radially near the intensity maximum. The magnitude of the scattering forces depends linearly on the laser beam power and so the latter has to remain high enough throughout the whole distance over which the particle is to be transported. The gradient forces, on the other hand, depend on the transverse intensity gradient of the laser

beam. The ideal configuration would offer a tight transverse confinement and a steep intensity gradient of the beam over a long distance – the same requirements as for nonlinear light/matter interactions discussed in the previous section.

Therefore, the techniques employed for the laser guidance of particles are similar to the ones used in gas-based nonlinear optics: particles are either illuminated in free space by focused laser beams or inside dielectric capillaries [36, 37]. Of course these techniques suffer from a low FOM, which results in short effective lengths for guidance and trapping. The HC-PCF may again be the solution: in Chapter 6 calculations of the optical forces on dielectric particles guided inside a state-of-the-art HC-PCF show that a $\times 10^6$ increase in the effective guidance length.

Effect of refractive index contrast

All the applications mentioned above require filling the air core of the HC-PCF with some other material. If all the air in the fibre is replaced by a material of higher refractive index, there will inevitably be a change in the transmission properties of the fibre. If this material is a low-index gas – as will be the case in Chapters 4 and 5, where the fibre is filled with hydrogen gas – the change in the index contrast of the fibre structure is negligible. However, different applications may induce a greater change in the refractive index contrast of the HC-PCF. The following chapter will experimentally investigate the change in the transmission properties of HC-PCFs, in which the index contrast is lowered significantly by replacing the air in the fibres with heavy water.

2.6 Summary

HC-PCF offer the unique possibility of waveguiding optical fields in air over long distances. This is done by confining light in a hollow core either by means of a photonic bandgap or by low density-of-states. With today's low attenuation rates new opportunities open up for the study of light/matter interactions inside the core of the fibre: the relative figure-of-merit in a HC-PCF can be up to 10 million times higher than other conventional techniques. Chapters 4 and 5 explore SRS

generation in hydrogen-filled HC-PCFs, while Chapter 6 explores laser-induced particle guidance inside such fibres. Of course, in such applications attention should always be paid to the effect that a refractive index change may have on the transmission properties of the HC-PCF; this is experimentally investigated in Chapter 3.

Chapter 3

Transmission properties of hollow-core photonic crystal fibres: experimental demonstration of refractive index scaling

This chapter presents the first experimental demonstration of refractive index scaling in photonic bandgap fibres.[1] Bandgap-guiding HC-PCFs were filled with heavy water and, thus, had their refractive index contrast reduced from its original value. Since HC-PCFs can be used for enhanced light/matter interactions, as discussed in the previous chapter, it is important to look at what happens to the fibre transmission properties when the index contrast is reduced. The transmission spectra of the liquid filled PCFs were found to be shifted in frequency; this shift showed good agreement with a recently derived index scaling law for bandgap fibres.

[1]The work presented in this chapter was carried out by the author and has been published in [39, 40]

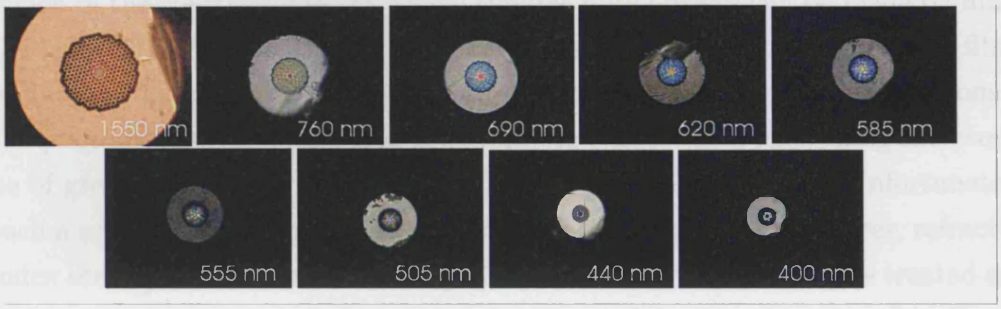

Figure 3.1: A hollow core PCF with an initial bandgap centred around 1550 nm is tapered so as to preserve the fibre structure and only decrease its scale. The pictures show optical micrographs of the cross-sections of the fibre – illuminated from below with white light – at different stages of the tapering process. The pictures also show the new bandgap centre for the tapered structure as predicted by the length scaling law. In the last image no visible core mode was observed. The pictures are courtesy of Dr Tim Birks

3.1 Introduction

One of the properties of photonic bandgap fibres that is extremely useful in the area of fibre design is the so-called length scaling law. This derives from the vector wave equation for the transverse field distribution $\mathbf{h}(\mathbf{r})$ in the fibre [41]:

$$[\nabla_\perp^2 + k^2 n_0^2(\mathbf{r}) + \nabla_\perp \times \nabla_\perp \ln n_0^2(\mathbf{r}) \times] \, \mathbf{h} = \beta^2 \, \mathbf{h} \; , \tag{3.1}$$

where k is the free-space wavenumber, $n_0(\mathbf{r})$ the radial (transverse) distribution of the refractive index of the structure, β the propagation constant of the mode and $\nabla_\perp = \hat{\mathbf{x}}\frac{\partial}{\partial x} + \hat{\mathbf{y}}\frac{\partial}{\partial y}$ the transverse Laplacian operator. According to this law, if we change the cladding pitch Λ, any previously obtained solution of Equation 3.1 will be replicated as long as $k\Lambda$ remains constant [42]. In terms of fibre fabrication this means that the bandgap frequency of any given PCF can be shifted to a different frequency by changing the length-scale of the whole structure (but otherwise keeping the structure unaltered). This has proved extremely useful in designing bandgap fibres operating at different frequencies (as shown, for example, in Figure 3.1).

However, there has recently been an increasing interest in bandgap fibres made from materials other than silica and air, the usual materials of most common HC-PCFs. For example, high index glasses can be used for guidance in the IR

region of the spectrum [21, 43], while tunable fibre devices can be made by filling the holes of a PCF with liquid crystals [44]. All these applications require fibres of different index contrasts between the high and low refractive index regions of the photonic crystal cladding of the fibre. A refractive index scaling law would be of great importance in this emerging field of fibre technology. Unfortunately, such a scaling law cannot be obtained by using Equation 3.1. However, refractive index scaling laws can be obtained [41], if the electromagnetic field is treated as a scalar quantity as we shall see in the following section: these laws can describe the evolution of the bandgap when the refractive index contrast of the fibre changes. Apart from the previously mentioned applications, index scaling laws can be of great value for applications in efficient light/matter interactions in HC-PCFs, where the latter are filled with other materials, (for instance, nonlinear gases).

3.1.1 Refractive index scaling laws

In the scalar approximation the last term of the left-hand side of Equation 3.1 can be neglected [41]. The wave equation for the scalar field distribution $\Psi(x, y)$ is then given by:

$$\nabla_{\perp}^2 \Psi + (k^2 n_0^2 - \beta^2)\Psi = 0 \ . \tag{3.2}$$

This is strictly valid for very small index contrasts. The question may arise whether such contrasts can actually produce bandgaps. It is well known that a strong index contrast is needed in order to have bandgaps for waves travelling in the plane of periodicity [5]. This results in a strong contrast in wavevector between the high and low index regions of the photonic crystal. However, the situation is different for bandgap-guiding PCFs, where the propagation is out of the plane of periodicity. In this case most of the wavevector is consumed by the longitudinal component β; this means that there can be a strong contrast in the transverse component of the wavevector even for small index contrasts as schematically shown in Figure 3.2. This is sufficient to generate bandgaps for out-of-plane propagation. To illustrate this, the contrast between the transverse wavevector components in the two materials k_{t1} and k_{t2} is written as:

$$\frac{k_{t1}}{k_{t2}} = \frac{\sqrt{(kn_1)^2 - \beta^2}}{\sqrt{(kn_2)^2 - \beta^2}} \ . \tag{3.3}$$

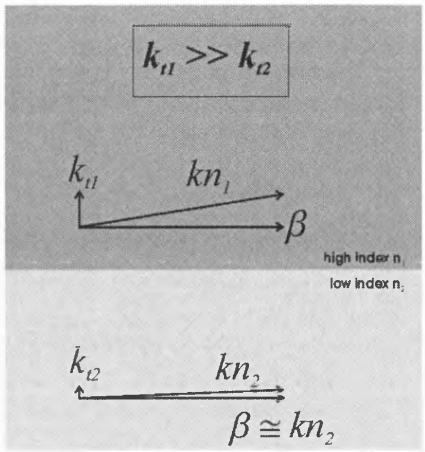

Figure 3.2: A schematic representation showing how a strong contrast in the transverse component in wavevector can occur when β is close to kn_2

For $\beta \cong kn_2$ this contrast in wavevector can be arbitrarily large even for small index contrasts. Here n_1 and n_2 are the high and low refractive indices of the PCF cladding respectively.

Using Equation 3.2, scaling laws for refractive index contrasts were derived [41]. In particular, it was found that the photonic states of a bandgap-guiding PCF scale so that the quantities:

$$\begin{aligned} v^2 &= \Lambda^2 k^2 (n_1^2 - n_2^2) \\ w^2 &= \Lambda^2 (\beta^2 - k^2 n_2^2) \end{aligned} \quad , \tag{3.4}$$

remain invariant when Λ, k, n_1 or n_2 vary. These two parameters can be compared with the frequency parameter $V = kR_0(n_1^2 - n_2^2)^{1/2}$ and eigenvalue parameter $W = R_0(\beta^2 - k^2 n_2^2)^{1/2}$ of conventional step-index fibres [26, 28]. The differences are that, while the characteristic transverse length-scale of the latter is the core radius R_0, in a PCF the length-scale is defined by the cladding pitch; and that w^2 is negative for core modes in a bandgap-guiding fibre.

These equations describe how the frequency and propagation constant of a photonic state will scale when the materials that make up the PCF change. Even though they are strictly valid only for very small index contrasts, they can still give qualitative results for larger contrasts [41]. This is because the vector nature of the electromagnetic field becomes most apparent at the interfaces, where the the last term of the LHS of Equation 3.1 (the vector term) cannot be neglected. However, in PCFs the photonic states result from interference effects away from

the interfaces, where the scalar description is approximately valid and where the vector term is zero.

Using the first of Equations 3.4 for the situation in which the low index material n_2 of the fibre is varied while the high index material n_1 is unchanged, the following simple and useful index-scaling law is obtained: when the index contrast of the PCF changes from $N_0 = n_1/n_2$ to N, any photonic states occurring at a wavelength λ_0 will shift to a new wavelength λ given by:

$$\lambda = \lambda_0 \left(\frac{1 - N^{-2}}{1 - N_0^{-2}} \right)^{1/2} . \tag{3.5}$$

This equation can potentially be a very useful tool for the study of bandgap structures of varying low index materials because it avoids the complexities of numerically solving the vector wave equation. Such an index scaling law is also extremely relevant to any application that requires filling a HC-PCF with gases or liquids.

In order to check to validity of this law, the experiments described in the following sections were carried out [39], where all the air in the HC-PCFs was replaced with heavy water in order to reduce the index contrasts of the fibres. This was the first experimental demonstration of the validity of the index scaling laws found in [41].

3.2 Experimental procedure and results

3.2.1 Experimental set-up and procedure for white light transmission spectra

White light transmission spectra were taken using the experimental set-up shown in Figure 3.3. The two HC-PCF ends were mounted into specially designed cells and the core and cladding holes were filled along the whole length of the fibre with liquid deuterium dioxide (D_2O). D_2O (also known as heavy water) has a refractive index of about 1.33 in the visible part of the spectrum. By replacing the air in the HC-PCF with heavy water, the index contrast of the fibre structure was reduced

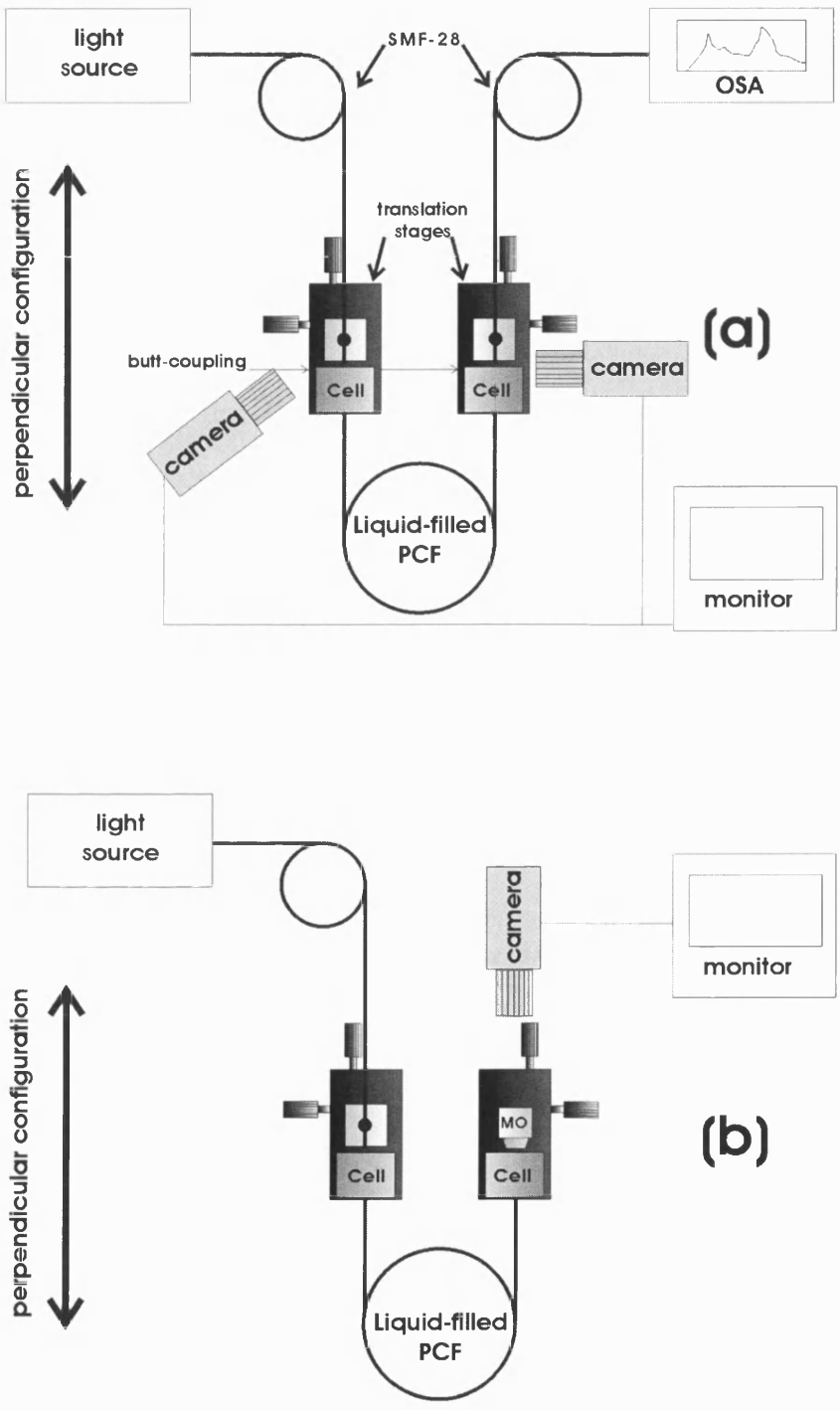

Figure 3.3: Experimental set-up for the acquisition of (a) white light transmission spectra and (b) near-field images of the transmitted light

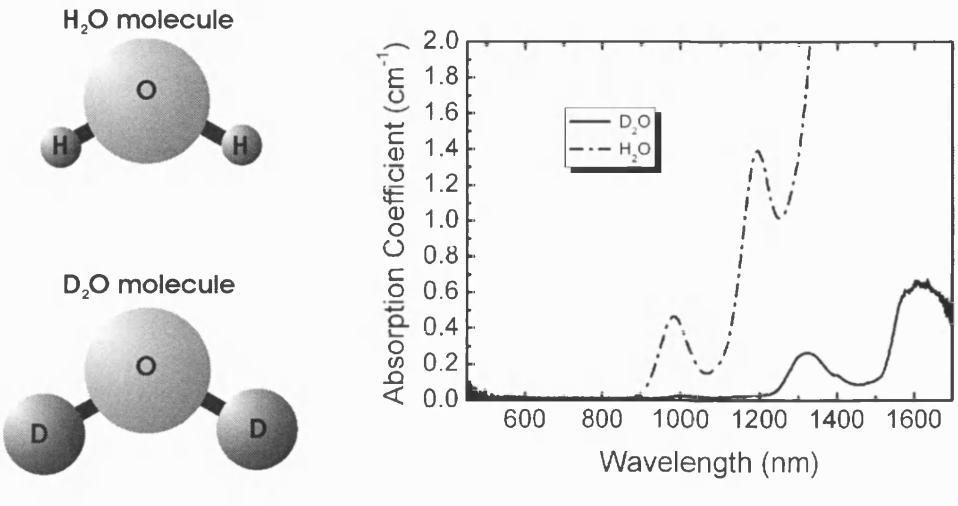

Figure 3.4: A schematic representation of the H_2O and D_2O molecules (right) and the absorption spectrum of D_2O (left). The absorption peaks of water at 980 nm and 1190 nm have moved to about 1320 nm and 1620 nm respectively in the case of heavy water. The absorption data in the figure were provided by Dr William Wadsworth

from about 1.46 to 1.10. D_2O was preferred to ordinary water because it is much less lossy in the near infrared. The reason for this is here briefly explained: the deuterium nucleus consists of a proton and a neutron and so it has double the mass of the hydrogen nucleus. This causes the absorption peaks of ordinary water associated with the hydroxyl ion (OH^-) to be shifted further into the infrared in the case of D_2O (by a factor of $\sqrt{2}$ [45]) as shown in Figure 3.4.

In the experiments described here two hollow-core PCFs were used: one with a bandgap centred at 1060 nm and another with a bandgap centred at 1550 nm. The 1060 nm fibre has a cladding pitch Λ of 3 μm, a core diameter of 8.2 μm, while the length of the sample was 40 cm. The respective figures for the 1550 nm fibre are 3.75 μm, 10 μm and 70 cm.

The design of the cells is shown in Figure 3.5. They were made of aluminium blocks that could be directly mounted onto XYZ translation stages. At one end of the cell there is a bore with a diameter of 0.5 mm. The fibre was initially passed through and glued onto a glass capillary in order to match the fibre diameter (125 μm) with that of the bore of the cell. This was done to prevent any bending of the fibre during the experiments. Then the capillary bearing the HC-PCF was passed through and glued onto the bore of the cell. Suitable water-resistant epoxy was used to seal any gaps between the capillary, the fibre and the bore so

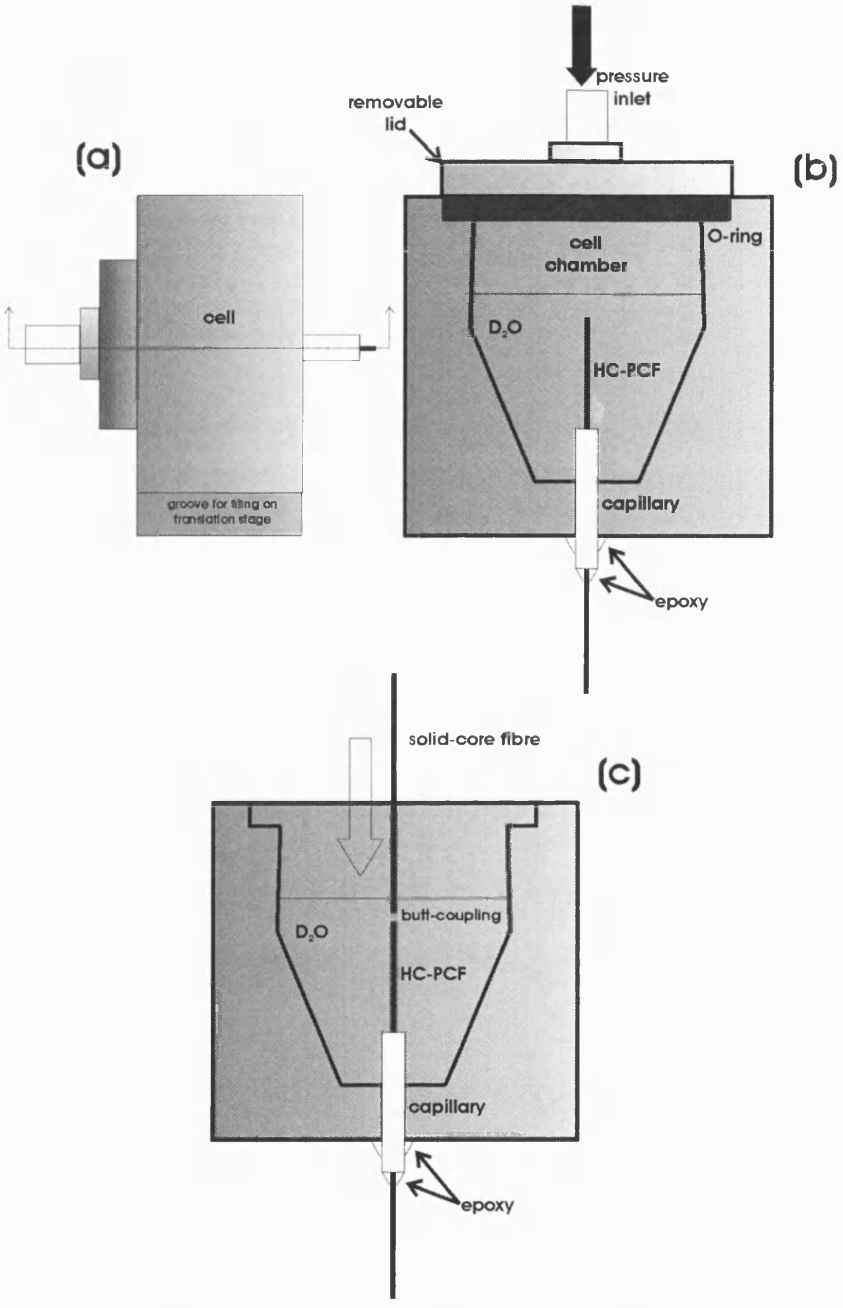

Figure 3.5: Design of the cells used in the index-scaling experiments. Figure (b) shows a cross-sectional view from the top of the cell as indicated by the arrows in (a). Figure (c) schematically shows the set-up for launching white light in the liquid-filled PCF, with the cell lid removed to allow optical access to the input end of the fibre

as to prevent any leakage of air or liquid. At the face of the cell opposite the fibre bore there is a larger opening which is used for optically accessing the fibre. This larger opening can be air-sealed (see Figure 3.5) using a removable lid that bears a pipe through which pressure can be applied inside the cell chamber.

Once both ends of the fibre were mounted into the cells, the latter were fixed onto translation stages perpendicular to the optical table (for the cells to sustain the liquid D_2O). One of the cells (the input cell) was filled with liquid. The cell was then sealed and a constant pressure was applied inside the cell chamber. The pressure difference between the two ends of the HC-PCF caused the liquid to flow through the air channels – the core and cladding holes – of the fibre. The filling process was observed by using CCD cameras connected to CRT monitors. The output fibre end was imaged in order to check for the completion of the flow of D_2O through the fibre, since the flow of liquid through the fibre was clearly visible on the monitor screen. Due to the applied pressure at the input end of the fibre, any air bubbles trapped in the HC-PCF were pushed out of the output end of the fibre. A pressure of just a few bars was sufficient for the filling of the holes to be complete within 2-3 hours. Once D_2O had filled all the fibre channels, the output cell was filled with D_2O and, finally, the lid of the input cell was taken off. This final step prevented any suction of air back into the fibre holes, when the pressure in the input cell was removed.

In order to optically access the fibre, white light from a tungsten bulb was coupled into a conventional step-index solid-core telecommunications fibre (SMF-28); the latter was butt-coupled to the input end of the PCF inside the liquid D_2O as in Figure 3.5(c). The tungsten lamp spectrum, recorded as it exits the SMF-28, is shown in Figure 3.8(b). Another piece of SMF-28 was butt-coupled to the output end of the liquid-filled PCF in order to collect the transmitted light and send it into an optical spectrum analyser (OSA). All the butt-coupling was facilitated by using cameras to assist with the alignment of the fibres. This spectrum acquisition procedure was carried out before and after filling the fibres with D_2O. It was, therefore, possible to record the changes in the transmitted spectra due to the change in the index contrast alone, while using the same piece of fibre and keeping, thus, the pitch and symmetry of the lattice unchanged. This eliminated any spectral changes that would be due to structural differences between different fibre samples of varying index contrast.

3.2.2 Results

The transmission spectra taken before and after the filling process are plotted together for each fibre and are shown in Figure 3.6. The spectra – normalised to the input white light spectrum (shown in Figure 3.8) – are plotted both in terms of wavelength and normalised frequency $k\Lambda$. The vertical lines show the edges of the shifted bandgaps as predicted by the index-scaling law. These edges were estimated by applying Equation 3.5 to the experimentally observed edges of the pass band of the original silica/air fibre. For the 1060 nm fibre the original pass band extended over the region 900-1200 nm; using Equation 3.5 this band should shift to about 510-780 nm. Similarly for the other fibre, the original pass band between 1400 nm and 1800 nm shifts to the region 790-1020 nm. Finally, the arrow marks the peak of the initial pass band and the wavelength to which this peak is predicted to shift.

In Figure 3.6, there is good agreement between the experimental spectra and the predictions of the index scaling law. The shifted spectra for both fibres peak within the bandgap edges given by Equation 3.5. Light recorded outside these edges is believed to come from the cladding; this light survives at the output due to the relatively short lengths of fibre used in these experiments. The fact that light outside the predicted bandgap comes from the cladding becomes more apparent when a much brighter supercontinuum source is used (Figure 3.8), as described in the next section.

In order to reduce the cladding contribution the fibre was wound a few times around a 1 cm rod in order to increase the loss rate of light propagating in the silica regions by means of total internal reflection. A typical spectrum of the wound liquid-filled fibre is shown in Figure 3.7. The spectra are again normalised to the input white light spectrum. In the shifted spectrum of the liquid-filled fibre there is now a reduction in the amount of light that falls outside the predicted bandgap at the long-wavelength end of the spectrum.

By comparing the magnitude of the transmitted signal of the D_2O-filled fibres with that of the unfilled ones, it is observed that the former is weaker than the original. Due to the short lengths of fibre used, the HC-PCF loss figure of about 70-75 dB/km is practically negligible. The decrease in intensity may be due both to the higher absorption coefficient of D_2O compared to that of air

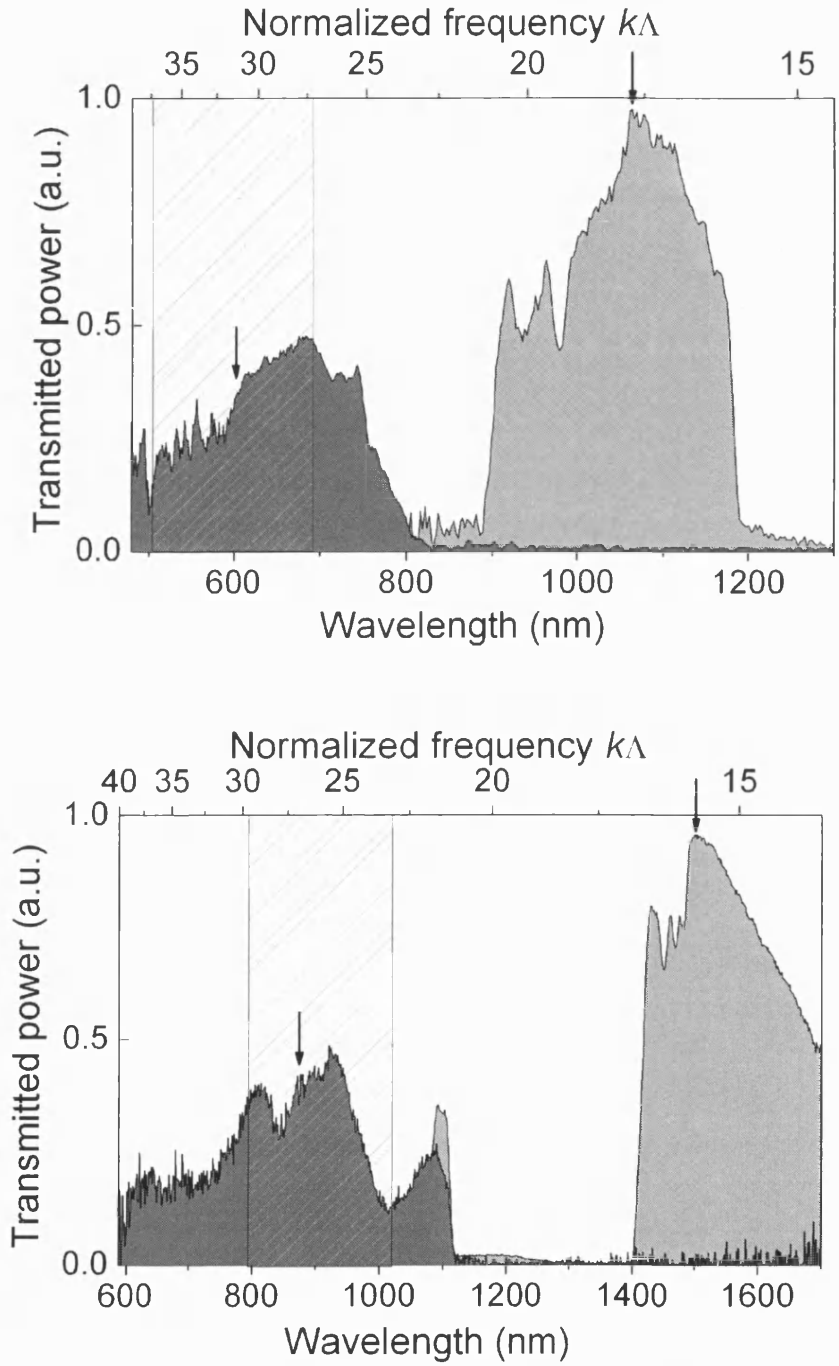

Figure 3.6: White light transmission spectra of the 1060 nm fibre (top) and the 1550 nm fibre (bottom). The spectra were taken before and after filling the holes of the HC-PCF with liquid D_2O (light and dark grey areas respectively). The vertical lines define the location of the new shifted bandgaps as predicted by the index scaling law. The arrows mark the position of the respective transmission peaks

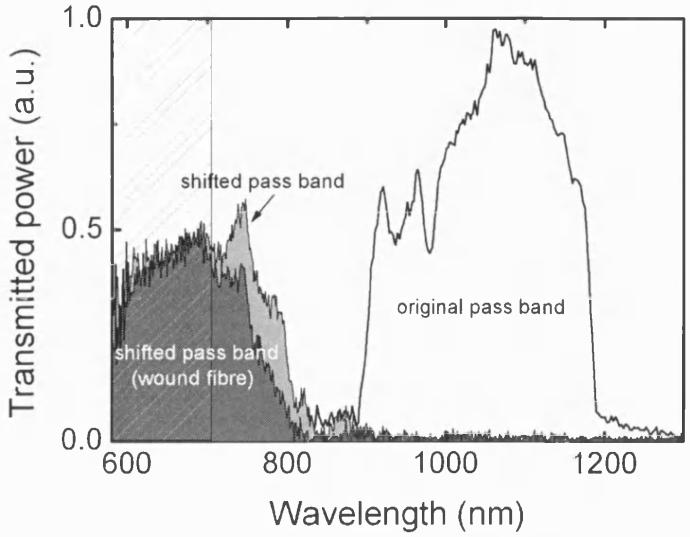

Figure 3.7: White light transmission spectra of the 1060 nm HC-PCF before and after filling it with D_2O and after winding the liquid-filled fibre 5 times round a 1 cm rod. The spectra are normalised to the input white light spectrum. The shaded rectangle defines the predicted location of the shifted bandgap

and to scattering impurities in the liquid that fills the entire length of the fibre (for example, suspended dust particles from the inner walls of the cells or any remaining air bubbles inside the fibre holes). Some of these bright scattering points were occasionally seen on the monitor screen during these experiments. Some coupling losses also occur and these were measured to be in the range 3-5 dB before the fibre was filled with D_2O. When the fibres are immersed in the liquid, the coupling losses could increase due to scattering impurities between the fibre end-faces. However, since the waveguide loss rate of the liquid-filled fibre is not known, these coupling losses cannot be directly estimated.

The same experiments were repeated with the 1060 nm fibre, but this time, instead of a tungsten white light source, a bright supercontinuum source was used (Figure 3.8). This source spectrum spans several hundred nanometres of wavelength and is much brighter than the white light source used in the previous experiments, as shown in Figure 3.8(b). It consists of a solid-core PCF with a core diameter of about 5 μm and $d/\Lambda = 0.5$. The fibre length was about 20 m. The PCF is pumped by a passively Q-switched Nd:YAG microchip laser (JDS Uniphase model number NP-10620-100) operating at 1064 nm with pulse duration 0.6 ns and repetition frequency 7.2 kHz. The average laser power is 30 mW, which

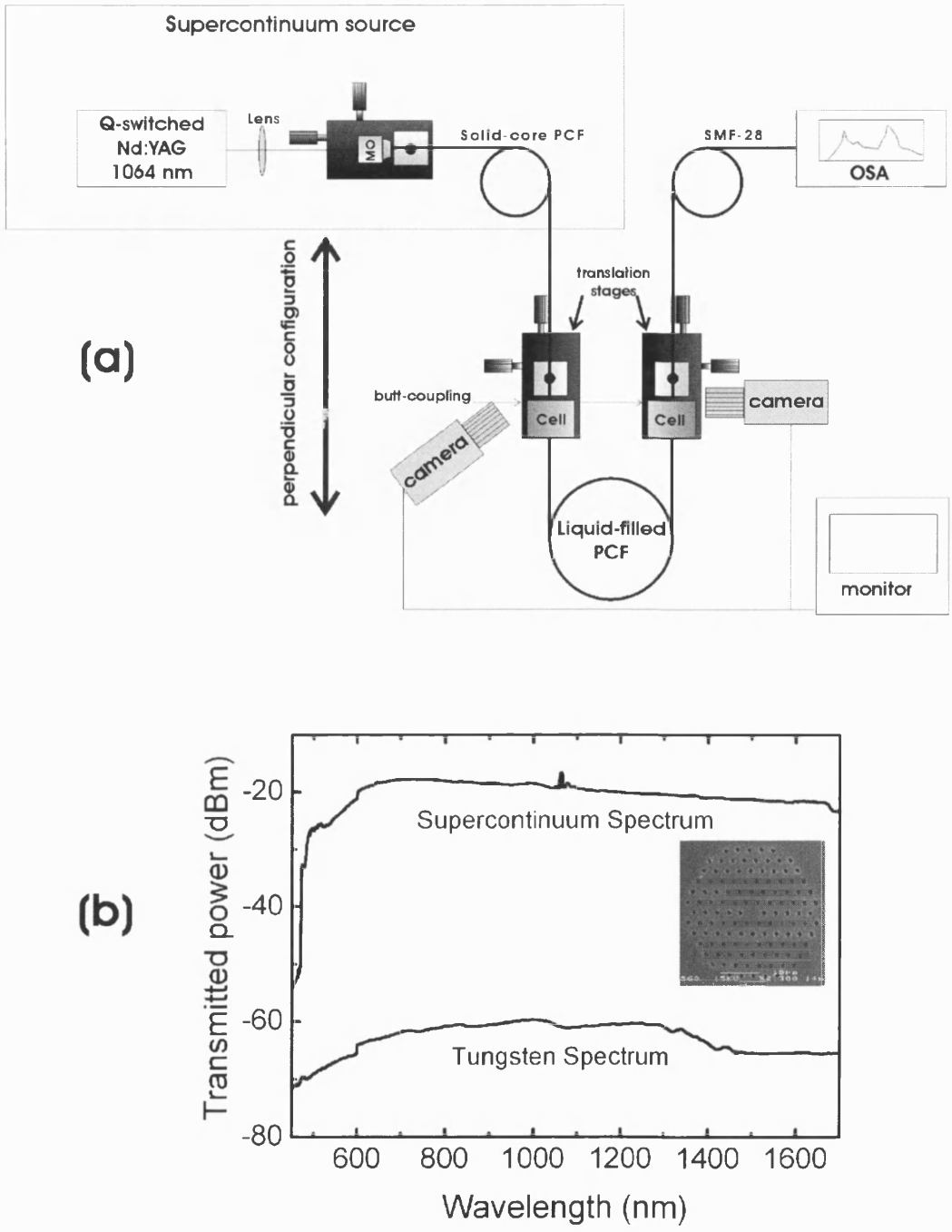

Figure 3.8: (a) Set-up for the acquisition of transmission spectra using a supercontinuum source. (b) Spectra of the supercontinuum source and the tungsten source used in the experiments. The inset shows an electron micrograph of the PCF used for supercontinuum generation. The relatively flat supercontinuum spectrum exiting the solid-core PCF extends from about 450 nm to well beyond the detection limit of the OSA used

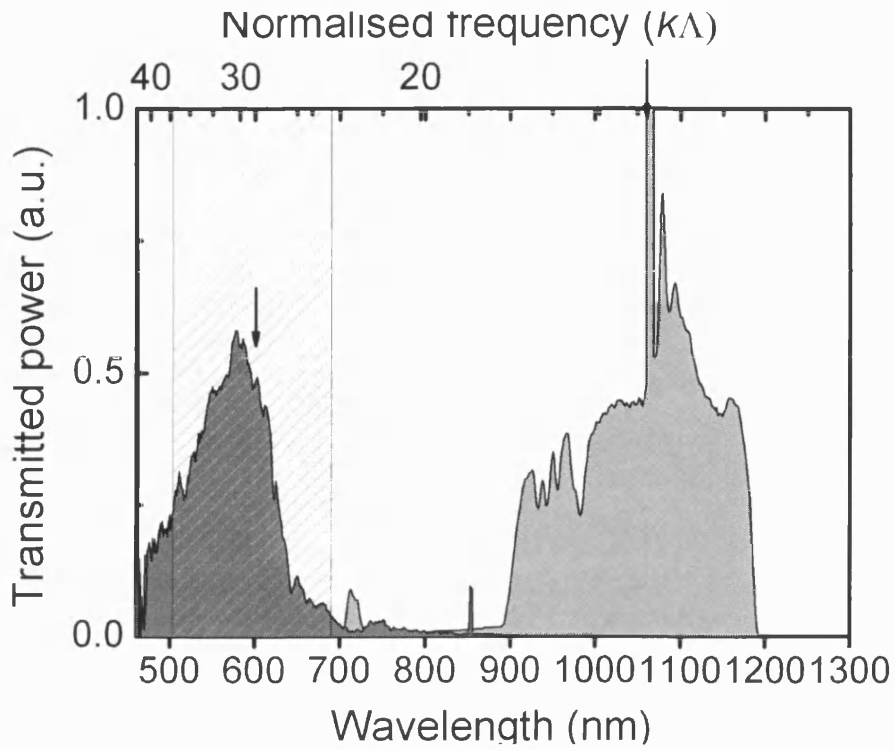

Figure 3.9: Transmission spectra of the 1060 nm fibre taken with a supercontinuum source before (light grey) and after (dark grey) filling the fibre with liquid

gives a pulse energy of 4.1 μJ and 6.9 kW peak power. The fibre was made at the University of Bath and has been reported to produce a broad supercontinuum spectrum via parametric four-wave mixing [46]. The supercontinuum spectrum was recorded before the experiments and is shown in Figure 3.8(b). The use of such a bright broadband source makes the output signal acquisition much easier and practically free of noise.

Exactly the same procedure as described previously was employed for the acquisition of the transmitted spectra , but this time the solid core PCF was directly butt-coupled to the input end of the D_2O-filled PCF. These spectra – normalised to the supercontinuum spectrum – are shown in Figure 3.9. The spike of the initial spectrum around 1060 nm is due to the laser source that pumps the solid-core PCF. The agreement between the predictions of the scaling law and the experimental observations is now excellent. If this figure is compared with the top plot of Figure 3.6, it is made obvious that any discrepancies in the latter from the index scaling law are largely due to cladding contributions, which are harder to eliminate with weaker source signals: any loss mechanisms inside the water (for example, bubbles and suspended particles) will be more pronounced

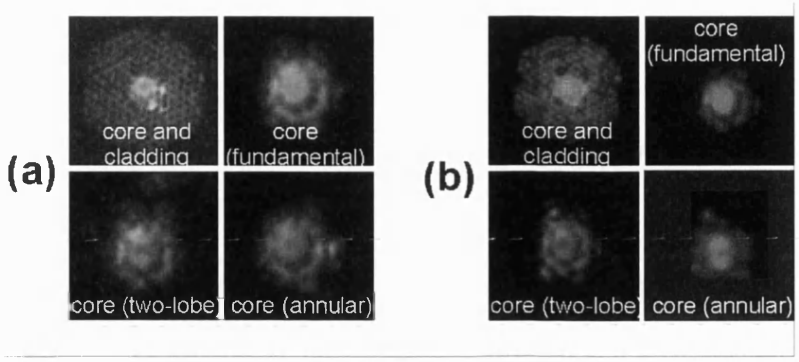

Figure 3.10: CCD camera images of the near-field intensity distribution at the output end of the D_2O-filled PCF. The set-up is shown in Figure 3.3(b). In (a) the input light is the supercontinuum light of Figure 3.8, while in (b) the input light is that of a laser diode at 633 nm

for light in the core rather than in the cladding and so, for weaker input signals, this will decrease the signal-to-noise ratio.

Near-field imaging

Images of the near-field intensity distribution at the output fibre end were taken for the 1060 nm D_2O-filled PCF. The experimental set-up is that shown in Figure 3.3(b). A long working distance $\times 20$ microscope objective collected the light at the fibre output and imaged it onto a colour CCD camera. Initially, the supercontinuum light was used as a source. The near-field images thus acquired are shown in Figures 3.10(a). Three core modes were excited: a mode with an intensity peak in the middle of the core (the fundamental mode), an annular mode and a two-lobe mode. The orange/red colour of the transmitted core modes matches very well with the location of the shifted bandgap of the liquid-filled fibre as can be seen in Figure 3.9 and provides a visual demonstration of refractive index scaling.

The same procedure was repeated using a laser diode operating at 633 nm as a source. This wavelength lies well within the shifted bandgap of the liquid-filled fibre. Indeed the same core modes as the ones observed with the white light source were excited at the output of the fibre; they are shown in Figures 3.10(b).

In the above patterns, surface modes were observed around the central core area.

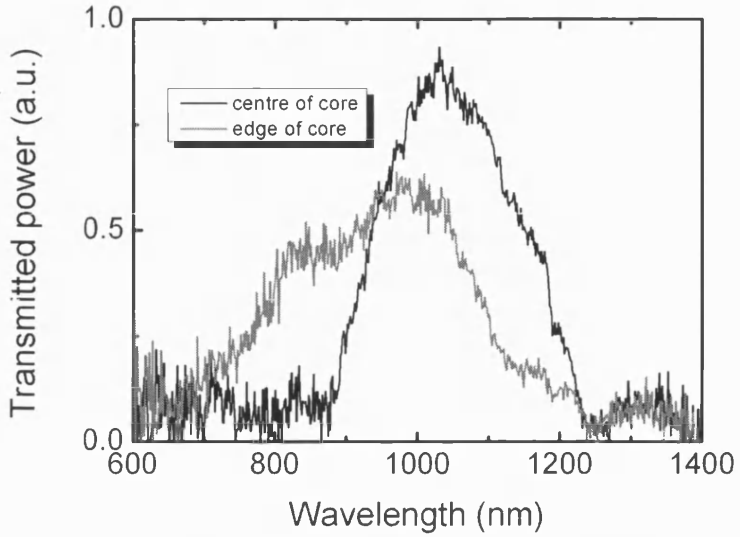

Figure 3.11: Transmission spectra of the (unfilled) HC-PCF taken by collecting light from the centre and the edge of the core from the near-field intensity distribution

Since the scaling laws apply to all photonic states, surface modes of the silica/air fibre should also scale with refractive index. Surface modes are also visible in the near-field patterns of the original silica/air fibre, as can be seen in Figure 2.6 on page 12. They also appear in the original transmission spectrum of the 1060 nm HC-PCF (Figures 3.6(a), 3.7 and 3.9) as high-loss regions at the lower wavelength side of the transmission band. That these high-loss regions are due to surface modes was further indicated by an experiment done using the unfilled HC-PCF: the near-field intensity pattern at the output end of the HC-PCF was collected and magnified using a microscope objective lens. By means of a collecting fibre, spectra from the centre and the edge of the fibre core were recorded. These are shown in Figure 3.11. The light coming from the edge of the core is mostly located in the low wavelength region of the transmission band, while light coming from the fundamental mode is more sharply confined within the bandgap.

3.3 Modelling results

Full-vector calculations were also performed for the fibre structure used in the experiments. Since the index-scaling law is based on the scalar wave approximation,

it should always be checked against the predictions of full-vector calculations. The modelled photonic crystal is shown in Figure 3.12. Density of states (DOS) maps were produced for the structure with a background index of 1.45 (silica), while for the index of the holes both the values of 1.00 (air) and 1.33 (D_2O) were taken. The model used for the DOS calculations and the dielectric function representation was the same as in [20, 21] and has already been mentioned in Section 2.1.1. The DOS maps for the two cases of air and D_2O are also shown in Figure 3.12. The initial (silica/air) bandgap in the DOS map lies between 13.8 and 16.9 units of normalised frequency. When air is replaced by D_2O, the bandgap shifts to higher frequencies, between 23.1 and 28.9 units of normalised frequency. This seems to agree quite well with what was experimentally observed with the 1550 nm fibre in Figure 3.6(b). There is however discrepancy with the results from the 1060 nm fibre (Figure 3.6(a)). This must be due to differences between the real fibre structure and the one used in the vector calculations.

Both in the experiments and the full-vector calculations, the shifted bandgaps occurring for smaller index contrasts appear to be wider in frequency than the bandgaps of structures with higher index contrasts. This has been observed before [47] and it can easily be explained [41]; the overall bandgap is the overlap of the bandgaps of each of the two states of polarisation. For small index contrasts (scalar regime) the two polarisation states are degenerate and their bandgaps completely overlap. As the index contrast increases (vector regime), there is splitting of the two polarisation states, the bandgap overlap is smaller and a narrower overall bandgap is generated.

3.4 Summary and conclusions

White light and supercontinuum spectra of HC-PCFs were taken before and after filling the fibres with heavy water and lowering thus their refractive index contrast. In these experiments the usefulness of the index-scaling laws (Equation 3.5, derived using the scalar-wave approximation) as a preliminary tool for the study of photonic bandgap fibres was demonstrated for the first time. There was good qualitative agreement between the observed transmission bands of the liquid-filled PCF's and the predictions of both a full-vector model and the scaling law. Discrepancies between experiment and the index scaling laws are mostly due to the

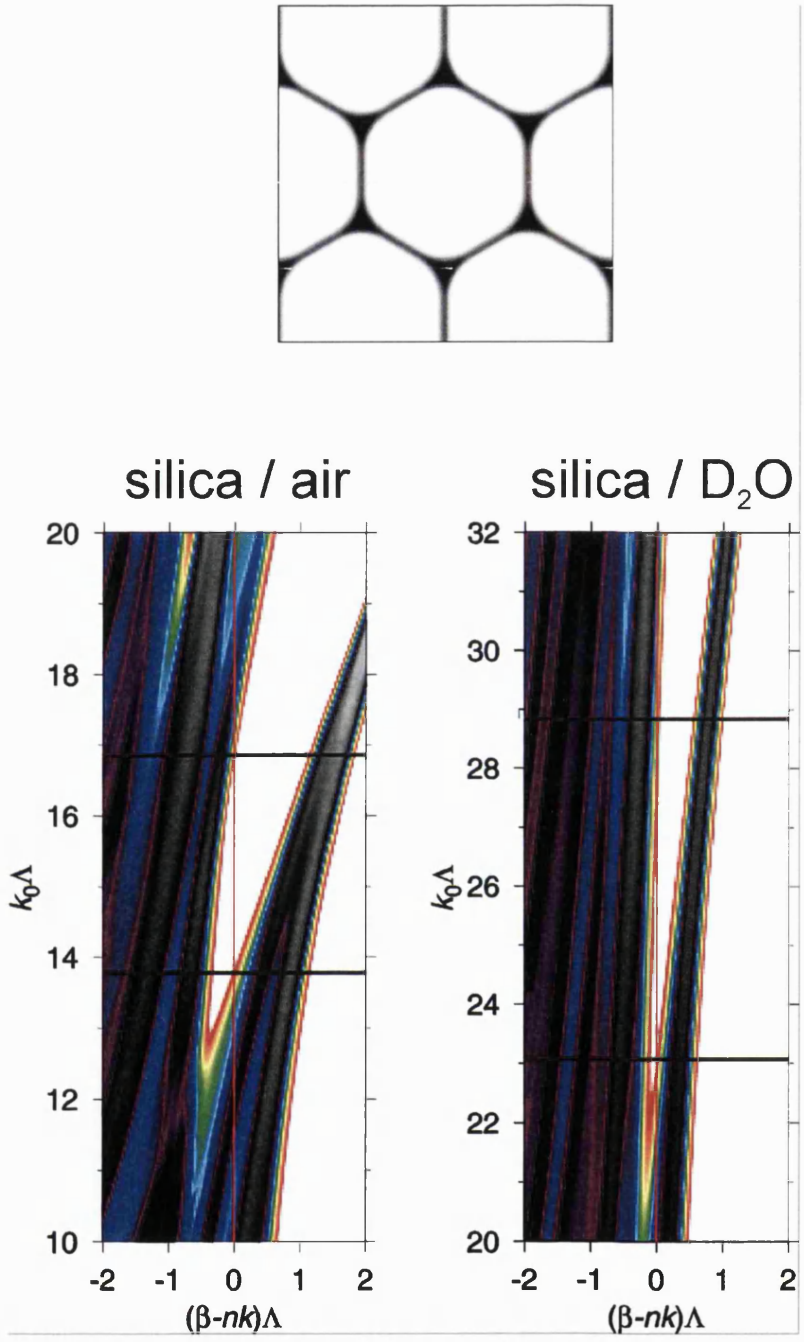

Figure 3.12: Full-vector calculations for the density of states for the photonic crystal shown at the top. The background index of the crystal was taken to be that of silica (1.46), while the index in the holes was equal to that of air (bottom left plot) and that of heavy water (bottom right)

fact the latter are strictly valid for the smallest index contrasts and also due to experimental factors, such as contribution from light in the fibre cladding. Some widening of the shifted bandgaps in the low-index-contrast fibres was observed in accordance with theory. Moreover, the experiments demonstrated bandgap guidance of light in liquid.

Refractive index scaling is something that should always be taken into account when filling a HC-PCF with materials other than air. However, very small differences in refractive indices have a negligible effect on the transmission spectrum of the fibre. This is the case with the work described in the two following chapters, where HC-PCFs were filled with hydrogen gas: the index of the latter differs from air by only about 10^{-3} and so any shifts in the fibre bandgap are too small to be taken into account.

Chapter 4

Vibrational stimulated Raman scattering in hydrogen-filled hollow-core photonic crystal fibre

In the work presented in this and the next chapter, HC-PCF is used as the host of hydrogen gas for efficient stimulated Raman scattering (SRS).[1] This chapter presents extremely low-threshold generation of vibrational Stokes radiation, 100 times lower than ever before reported; this low-threshold regime is attributed to the very high FOM of the HC-PCF as a Raman gas host. The evolution of the different SRS bands with input pump power and interaction length is also investigated.

4.1 Introduction

This section provides a brief introduction to SRS in hydrogen gas. It introduces some basic concepts and notations that will be used throughout this and the following chapters.

[1]The work presented in this chapter was carried out jointly by the author and Dr F. Benabid. It has been published in [11, 48]

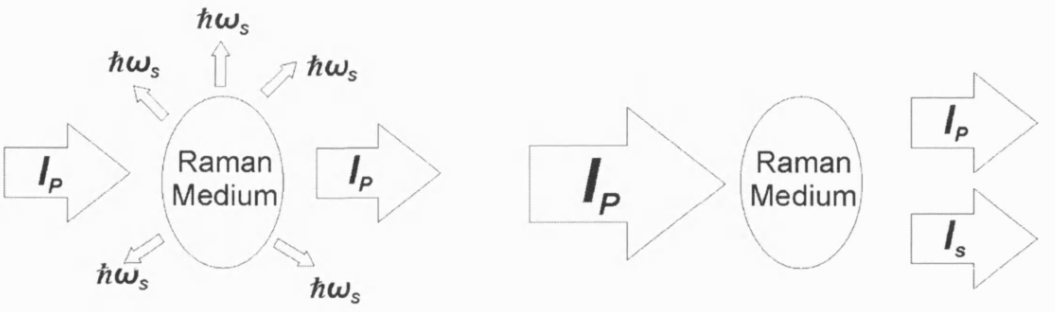

(a) Spontaneous Raman scattering (b) Stimulated Raman scattering

Figure 4.1: Schematic comparison between spontaneous and stimulated Raman scattering (SRS)

4.1.1 Spontaneous and stimulated Raman scattering

Apart from the scattering of light by electrons in a medium, the nuclear motion can also modify the scattering process. The scattered light can thus be shifted in frequency by the characteristic frequencies of optical or acoustic phonons. The former is called Raman scattering (inelastic scattering of light by optical phonons) and the latter Brillouin scattering (inelastic scattering of light by acoustic phonons). In spontaneous Raman or Brillouin scattering the scattered waves do not affect the scattering process: when a Raman-active medium is illuminated by a laser beam (called the "pump" beam) of relatively low intensity, the molecules may scatter light inelastically, emitting photons at new Raman-shifted frequencies. As the input pump beam intensity is kept low, different molecules will scatter light independently and incoherently with one another (Figure 4.1(a)). This is the case of sponatenous Raman scattering.

On the other hand, when the incident pump intensity is high enough, there will be strong enough scattered waves that have the right phase to produce interference with the incident wave and with the wave of the excited molecular motion in the medium. This is the case of stimulated Raman scattering (SRS) [49]. The nonlinearity of the medium offers the necessary coupling between the waves. Due to this interference, there can be a rapid build-up of the radiation at the newly generated Raman-shifted frequencies at the expense of the incident beam power (Figure 4.1(b)). The coupled wave equations for the fields are briefly derived in Appendix A; also in that appendix, the equations describing the growth of the Stokes and Anti-Stokes waves are given.

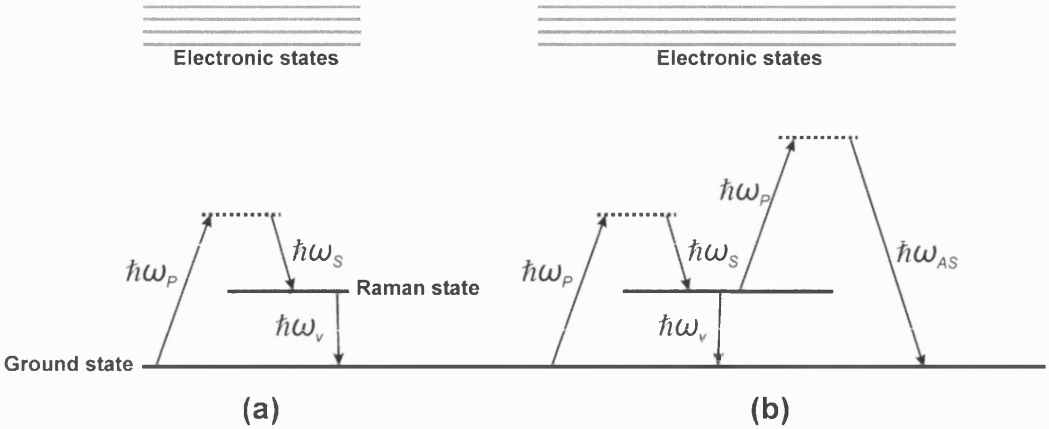

Figure 4.2: Energy levels showing the generation of a Stokes photon (a) and a Stokes and Anti-Stokes photon (b) during Raman scattering

Raman transitions of the hydrogen molecule

The inelastic scattering of the pump photons with frequency ω_P by a Raman-active medium can produce photons at new frequencies shifted by an amount equal to the frequency ω_v of the excited Raman transition, as shown in Figure 4.2. These new frequencies are called Stokes ($\omega_S = \omega_P - \omega_v$) and Anti-Stokes frequencies ($\omega_{AS} = \omega_P + \omega_v$). The Anti-Stokes wave is generated via a parametric wave-mixing process between the pump and Stokes wave (see Section A.3 on page 118 of the Appendix).

As the power of Stokes and Anti-Stokes fields increases, they can, in turn, act as pump fields for Raman scattering generating higher-order Stokes and Anti-Stokes bands. The nth order Stokes and Anti-Stokes frequencies will respectively be $\omega_{Sn} = \omega_P - n\omega_v$ and $\omega_{ASn} = \omega_P + n\omega_v$.

In general, there can be three types of Raman transitions: vibrational, rotational or a combination of rotation and vibration (ro-vibrational states), as shown schematically in Figure 4.3 for a diatomic molecule, such as H_2. Each vibrational Raman state of the molecule is denoted by the quantum number $v = 0, 1, 2, 3, \ldots$, with $v = 0$ the ground state. In Raman scattering the selection rule for transitions between vibrational states is [50]:

$$\Delta v = 0, \pm 1, \pm 2 \; . \tag{4.1}$$

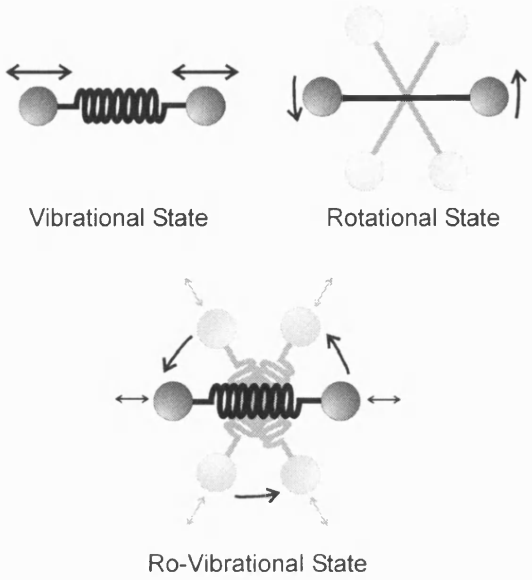

Figure 4.3: Schematic examples of different excited Raman states of a diatomic molecule, such as H_2

Furthermore, the vibrational states have a fine structure of rotational states, each denoted by the quantum number $J = 0, 1, 2, \ldots$ (for diatomic molecules). For the hydrogen molecule in particular, the ground rotational state can be either $J = 0$ (when the nuclear spins of the two hydrogen atoms are anti-parallel) or $J = 1$ (when the nuclear spins of the two hydrogen atoms are parallel). The latter is called ortho-hydrogen and the former para-hydrogen. In a normal (unprepared) hydrogen gas at room temperature they occur at a ratio of 3:1.

The selection rule for rotational Raman transitions is [50]:

$$\Delta J = 0, \pm 2 \ . \tag{4.2}$$

According to the molecular states involved, Raman transitions are divided into branches. The Raman transition branches are written in the form:

$$X_{vv'}(J) \ , \tag{4.3}$$

with v and v' the initial and final vibrational states respectively and J the quantum number of the initial rotational state. The Q branch involves purely vibrational transitions with $\Delta v = 1$ and $\Delta J = 0$. For hydrogen molecules, $Q_{01}(1)$ is the vibrational transition $v = 0 \rightarrow v' = 1$ and $\Delta J = 0$ of ortho-hydrogen. The Raman frequency of this transition is 4155 cm^{-1} (198.4 THz). The S branch

describes rotational or ro-vibrational transitions where $\Delta v = 0$ or $v = 0 \rightarrow v' = 1$ and $\Delta J = \pm 2$. For hydrogen molecules, $S_{00}(1)$ describes the purely rotational transition $\Delta v = 0$ and $J = 1 \rightarrow J' = 3$ of ortho-hydrogen, while $S_{00}(0)$ the rotational transition $\Delta v = 0$ and $J = 0 \rightarrow J' = 2$ of para-hydrogen. The respective Raman frequencies are 587 cm^{-1} (28.2 THz) and 354 cm^{-1} (16.9 THz).

Applications of gas-based SRS

Gas-based SRS is a useful nonlinear phenomenon with many diverse applications: it has been used for broadband generation [51], Raman gas lasers [32], high-resolution spectroscopy and even pulse compression [52, 53] and phase conjugation [54]. Hydrogen gas in particular has been extensively studied and used in SRS due to its high Raman gain, and so there is a variety of work on gas-based SRS using different experimental schemes for efficient SRS generation.

Previous work on vibrational SRS in hydrogen gas

As outlined in the previous chapter, mainly two experimental configurations for single-pass SRS generation have been used so far: a free-space laser beam tightly focused onto a volume of a Raman-active medium (as in [55]), where SRS is observed due to the high intensity of the light field at the beam focus; and the use of a dielectric capillary as a host for the Raman-active medium, where the laser beam is coupled into the lowest-loss mode of the capillary. This technique increases the interaction length and improves the FOM of the nonlinear process (as in [56, 31], for example). Relatively low threshold energies of the input pump pulses were achieved (in the order of 10 μJ with $\sim$ 0.1 ps pulses) [55, 56], even though the power requirements remained very high ($\geq$ 1 MW).

Multiple-pass configurations have also been used in SRS, where the nonlinear medium is confined in an optical cavity. This has been most successfully implemented using a high-finesse Fabry-Pérot cavity (FPC), with a resonant frequency tightly locked to the pump laser frequency [32]. Continuous-wave SRS generation has been thus observed at input pump powers as low as 400 μW, using a doubly-resonant cavity filled with hydrogen with an intensity enhancement factor of 25×10^3. However, in these experiments the conversion efficiency is small and

the laser frequency needs to be tightly locked to the resonant design of the FPC.

4.2 Experimental results and discussion

4.2.1 Choice of fibre for vibrational SRS in hydrogen gas

When using a HC-PCF as a Raman gas host, it is necessary to consider the transmission spectrum of the fibre with respect to the generated SRS spectrum. For the first-order SRS bands of the $Q_{01}(1)$ vibrational transition of hydrogen to be transmitted by the fibre, a bandwidth of at least 200 THz around the pump frequency is required. Such a wide transmission spectrum is unattainable by most bandgap-guiding fibres (look, for example, at the transmission spectrum of the photonic bandgap fibre such of Figure 2.6 on page 12).

In order to overcome this limitation, the HC-PCF used in the experiments described in this chapter is the Kagomé fibre (described in Chapter 2), which guides light by means of low-density-of-states (LDOS) guidance over a broad frequency range (see Section 2.1.2). The transmission spectrum of the fibre (which covers almost the entire visible and near-IR range) is presented here again in Figure 4.4 together with the positions of the pump, Stokes and Anti-Stokes wavelengths for the present experimental conditions. The minimum loss rate is in the range 1-3 dB/m. Recalling Figure 2.13(b) on page 22, this fibre offers a FOM enhancement of about 10^2 compared to other SRS techniques, to which the very low threshold SRS achieved is attributed.

4.2.2 Experimental set-up

The experimental set-up is shown in Figure 4.5(a). The two ends of the HC-PCF were mounted onto specially designed cells (Figure 4.5(b)). This was done by inserting the fibre into a fibre holder equipped with O-ring seals. Then the holder was screwed into the gas cell. Both ends of the fibre were optically accessed through anti-reflection coated windows to avoid back-reflections. The fibre was mounted in such a way as to have its end-face close to the cell windows, while

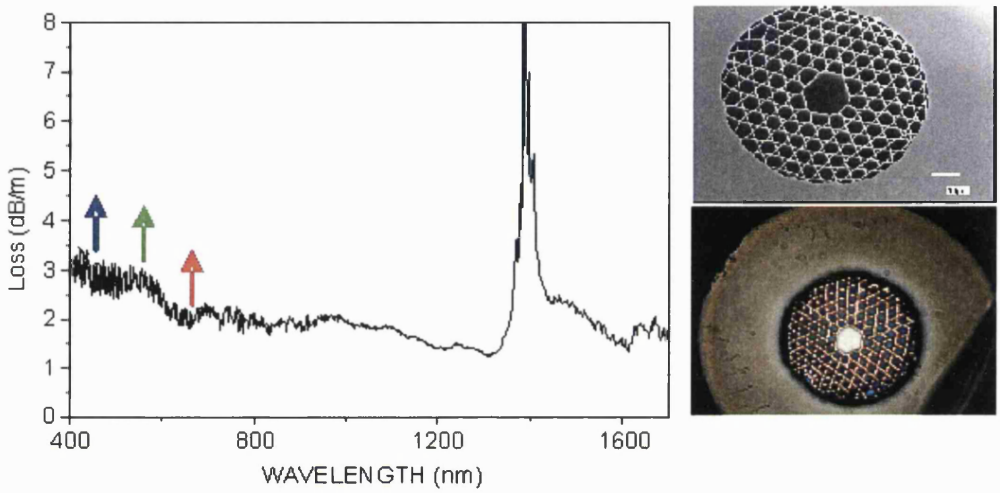

Figure 4.4: The loss spectrum of the Kagomé fibre used for vibrational SRS in hydrogen. The transmission range of the fibre covers the entire 400-1300 nm region. The arrows show the wavelengths of the pump laser (green), Stokes (red) and Anti-Stokes (blue) radiation. The top right image is an electron micrograph of a cross-section of the fibre showing the Kagomé lattice of the cladding. The bottom right picture shows an optical micrograph of a cross-section of the fibre when the latter is illuminated from below with white light. The very broad transmission spectrum of the fibre accounts for the white colour of the light transmitted in the fibre core

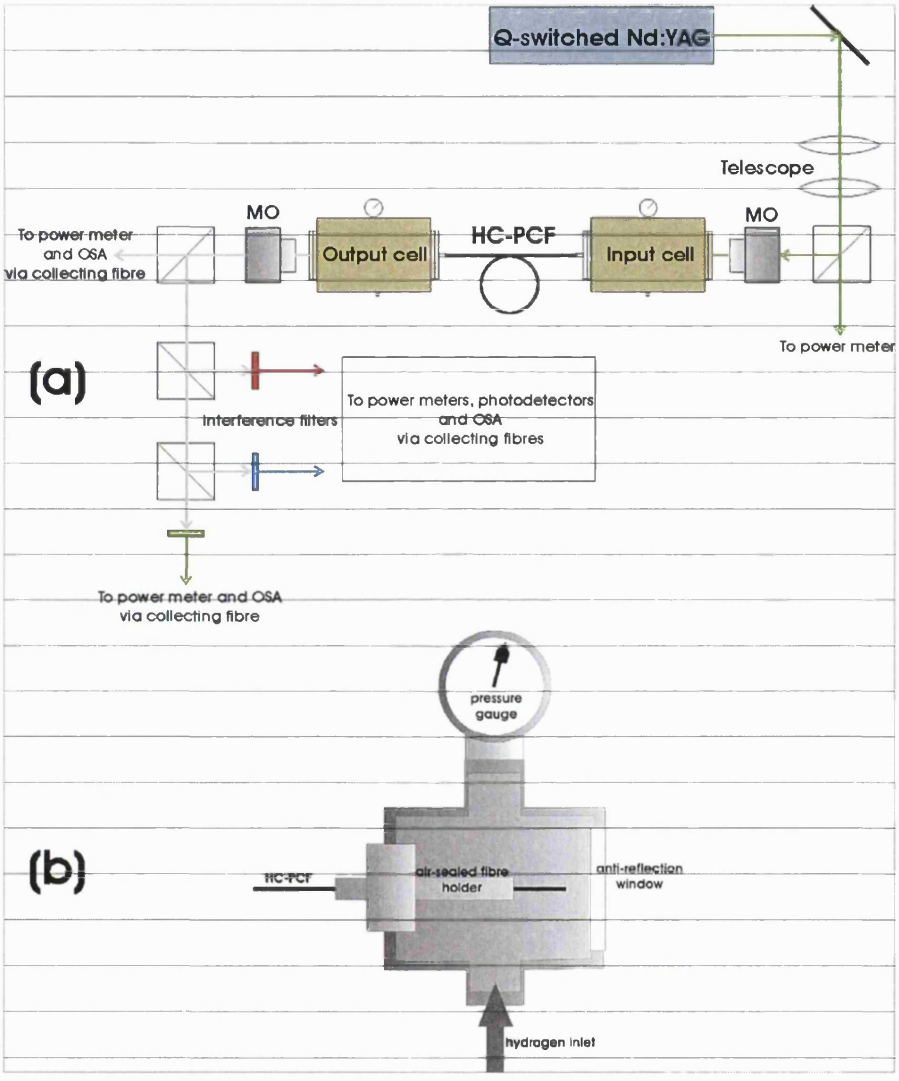

Figure 4.5: (a) Experimental set-up for vibrational SRS in hydrogen-filled HC-PCF. (b) Schematic cross-section of the gas cells used in the experiments for filling the HC-PCF with hydrogen gas

still being held firmly in place by the fibre holder. Once the fibre was mounted, one of the cells was filled with H_2 gas. Both cells were equipped with gauges to monitor the pressure in the interior of the cells. The hollow core and the holes in the cladding of the HC-PCF acted then as gas pipes that linked the two cells and, after sufficient time had elapsed, the pressure in the two cells was equalised. The highest pressure achieved was 50 bar, which was the actual recording limit of the pressure gauges. The results presented here were acquired at an equilibrium hydrogen pressure of 17 bar and for a maximum fibre length of 92 cm.

The pump source used was a Q-switched single-mode frequency-doubled Nd:YAG operating at 532 nm with a repetition frequency of 20 Hz and pulse duration 6 ns. The laser beam passed through a neutral density filter and then through a pair of lenses acting as a telescope to enhance the coupling efficiency into the fibre. Afterwards the beam was split into two beams in a 50:50 beam-splitter; one of the beams was sent to a power meter while the other was passed through a $\times 4$ microscope objective placed before the input cell window and coupled into the lowest-loss mode of the Kagomé HC-PCF. The light coming out of the HC-PCF was collected by another microscope objective after the output cell window and sent to a beam-splitter where it was split into two beams; one beam was directed either to an optical spectrum analyser (OSA) or to a fast photodetector to monitor the total output spectrum or power. The other beam was further split and sent to fast photodetectors in front of which narrow-band (10 nm) interference filters were placed to select the various co-propagating wavelengths. This allowed the recording of the power evolution of the different Raman components with various parameters (fibre length, input power, pressure).

4.2.3 Extremely low-threshold SRS

Using this set-up, extremely low-threshold SRS was observed:[2] the threshold for Stokes generation (Stokes wavelength 683 nm) was 800 ± 200 nJ or 133 W peak power at a fibre length of 17 cm. This threshold value is about 100 times lower than ever before reported [55, 56] and is due to the high FOM of the HC-PCF as a nonlinear gas host. It can be compared with the theoretical threshold energy

[2]The threshold energy will be henceforth defined as the input energy for which the ratio of the transmitted Stokes-to-pump signals becomes 1:100 (20 dB point)

value in the steady-state, where the Stokes intensity grows exponentially:

$$I_S = I_{S0} e^{G_{ss}} \ , \tag{4.4}$$

from the spontaneous Raman noise I_{S0}, with $G_{ss} = g_R I_P L_{eff}$ as shown in Section A.2 on page 116 of the Appendix. From the definition of threshold, one finds that the Stokes gain at threshold is $G_{ss,th} = 20$.

The threshold energy is written as:

$$\begin{aligned} G_{ss,th} &= g_R \frac{P_{P,th}}{A_{eff}} L_{eff} = g_R \frac{\mathcal{E}_{P,th}}{A_{eff}\,\tau} L_{eff} \Longrightarrow \\ \Longrightarrow \mathcal{E}_{P,th} &= \frac{G_{ss,th}\, A_{eff}}{g_R\, L_{eff}} \tau \ . \end{aligned} \tag{4.5}$$

In this derivation, the pulse is treated as a square pulse of width τ. Typical values of the above parameters in this case are $G_{ss,th} = 20$, $A_{eff} = 150\ \mu\text{m}^2$, $\tau = 6$ ns and $g_R = 4.5 \times 10^{-11}$ m W^{-1} [57]. The effective interaction length is defined as [27]:

$$L_{eff} = \frac{1 - \exp(-\alpha L)}{\alpha} \ , \tag{4.6}$$

with α the exponential attenuation coefficient (0.69 m^{-1} for a loss rate of 3 dB/m). This gives $L_{eff} = 0.72$ m. The threshold energy is then found to equal $\mathcal{E}_{P,th} \approx 1\ \mu$J.

The Stokes signal continues to increase beyond the threshold energy and at an input energy $\mathcal{E}_c = 3.4 \pm 0.7\ \mu$J (567 W peak power) and a fibre length of 25 cm a weak Anti-Stokes signal (at 435.2 nm) is observed, which increases rapidly thereafter. The generation of the Anti-Stokes band at such a low power threshold is facilitated by the good phase matching conditions in the fibre core. At the same time, the Stokes signal keeps on increasing but more slowly than before, until it reaches a maximum value and then it starts decreasing slowly. The pump on the other hand, after going through a plateau in the same range of values as the total energy (see below, Section 4.2.3), drops much more rapidly than the Stokes signal. The evolution of the SRS bands is shown in Figure 4.6.

Figure 4.7(a) shows the evolution of the spectrum of light coming out of the fibre with increasing pump power along with the generation of the first Stokes and Anti-Stokes bands, due to SRS and parametric four-wave mixing (FWM) re-

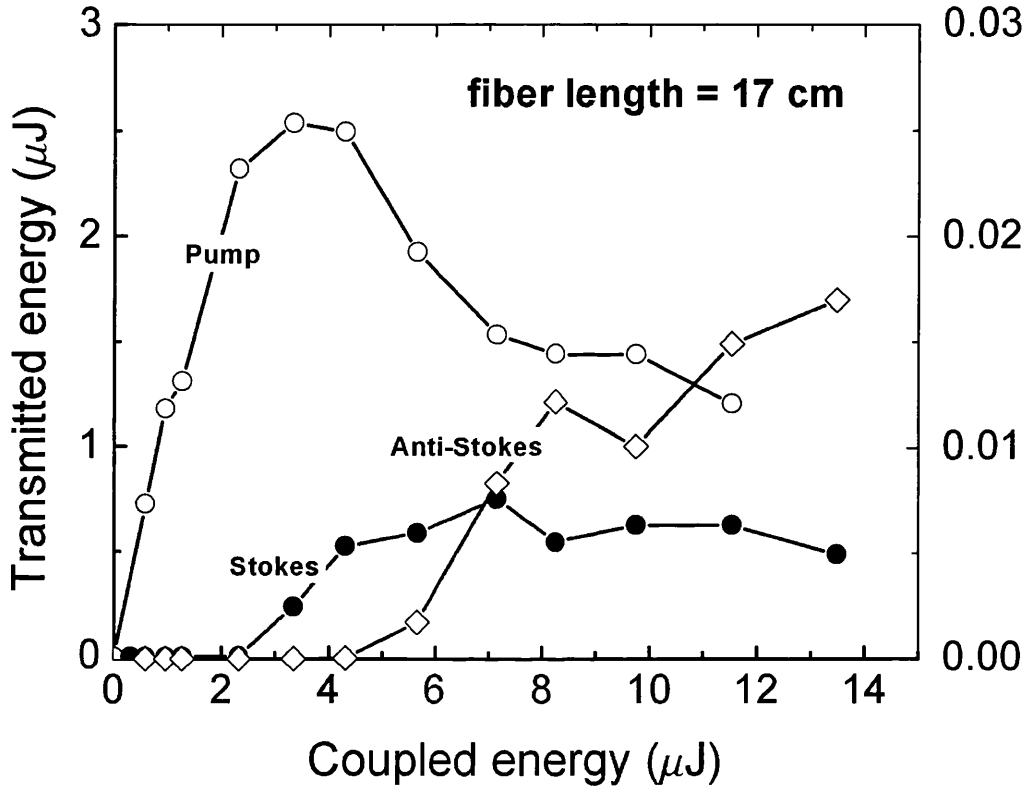

Figure 4.6: Evolution of the energy of the pump, Stokes and Anti-Stokes waves with input energy for a fibre length of 17 cm

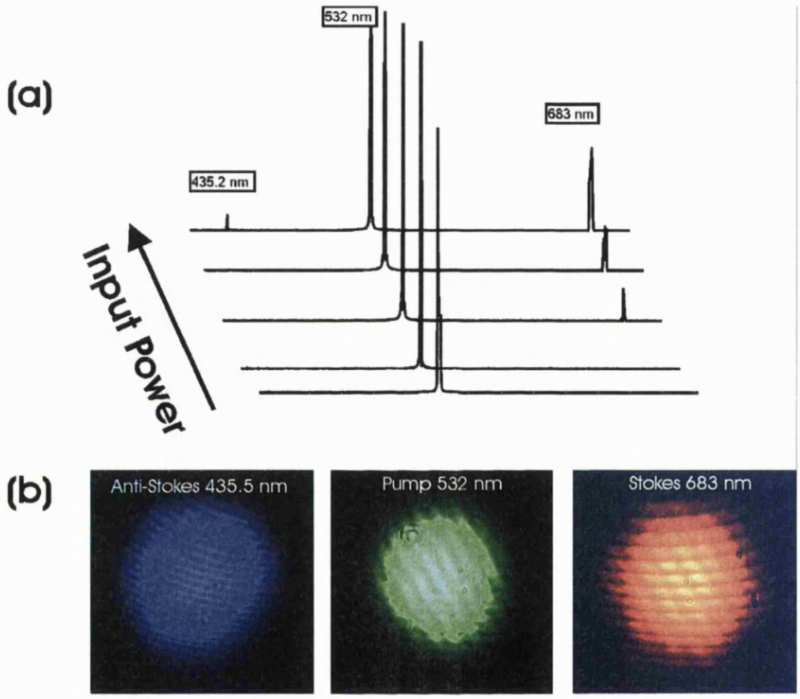

Figure 4.7: (a) Evolution of the spectrum of the light coming out of the hydrogen-filled HC-PCF with increasing input power. (b) Near-field intensity patterns at the fibre output of the pump (green pattern), Stokes (red) and Anti-Stokes (blue) fields. The streaks in the patterns are artefacts of the camera

spectively (see also Sections A.2 and A.3 of Appendix A). No rotational Raman components were observed, and that is due to two reasons: firstly, in order to efficiently generate rotational Raman bands, a circularly polarised beam is required while the polarisation of the beam in this experiment was linearly polarised (however, due to the birefringence of the fibre, some depolarisation of the input beam is expected). No backward SRS was observed, mainly due to the large linewidth of the laser (3 cm^{-1}) compared to the Raman linewidth (< 0.03 cm^{-1}) [58].

A $\times 20$ long working distance microscope objective was used to image the near-field pattern at the output end of the fibre for all three Raman components. The mode profiles recorded are shown in Figure 4.7(b). In all three cases the intensity profile peaks in the centre of the core. This is an indication that the Raman components are coupled into the fundamental mode of the HC-PCF.

Discussion of data on the transmitted power

Having looked at the behaviour of the SRS bands with input energy, their spatial evolution with propagation distance will be considered. This is shown in Figure 4.8 at an input coupled energy of 5.6 μJ, where all three signals are present inside the HC-PCF. A dramatic decrease in the pump signal is observed. The pump signal disappears over a distance of 42 cm. At the same time, up to a distance of about 30-32 cm, the energy of the Stokes wave builds up exponentially at rate similar to the attenuation rate of the pump energy. After that point the Stokes energy reaches a plateau over a distance of about 10 cm; it then drops with almost the same rate as its initial increase until it disappears at a length of 55 cm. This energy drop of the Stokes field – which is about 5 times faster then the intrinsic fibre loss rate – is accompanied by a rapid increase of the Anti-Stokes field. However the latter is too weak to account for the rapid decrease and eventual depletion of the pump and Stokes fields.

It is very likely that there is some (nonlinear) loss mechanism involved in the SRS process. This is corroborated by measurements of the total transmitted power carried out for different fibre lengths by successive cut-backs of the original length of the fibre. The results are shown in Figure 4.9, where the total transmitted energy is plotted against the input energy for different fibre lengths. Up to a value of 3 μJ coupled energy the transmitted power increases rapidly until it reaches

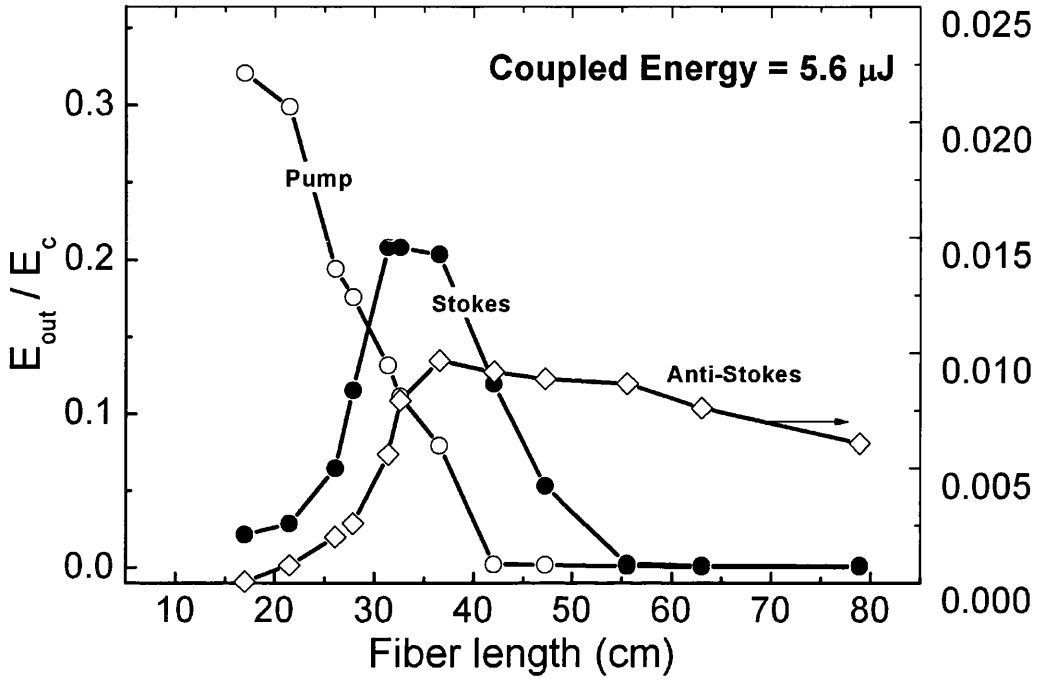

Figure 4.8: Evolution of the energy of the pump, Stokes and Anti-Stokes waves along the fibre length for an input pump energy of 5.6 μJ

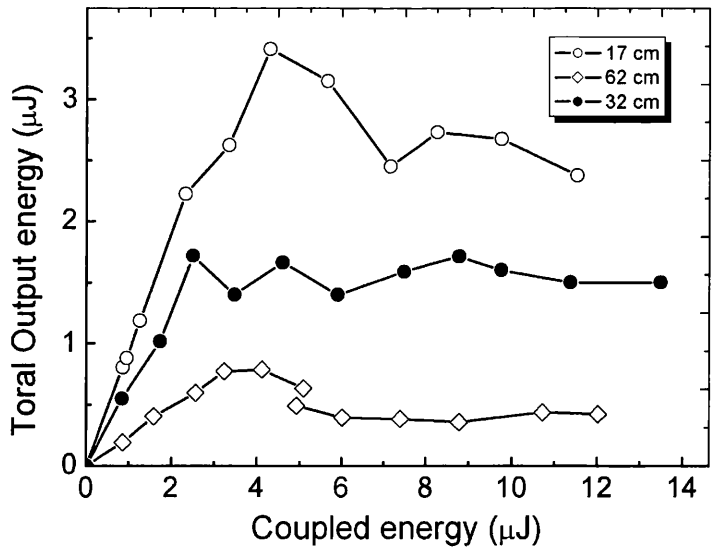

Figure 4.9: Evolution of the total transmitted energy with input energy for different fibre lengths

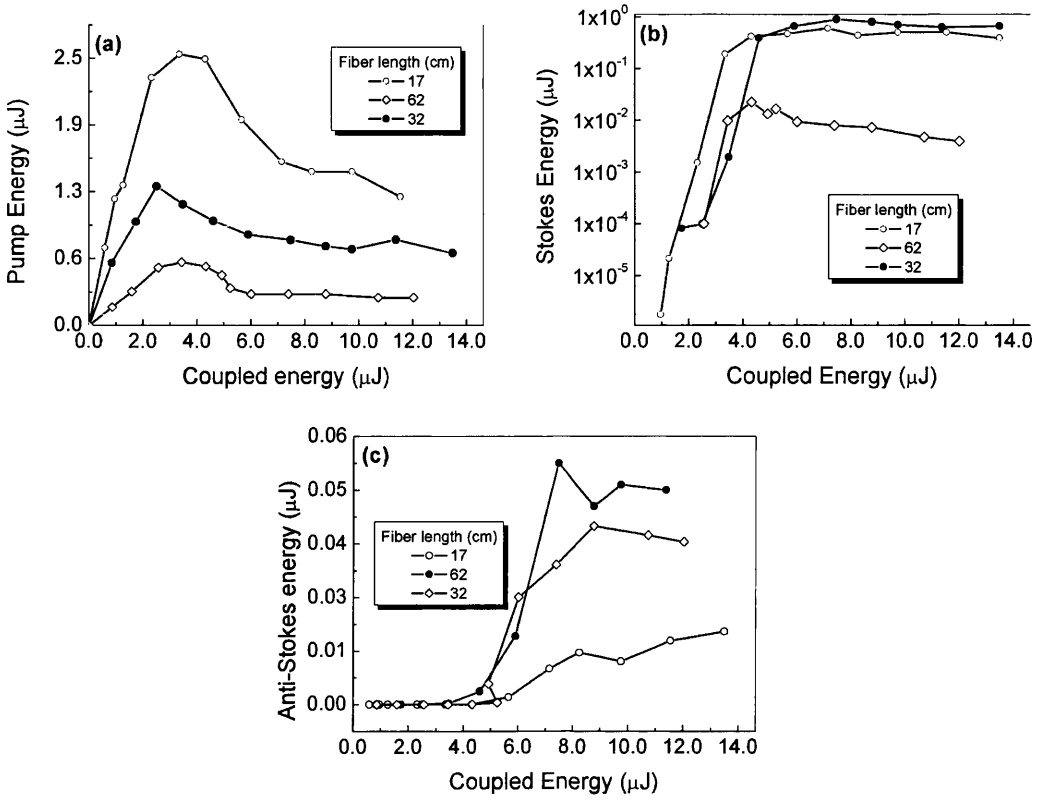

Figure 4.10: Evolution of the (a) the pump, (b) the Stokes and (c) the Anti-Stokes energy with input energy

a saturation region for input coupled energy between about 3-4 μJ. In fact, for $\mathcal{E}_c > 4$ μJ, bright scattering of the pump and Stokes from the side of the fibre was visible during the experiments. This scattering persisted for about 10 cm from its starting point which, as the coupled energy increased, moved closer to the input end of the fibre. When the input power was reduced, the transmitted power was recovered, which means that the observed saturation is not the result of fibre damage. Moreover, no higher-order Stokes or Anti-Stokes bands were observed, even though their wavelengths lie within the transmission spectrum of the Kagomé fibre (the second-order Stokes is at 953.6 nm and the second-order Anti-Stokes at 368.9 nm) and so higher-order Raman excitations cannot account for the observed saturation in transmitted energy.

This saturation region is also apparent if one looks at the evolution of each SRS band with input energy in Figure 4.10. The output pump power (plot (a)) also experiences a plateau (and subsequent drop) as the total power for the same input energy values (3-4 μJ). At input energies 4-5 μJ, the Stokes power (plot

(b)) also reaches a saturation point.

One possible explanation is that the energy loss is due to self-focusing of the laser light inside the hollow waveguide. Self-focusing is a result of the Kerr nonlinearity of the medium in which the light beam propagates, that is the dependence of the refractive index on the intensity I of the propagating field given by:

$$n = n_1 + n_2 I \ , \tag{4.7}$$

where n_1 is the linear and n_2 the nonlinear refractive index. When an intense Gaussian-like laser beam propagates in a medium the radial intensity distribution of the beam is such that, according to Equation 4.7, the edges of the beam experience a smaller refractive index than the brighter central part of the beam; this results in phase advance of the edges of the beam. In contrast, diffraction has the opposite effect, and the edges undergo phase retardation with respect to the central part of the beam. For a certain critical power, the effect of self-focusing overcomes diffraction and self-focusing occurs [59]. However, there are also nonlinear effects that put a limit to the minimum diameter of the self-focused beam. In particular, the presence of high-gain SRS limits the self-focusing process up to a certain propagation distance, beyond which the decrease in beam diameter ceases and diffraction occurs [60].

In the case of hollow waveguides, self-focusing has been interpreted as energy transfer from the fundamental to higher-order modes of the waveguide [61, 62]. The critical power for self-focusing (the power above which self-focusing is not negligible) is [61]:

$$P_{cr} = \frac{\delta\beta}{\gamma} \ , \tag{4.8}$$

where $\delta\beta$ is the difference in propagation constants between the fundamental and the higher-order mode and $\gamma = n_2\omega/(c\ A_{eff})$. The Kagomé fibre can support a low-loss ($\sim$3 dB/m) mode (HE_{11}) and a set of higher-order modes with much larger attenuations (57 dB/m for the second-order mode). If self-focusing occurs and leads to coupling to higher-order modes, then these modes will quickly be attenuated, and this could account for the plateau region in the total transmitted energy.

In order to assess whether the critical power for self-focusing is reached, Equation 4.8 is solved for coupling of the fundamental to different higher-order modes. The

Mode	$\delta\beta$ (m^{-1})	P_{cr} (W)
HE_{21}, TE_{01}, TM_{01}	7,690	491
HE_{31}, HE_{-11}	17,793	1,137
HE_{12}	21,329	1,363
HE_{-21}, HE_{41}	30,171	1,928
HE_{22}, TE_{02}, TM_{02}	37,532	2,398

Table 4.1: Table of the values of the difference in propagation constants between the fundamental-like fibre mode HE_{11} and various higher-order modes together with the respective critical powers for self-focusing

difference $\delta\beta$ is calculated by considering the modes of a straight dielectric hollow capillary: the propagation constant β_{nm} of the mode with indices n and m is given by [22]:

$$\beta_{nm} = \frac{2\pi}{\lambda}\left[1 - \frac{1}{2}\left(\frac{u_{nm}\lambda}{2\pi R_0}\right)^2\right] , \tag{4.9}$$

with u_{nm} the mth root of the Bessel J_{n-1} function and R_0 the bore radius of the fibre. The $\delta\beta$ values together with the respective critical powers are shown in Table 4.1 for $n_2 = 1.2 \times 10^{-16}$ m^2/W (at 17 bar) and A_{eff} =150 μm^2. The input energy at which saturation of the transmitted power occurs is about 3-4 μJ or 500-670 W peak power. Using the results of Table 4.1, this is above the minimum critical power and, therefore, self-focusing can occur inside the fibre and may account for the saturation plateaux observed.

Behaviour of the Anti-Stokes band

Returning to Figure 4.8 to look at the behaviour of the Anti-Stokes signal with propagation distance, it is found that the increase of the Anti-Stokes signal is much more rapid than expected theoretically: recalling Equation A.38 on page 119 of the Appendix, for constant pump I_P and Stokes I_S field intensities, the power of the Anti-Stokes field I_{AS} can be written as [11]:

$$P_{AS}(z) = \left(\frac{3\, n_2\, \omega_{AS}}{2c\, n\, A_{eff}}\right)^2 P_P^2 P_S\, z^2\, \mathrm{sinc}^2\left(\frac{\Delta\beta z}{2}\right) . \tag{4.10}$$

In the above, n_2 is the nonlinear refractive index of hydrogen (see Equation 4.7) and $\Delta\beta$ is the phase mismatch:

$$\Delta\beta = (2\beta_P - \beta_S - \beta_{AS}) - \Delta\beta^{NL} \ , \tag{4.11}$$

where the linear wavevectors (including the dispersion of hydrogen and the waveguide) are $\beta_i = \omega_i n(\omega_i)/c$. The second term in the RHS of Equation 4.11 accounts for the nonlinear phase mismatch due to nonlinear phase modulation.

The present experimental conditions are: $P_P \approx P_S \approx 100$ W, $n = 1$, $n_2 = 1.2 \times 10^{-16}$ m^2/W at 17 bar, interaction length $z \approx 0.1$ m and A_{eff} =150 μm^2. Using Equation 4.9 one finds $\Delta\beta z/2 \cong 1000$. By taking the peaks of the oscillatory sinc$x$ function one finds sinc^{2}1000 $\sim 10^{-6}$, and the Anti-Stokes power is estimated to be approximately 0.04 W, which is about 25 times smaller than the experimental value.

If the nonlinear term in Equation 4.11 is neglected, then for perfect (linear) phase-matching, the Anti-Stokes power should increase with the square of distance, according to Equation 4.10. However, as can be seen in Figure 4.8, the power of the Anti-Stokes field grows in a quadratic manner at a much more rapid rate than predicted by Equation 4.10. This can be explained either by a concurrent decrease in the phase mismatch, or by a decrease in the effective area due to self-focusing. The Stokes energy begins to drop rapidly after attaining a maximum value at about 35 cm from the fibre input end. At the same time, however, and for 35 cm $< z <$ 55 cm, the Anti-Stokes signal drops at a much lower rate (about 2 dB/m) which is actually lower than the fibre attenuation rate (3 dB/m) and this suggests that there is still Anti-Stokes gain present.

4.3 Summary and conclusions

Extremely low-threshold vibrational SRS was generated in a hydrogen-filled Kagomé HC-PCF, where both the 1st-order Stokes and Anti-Stokes bands were recorded. The pump energy threshold for the generation of the Stokes band was about 800 nJ, which is 100 times lower than ever before reported; this is because of the high FOM of the Kagomé fibre, which is about 100 times higher than other

techniques. If a fibre with even lower losses is used the enhancement factor can be even larger. The pump and Stokes fields seems to suffer some loss inside the HC-PCF, in addition to the intrinsic fibre attenuation: this is attributed to self-focusing, which is known to lead to the coupling of power to lossy higher-order modes. Estimation of the self-focusing critical power inside the waveguide corroborates this assumption. The parametric Anti-Stokes generation, on the other hand, is enhanced by the tight phase matching inside the hollow core of the fibre and experiences very rapid growth.

Chapter 5

Rotational stimulated Raman scattering in hydrogen-filled hollow-core photonic crystal fibre

In the experiments described in this chapter,[1] a comb-like SRS spectrum of 9 purely rotational SRS lines spanning a bandwidth of 80 THz is generated in a hydrogen-filled bandgap-guiding HC-PCF. A threshold power for Stokes generation of less than 10 W is demonstrated. Quasi-continuous-wave (quasi-CW) SRS was observed for pulses as long as 35 ns. In addition to the usually dominant SRS bands of ortho-hydrogen, frequencies originating from transitions of para-hydrogen were also observed at very low pump powers. Due to the 10^6 times enhancement of the FOM of the HC-PCF compared with conventional techniques, SRS is generated over long interaction lengths (10 m) and at low input powers. This brings about a new regime in the SRS dynamics, with transient behaviour observed for pulse lengths far exceeding the Raman dephasing time. In another series of experiments, the selective excitation of only the Stokes band of para-hydrogen was observed in normal hydrogen for certain pump frequencies. This was achieved for the first time in normal hydrogen.

[1]The work presented in Section 5.2 was carried out jointly by the author and Dr F Benabid. The work of Section 5.2.6 was carried out by the author. All these results have been published in [63, 64, 65]

5.1 Introduction

5.1.1 Previous work on rotational SRS in hydrogen gas

The SRS process in hydrogen is usually dominated by the vibrational Raman transitions, which have a higher gain than the rotational ones. Also the latter are sensitive to the state of polarisation of the pump beam. Rotational SRS was first observed in deuterium gas by Minck et al [66]. In experimental practice, the generation of rotational Raman frequencies required the use of special focusing geometries of the pump beam and strict control of the polarisation state of the latter [67, 68]; however, there were always vibrational Raman components present in the SRS spectrum. Only the use of a high finesse Fabry-Pérot cavity, tuned to be resonant with the rotational Stokes frequency and tightly locked to the laser frequency made possible the generation of a purely rotational SRS spectrum even though the conversion efficiency was very low ($< 5\%$) [32]. In fact purely rotational SRS had never been observed in hydrogen in a single-pass configuration before the use of HC-PCF [12]. In that work, extremely low-threshold purely rotational SRS was demonstrated in a hydrogen-filled HC-PCF. The latter had a narrow enough bandwidth so that only the rotational SRS bands would be transmitted. The set-up was similar to the one described in this chapter. Apart from a 10^6 times reduction in threshold energy for Stokes generation from previously published results, this work also demonstrated the extremely high conversion efficiency achievable with the HC-PCF (92%, almost quantum limited).

5.2 Results and discussion

The very high FOM of the HC-PCF establishes a novel regime for SRS. In particular high Raman gain is achieved for relatively low input powers. Using the expression A.34 of the Appendix for the net Raman gain in the steady-state:

$$G = g_R \frac{P_P}{\pi R_0^2} z \ , \tag{5.1}$$

for typical experimental values $g_R = 3$ cm/GW [32], P_P=100 W, core radius $R_0 = 3.5$ μm and $z = 10$ m, gives $G \cong 100$. Under these conditions of high gain,

long interaction lengths and low powers, the following points are investigated in this chapter: the generation of a quasi-CW comb-like purely rotational SRS spectrum, the novel dynamics of Stokes amplification, the effect of GVD and fibre birefringence on the SRS gain, the temporal shape of the Raman pulses and the selective excitation of the Stokes band of para-hydrogen. Before all these a description of the experimental configuration is first presented.

5.2.1 Experimental set-up

As in the experiments described in the previous chapter, here a HC-PCF ws also filled with hydrogen gas. The fibre used is the same as the one used in [12] and is shown in Figure 2.6 on page 12 together with its transmission spectrum: this is a bandgap-guiding HC-PCF with a transmission window about 300 nm wide centred around the wavelength of 1060 nm. The lowest attenuation rate of the fibre is 65 dB/km near the centre of the bandgap with a core diameter of 7 μm. This offers a FOM enhancement factor of about 10^6 compared with conventional techniques (see Figure 2.13(b) on page 22). The fibre was filled with hydrogen gas in the way described in Section 4.2.2.

The experimental set-up for the acquisition of the spectra emerging from the hydrogen-filled HC-PCF is shown in Figure 5.1.The pump laser source was a Q-switched Nd:YVO_4. This is a compact-sized diode-pumped system producing low-energy pulses at 1047 nm of varying repetition frequency and duration. The repetition frequency of the laser output varied from 1-50 kHz with a concurrent variation of the pulse width in the region 6.5-35 ns. The pulse energy varied with pulse width with a maximum energy of less than 100 μJ. The laser could also operate in CW mode. The laser beam was in a Gaussian TEM_{00} mode. The output pulse repetition frequency of the laser could be varied from 1 Hz to 50 kHz. Changing the repetition frequency also changed the pulse duration. The pulse width emerging from the laser was measured for the whole range of repetition frequencies and the data are shown in Figure 5.1.

A polarising beam-splitter and a half-wave plate are used to control the pump power entering the fibre. By means of a rotating quarter-wave plate the state of polarisation of the input light can change from linear to elliptical or circular. A flipper mirror is used to send the input beam into a power meter in order

(a)

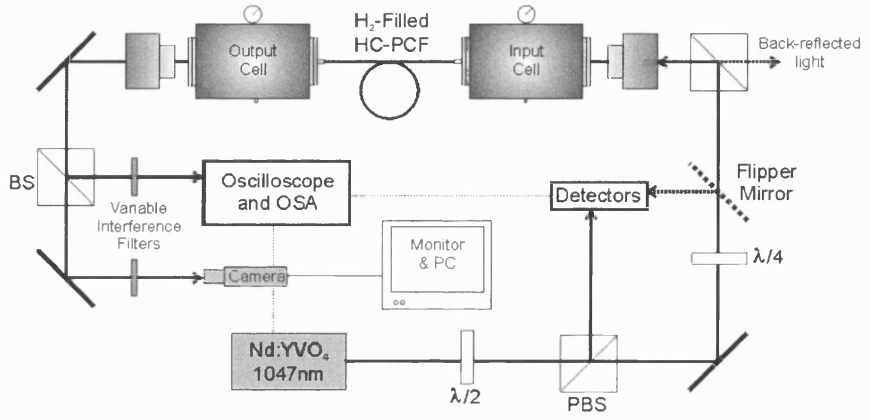

(b)

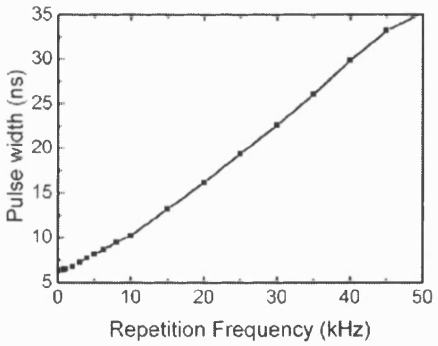

Figure 5.1: (a) Experimental set-up for acquisition of SRS spectra and measurement of threshold energy. (b) Variation of the pulse width of the laser source with repetition frequency

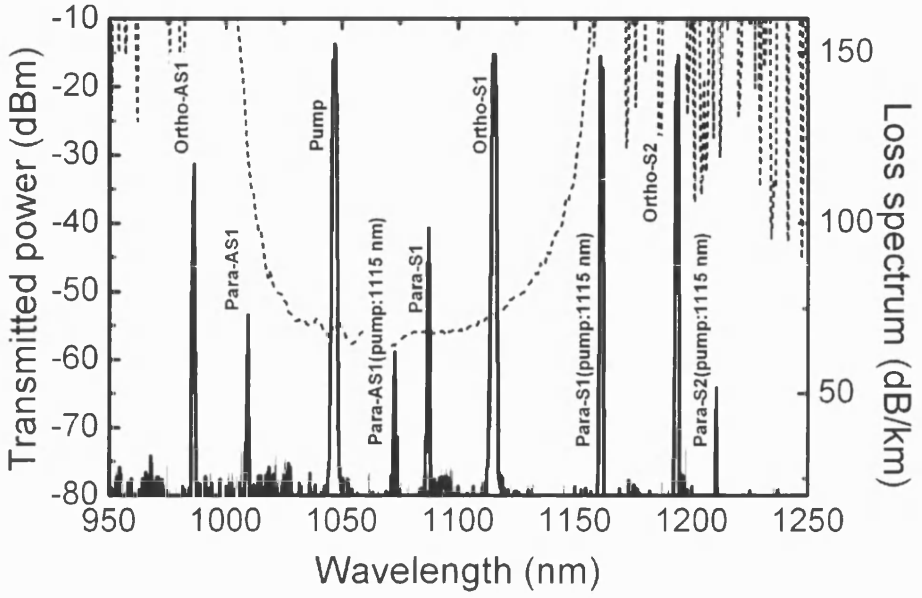

Figure 5.2: Typical output SRS spectrum of a 10 m-long HC-PCF filled with hydrogen at a pressure of 12 bar. The pump pulse width is 7 ns and the pump energy is about 4 μJ. S1, S2, AS1 and AS2 stand for first-, second-order Stokes and first- and second-order Anti-Stokes respectively

to monitor the input power. The pump light is coupled into the fibre through the window of the hydrogen cell using a microscope objective lens. The output light is then collected and sent to an optical spectrum analyser (OSA) and power detectors after passing through different interference filters in order to select different frequencies of the output spectrum.

5.2.2 The SRS spectrum

A typical output spectrum for a relatively short pump pulse width (7 ns) is shown in Figure 5.2. It consists of a comb of nine spectral peaks spanning a frequency range of 80 THz. The SRS peaks correspond to different rotational transitions of the hydrogen molecules. In particular, the first-order Stokes bands both the $S_{00}(1)$ and the $S_{00}(0)$ rotational Raman transition were observed. The new frequencies pumped by the input laser field correspond to Stokes and Anti-Stokes transitions due to four-wave mixing. The various peaks are labelled on the spectrum of Figure 5.2.

The first-order $S_{00}(1)$ Stokes wave (ortho-S1) at 1115 nm (pumped by the laser source) grew to the extent of subsequently generating new Raman frequencies (cascade SRS). These frequencies correspond to both types of rotational Raman transitions. Furthermore, the first-order $S_{00}(0)$ Stokes wave (para-S1) at 1161 nm (pumped by the ortho-S1 wave at 1115 nm) is stronger than the corresponding para-S1 transition at 1084 nm pumped by the input laser field. This is due to the transmission spectrum of the fibre: in general, the $S_{00}(1)$ transitions are the most efficient ones, due to the 3:1 ratio of ortho- to para-hydrogen. Therefore, these transitions will dominate, until the pump wave acquires a frequency for which the higher-order $S_{00}(1)$ transitions lie outside the low-loss region of the fibre transmission spectrum. In that case the $S_{00}(0)$ transition will be enhanced. This shows how the effect of the fibre transmission properties can be used to suppress an otherwise dominant Raman transition in favour of a weaker one. This effect will be further investigated in another series of experiments described in Section 5.2.6.

The evolution of each one of these peaks with increasing input pump power is shown in Figure 5.3(a). Neutral density filters were used after the fibre output to prevent the detector from saturating. The strong ortho-S1 wave grows to the extent of surpassing the output power of the pump field at an input pump energy of around 2.4 μJ (Figure 5.3(b)). The pump power at the fibre output quickly reaches a saturation plateau at an input power of about 450 nJ.

Near-field intensity profiles

Profiles of the near-field intensity distribution at the output face of the fibre were acquired by collecting the emerging light with a microscope objective and sending it to an infrared-sensitive camera (see Figure 5.1). The near-field profiles for the pump, ortho-S1 and ortho-S2 fields, taken using interference filters, are shown in Figure 5.4. Both the pump and ortho-S1 fields couple to the fundamental mode of the HC-PCF, as their frequencies are well centred near the middle of the fibre bandgap. However, the ortho-S2 field is coupled to a higher-order mode, as it is located near the long-wavelength edge of the fibre bandgap. This is due to the finger-like shape of the bandgap as illustrated in Figure 5.5: on the long-wavelength side of the propagation diagram, the fundamental mode is cut off at shorter wavelengths than the second-order mode.

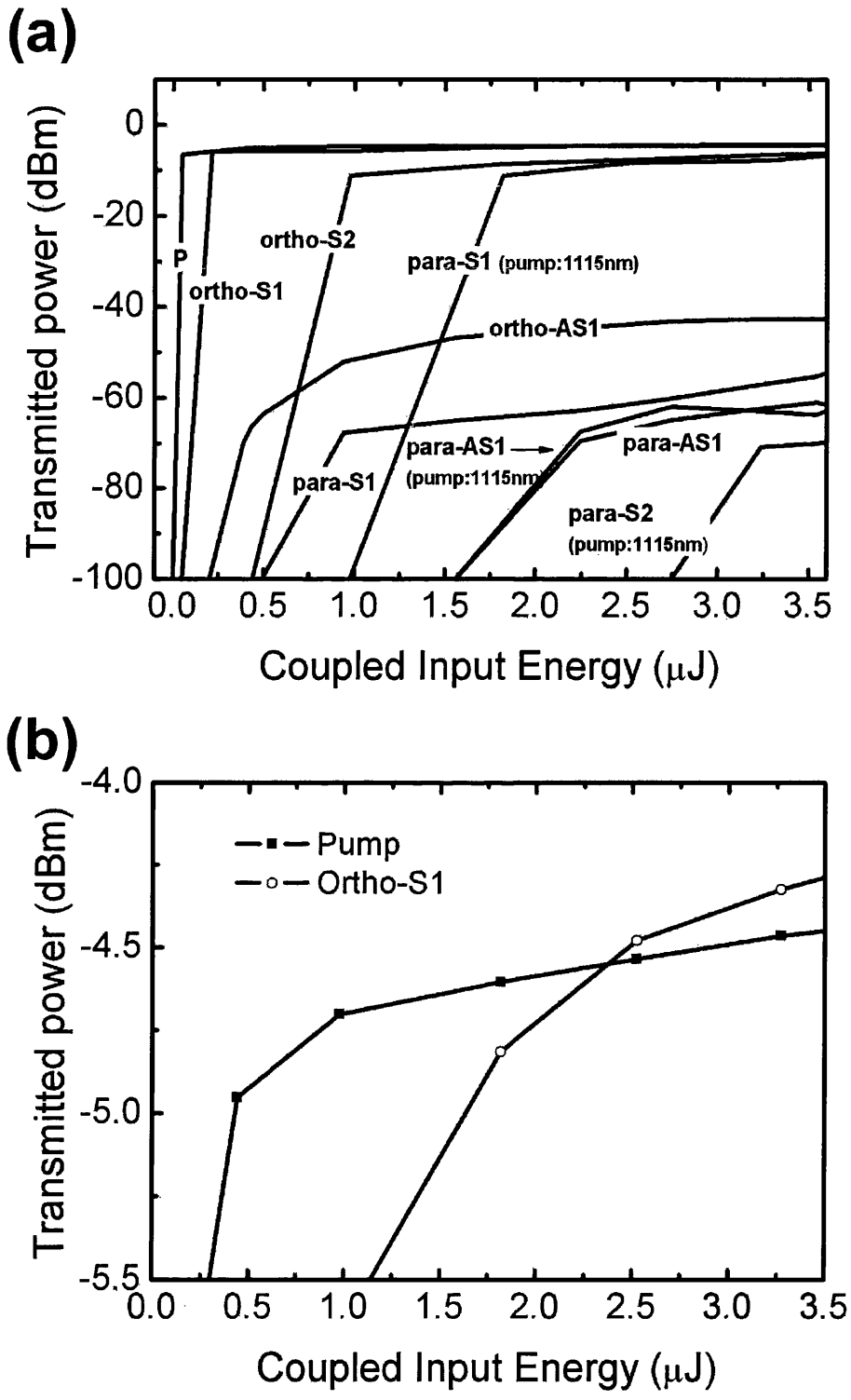

Figure 5.3: (a) Evolution of the power at the different Raman frequencies with input pump power. (b) An enlarged detail of the previous plot showing the growth of the ortho-S1 power above the power level of the pump

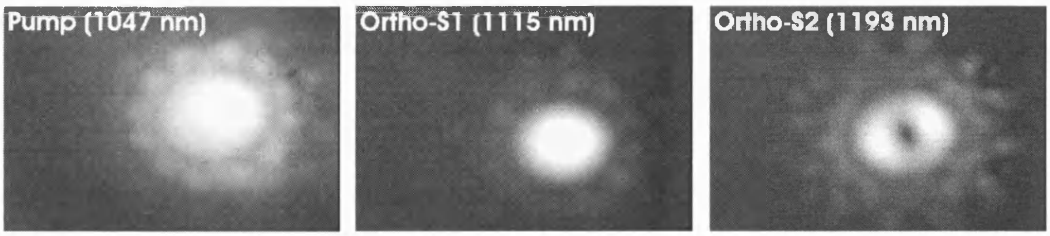

Figure 5.4: Profiles of the near-field intensity distribution of the pump, ortho-S1 and ortho-S2 fields at the fibre output

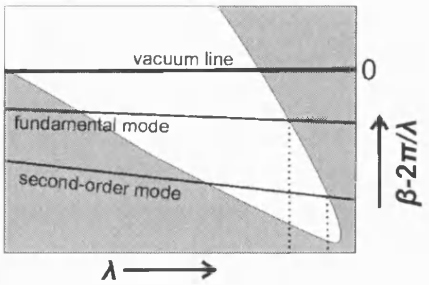

Figure 5.5: Schematic dispersion plot of a HC-PCF with a full PBG (white region) demonstrating that, on the long-wavelength side of the plot, the fundamental mode is cut off at a shorter wavelength than the second-order mode

5.2.3 Threshold energy measurements

Apart from the generation of quasi-CW, comb-like, purely rotational SRS spectra, the very high FOM of the HC-PCF can also affect the dynamics of the amplification of the Stokes field. SRS has been mainly studied for very short interaction lengths and high input powers. Under these circumstances it is generally assumed that the SRS process reaches its steady-state limit when the interaction time-scale (the pulse duration of the pump laser) is larger than the dephasing time T_2, which is then identified with the relaxation time of the Raman transition (inverse of the Raman linewidth). However this may not always be the case: temporal analysis of the SRS process [69, 70] shows that for very large interaction lengths the scattering process may still exhibit transient behaviour even for pulse widths largely exceeding the dephasing time (see Appendix B and Figure 5.6(a)). It is noteworthy that for an interaction length of 1 km (a realistic length with the low-loss fibres currently available) the steady-state is only reached for pulses as long as 200 ns, four orders of magnitude longer than the dephasing time $T_2 = 200$ ps of the rotational transition in hydrogen.

In order to investigate the Stokes amplification dynamics in the present experi-

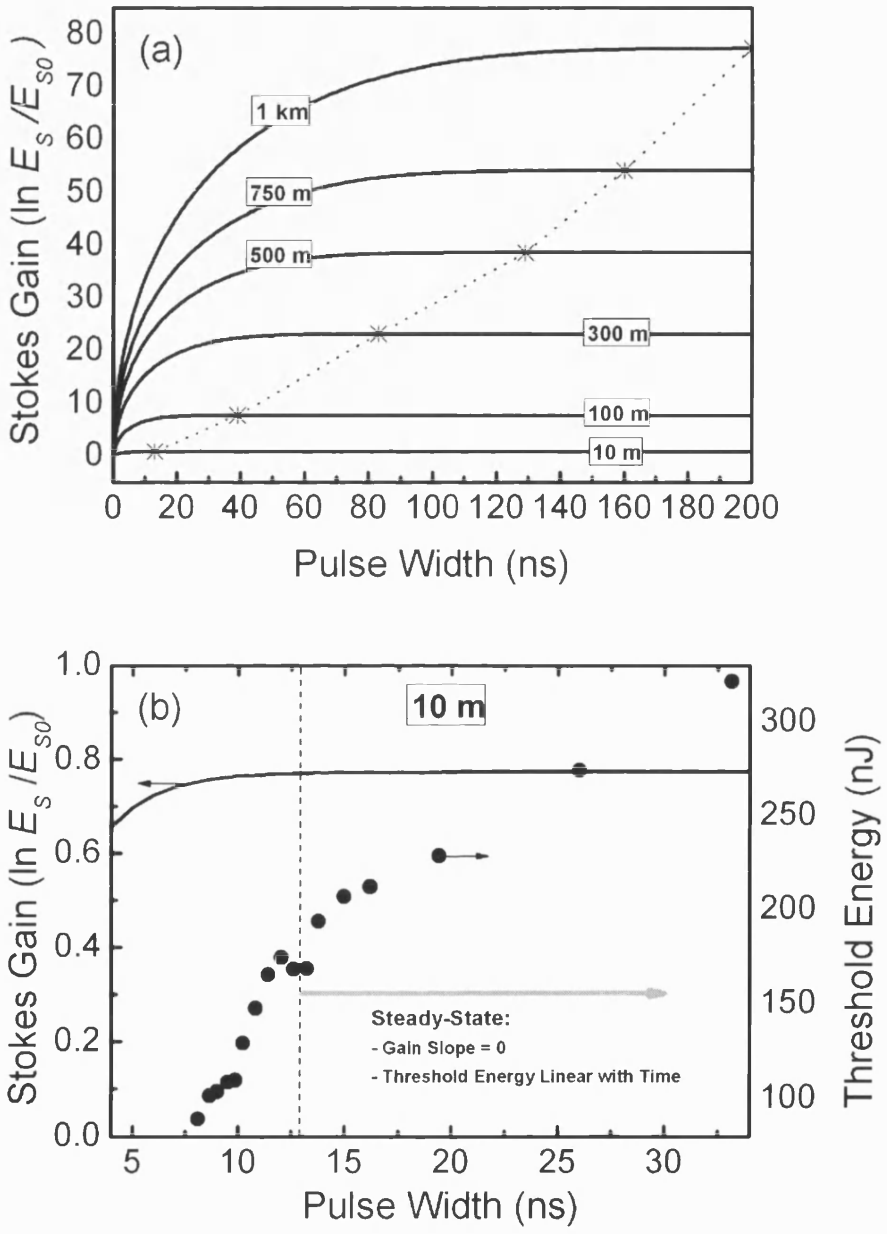

Figure 5.6: (a) Stokes gain versus pump pulse width for different fibre lengths at 10 W input power as calculated using Equation B.4 on page 120 [69]. The points show where the steady-state is reached (gain independent of time). (b) For an interaction length of 10 m the steady-state is reached for pulse widths around 13 ns, which coincides exactly with the experimentally observed transition of the dependence of threshold energy on time from transient to steady-state

mental set-up, threshold energy measurements for Stokes generation were taken for different pulse widths. Moreover, the experimental results were compared with theoretical models.

Experimental procedure and results

The pump threshold energy for the generation of the first Stokes frequency of the $S_0(1)$ rotational Raman transition was measured using the set-up shown in Figure 5.1. As with the acquisition of the output spectra, the input pump power was varied by rotating the half-wave plate before the polarising beam-splitter and the output light was collected and fed to a spectrum analyser and power detectors. The detected signal at the Stokes wavelength was monitored as the input power was varied from values below the threshold, where no Stokes signal was detected, up to the threshold point where the Stokes signal emerged abruptly.[2] This procedure was repeated for different laser pulse widths in the entire available range of 6-35 ns.

The threshold energy was measured for a range of different pulse widths for a HC-PCF of length $L = 12$ m filled with hydrogen gas at pressure $p = 12$ bar. The acquired threshold data are shown in Figure 5.7. The pump threshold energy varies from about 90 nJ (13.8 W peak power) for the shortest pulses (6.5 ns) up to about 320 nJ (9 W peak power) for the longest pulses (35 ns).

In order to theoretically investigate the threshold dependence on time, the results of Raymer et al [70] are employed: there, the SRS process is described quantum mechanically, encompassing the whole range of temporal domains including the spontaneous initiation and the transient and steady-state regimes. Transient behaviour is expected for pulse widths between $\tau_1 = (g_R I_P z \Gamma)^{-1}$ and $\tau_2 = g_R I_P z \Gamma^{-1}$, where $\Gamma = (2\pi T_2)^{-1}$ is the linewidth of the Raman transition. Below τ_1, the scattering is spontaneous and the Stokes power is given by:

$$P_{S0} = \frac{1}{2}\Gamma h v_S \ , \tag{5.2}$$

with v_s the Stokes frequency. The spontaneous Stokes noise found using this last equation is 1.4×10^{10} W.

[2]The threshold energy has already been defined in the footnote of Section 4.2.3 on page 53

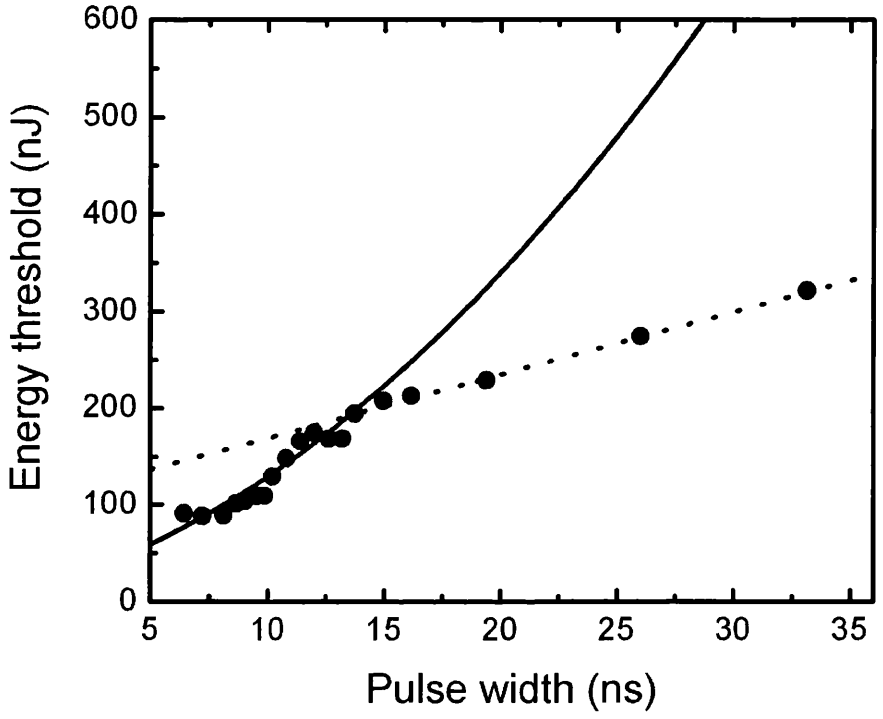

Figure 5.7: Measured pump energy at threshold for the generation of the first-order $S_{00}(1)$ Stokes wave versus pump pulse width. The dotted line shows a plot of the theoretical steady-state threshold energy with time (Equation 5.7) and the solid curve is the theoretical transient threshold energy (Equation 5.8)

In the high-gain limit ($g_R I_P z \Gamma \tau \gg 1$), the Stokes power in the transient regime is given by:

$$P_S^t(z,\tau) \approx h\nu_S \frac{\exp\left(2\sqrt{2\, g_R\, I_P\, z\, \Gamma\, \tau} - 2\Gamma\tau\right)}{8\pi\tau} \ , \tag{5.3}$$

For pulses longer than τ_2, the SRS reaches its steady-state and the Stokes power is given by the well-known equation for steady-state amplification (see Section A.2 of the Appendix):

$$P_S^{ss}(z,\tau) \approx h\nu_S \frac{\Gamma}{2\sqrt{\pi\, g_R\, I_P\, z}} \exp(g_R\, I_P\, z) \ . \tag{5.4}$$

Analytical expressions for the threshold energy versus pulse width can be derived for each of these temporal regimes: it is assumed that the Stokes field intensity experiences exponential amplification:

$$I_S = I_{S0}\, e^{G_{th}} \ , \tag{5.5}$$

with G_{th} the gain at threshold. This gives:

$$\ln\left(\frac{I_S}{I_{S0}}\right) = G_{th} = \text{constant} \ . \tag{5.6}$$

Using the above threshold condition for the steady-state (Equation 5.4) yields the threshold energy:

$$\mathcal{E}_{P,th}^{ss}(\tau) = \frac{G_{th}\, A_{eff}}{g_R\, L_{eff}}\, \tau + \mathcal{E}_0 \ . \tag{5.7}$$

The energy offset $\mathcal{E}_0$ for $\tau = 0$ is added empirically and accounts for the offset between the Stokes intensity in spontaneous and steady-state scattering. The slope of the equation corresponds to the steady-state power threshold. Equation 5.7 is the same as the one found in [71] and is also used later in the chapter (Equation 5.10). The energy $\mathcal{E}_{P,th}^{ss}(\tau)$ is plotted in Figure 5.7 (dotted line) for $G_{th} = 20$, $g_R = 3$ cm/GW [32], $\mathcal{E}_0 = 90$ nJ and a core diameter of 7 μm is shown. L_{eff} is the effective interaction length of the SRS process, after taking into account the fibre loss, and equals $\frac{1-\exp(-\alpha_P L)}{\alpha_P}$, with α_P the exponential attenuation coefficient at the pump frequency (the fibre loss is 70 dB/km at 1047 nm, which gives $\alpha_P = 0.016$ m^{-1}). This gives an effective length of about 10 m. There is excellent agreement between the calculated steady-state threshold energy and the experimental points for $\tau > 12 - 14$ ns.

The threshold condition (Equation 5.6) in the transient regime (Equation 5.3)

gives a threshold energy that is quadratic with time:

$$\mathcal{E}^{t}_{P,th}(\tau) \approx \frac{A_{eff}}{2\Gamma\, g_R\, L_{eff}} \left[G_{th} + \ln(4\pi\Gamma\tau) + 2\Gamma\tau\right]^2 \ . \tag{5.8}$$

A plot of this last equation is also shown in Figure 5.7 (solid curve) for $G_{th} = 20$; it describes very well the behaviour of threshold energy with time for pulses shorter than 12-14 ns. The very good fit of Equation 5.7 for $\tau > 14$ ns and Equation 5.8 for $\tau < 14$ ns is a further indication for the transition of the SRS process from steady-state to transient around that pulse width. This turning point is found to be the same as the time τ_2 mentioned above, where transition from transient to steady-state takes place. It is also the same pulse width calculated using the results of [69], as can be seen in Figure 5.6(b), where the change of the temporal behaviour of the Raman gain around 12-14 ns is a fingerprint of the transition from transient to steady-state SRS.

All these results demonstrate the novel dynamics of the Stokes amplification in this set-up of very long interaction lengths and low input power. Transient SRS occurs for pulses as long as 14 ns, well above the dephasing time of the Raman excitation.

5.2.4 Factors affecting the SRS gain inside the fibre

Inside the waveguide, effects such as group velocity dispersion (GVD) and birefringence can affect the SRS gain. The gain reduction factor R can be used to estimate the reduction of the experimental SRS gain. It is assumed that the net Raman gain G_{exp} is reduced from its steady-state value G_{ss} by a factor R:

$$G_{exp} = R(\tau)\, G_{ss} \ , \tag{5.9}$$

where R varies from 0 to 1. In the context of stimulated scattering, the gain reduction was first used to study the effect of phonon lifetime on SBS and SRS [72]. Here the derivation of the experimental gain reduction follows the method of [71]. A linear fit is performed to the threshold data measured at the longest pulse widths (see Figure 5.7), the slope of which is taken to be equal to the steady-state threshold power $P_{ss,th}$:

$$\mathcal{E}_{th}(\tau) = \mathcal{E}_0 + P_{ss,th}\, \tau \ . \tag{5.10}$$

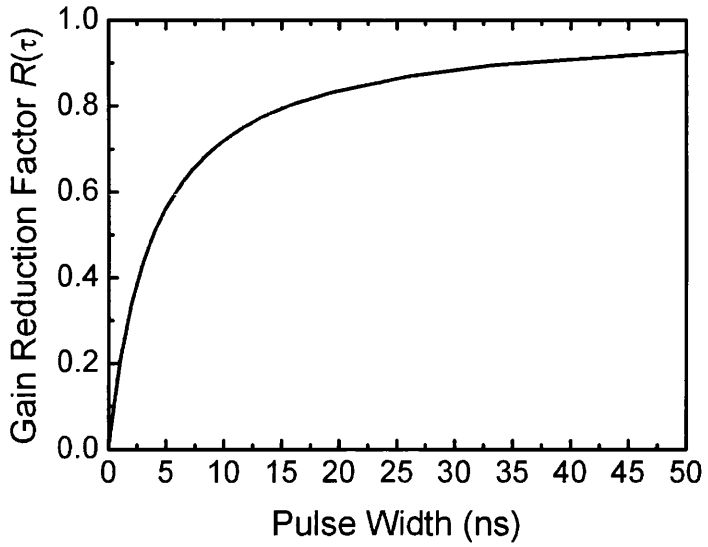

Figure 5.8: Experimental gain reduction factor (Equation 5.11) as calculated from the fitting parameters of the experimental threshold data (Figure 5.7)

Then the gain reduction factor $R(\tau)$ will be given by [71]:

$$R(\tau) = \left(1 + \frac{\mathcal{E}_0}{P_{ss,th}\,\tau}\right)^{-1} . \tag{5.11}$$

The experimental gain reduction curve (5.11) is shown in Figure 5.8 (solid line). The gain reduction curve (5.11) is extrapolated in the plot for pulse widths outside the experimental range. It shows the reduction of the Raman gain even in the steady-state regime. This reduction may be due to GVD and fibre birefringence and these effects will now be investigated.

Effect of linear dispersion on the SRS gain

So far, the effect of the chromatic dispersion of the fibre on the SRS process has not been considered. In general, pulses centred at different frequencies will travel with different group velocities due to the dispersion of the waveguide. The dispersion parameter D of the HC-PCF used in these SRS experiments was measured by Dr Fetah Benabid using a low-coherence interferometric technique and is shown in Figure 5.9. The dispersion parameter, has already been defined

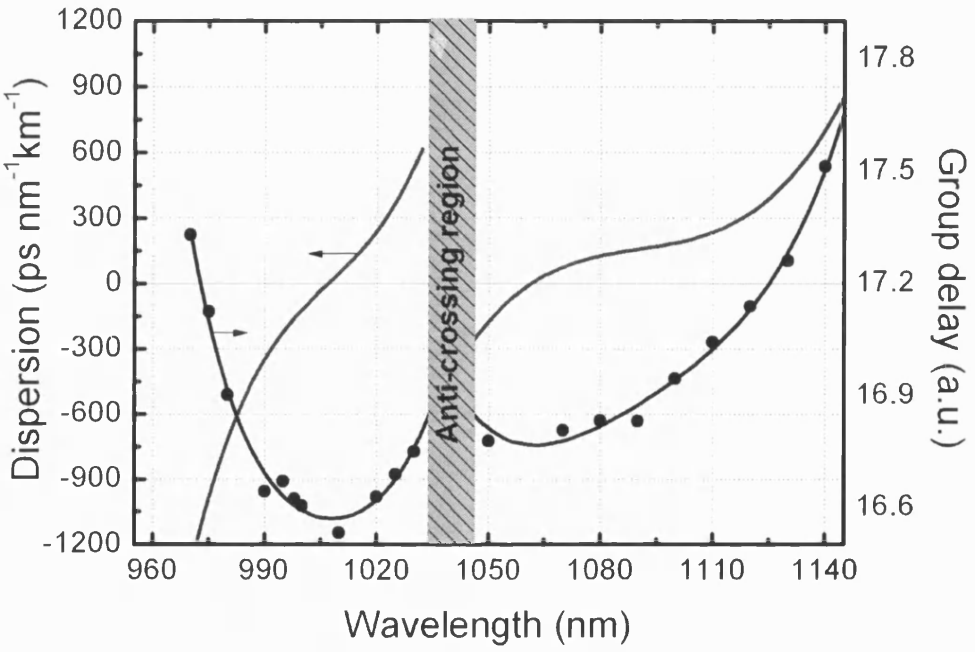

Figure 5.9: The experimental group delay (right vertical axis) and dispersion parameter (left axis) of the fundamental mode of the HC-PCF used in the rotational SRS experiments. The shaded box is a region of anti-crossings with surface modes, where the dispersion varies in a complex manner

on page 17 as:

$$D = \frac{d\,(u_g^{-1})}{d\,\lambda}\ , \tag{5.12}$$

where u_g is the group velocity. The fibre dispersion has a direct effect on the SRS gain as can readily be seen by looking at the driving term of the molecular excitation (proportional to the product of the fields $\mathbf{E}_P\mathbf{E}_S^*$, as in Equation A.14 on page 115 of the Appendix). In the absence of group velocity dispersion, the phases of the pump and Stokes waves adjust to produce maximum gain [73]. However, the presence of group delay will affect the relative phase of the pump and Stokes waves and will, thus, reduce the gain from its dispersionless value. This happens both in the transient and the steady-state.

Two competing characteristic lengths can be defined: a Raman length, $L_R = (g_R\ I_P)^{-1}$, which is a characteristic length-scale for the (dispersionless) amplification of the intensity of the Stokes field, and a phase destruction length L_{des} (over which dispersion effects destroy the phase relationship between the two waves). The latter is found to be [73, 74]:

$$L_{des} = \frac{\pi}{\left|u_P^{-1} - u_S^{-1}\right| \Delta\omega}\ , \tag{5.13}$$

with $\Delta\omega$ the bandwidth of the pump laser (215 GHz in this case) and $u_{P,S}$ the group velocities of the laser and Stokes pulses respectively. The values of the dispersionless gain will apply only for $L_R \ll L_{des}$. The Raman length for the typical peak power of the pump pulses (10 W) is:

$$L_R = (g_R\ I_P)^{-1} = (g_R\ P_P/A_{eff})^{-1} \cong 250 \text{ mm}\ . \tag{5.14}$$

The group velocity mismatch $u_P^{-1} - u_S^{-1}$ can be calculated by using the experimental data of Figure 5.9 and Equation 5.12, from which it is found to be:

$$u_P^{-1} - u_S^{-1} \cong (D_P - D_S)\,\Delta\lambda\ , \tag{5.15}$$

with $D_{P,S}$, the dispersion at the pump and Stokes frequencies respectively and $\Delta\lambda$, the corresponding difference in wavelength. From the experimetal data it is found that $D_P - D_S = [-240 - (+272)]$ ps nm^{-1}km^{-1} = –512 ps nm^{-1}km^{-1}. This gives, using Equation 5.13:

$$L_{des} \sim 10^2 \text{ m}\ , \tag{5.16}$$

which is far longer than the Raman length. Therefore, the effect of the linear dispersion is very small in the present experiments.

Effect of fibre birefringence on the SRS gain

The fundamental mode of an optical fibre consists of a pair of modes with orthogonal polarisation states. Slight anomalies in the fibre core such as twists, bends and stress can induce a certain degree of symmetry breaking and the fibre becomes birefringent. The two orthogonal modes thus acquire slightly different propagation constants; this eventually leads to a change in the state of polarisation of the output light.

If linearly polarised light is launched into a birefringent optical fibre, it becomes elliptical over a short distance. Circularly polarised input light will change its state of polarisation periodically as it propagates along the fibre [26]. The length after which a given state of polarisation repeats itself is called the beat-length, L_B, and it is a measure of the birefringence of the fibre (the shorter the beat-length, the higher the birefringence). It is written as [28]:

$$L_B = \frac{2\pi}{\Delta\beta} = \frac{\lambda}{n_x - n_y} , \tag{5.17}$$

where $\Delta\beta$ is the difference in propagation constants between light polarised along the x and y axes of the elliptical fibre core, with n_x and n_y the respective modal indices.

The rotational SRS gain depends on the state of polarisation of the pump beam. This was first observed experimentally [66] and was later described mathematically [75]. There it was shown that the maximum rotational SRS gain ($g_{R,max}$) is obtained for a circularly polarised beam with a co-propagating circular Stokes field of opposite sense. In this case, and in the presence of the Anti-Stokes band, the Raman gain is independent of the phase-mismatch $\Delta k = 2k_L - k_S - k_{AS}$. For plane-polarised pump light the maximum gain occurs for Stokes light linearly polarised in the same plane of polarisation; in this case the gain is strongly dependent on phase-mismatch and goes from zero at complete phase-matching (due to four-wave mixing Raman gain suppression) to a maximum value of $\frac{2}{3}\, g_{R,max}$ away from phase-matching. The gain coefficients (normalised to $g_{R,max}$) for dif-

Pump Polarisation	Stokes Polarisation	g_R / $g_{R,max}$
+	−	1
+	+	1/6
x-polarised	x-polarised	2/3
x-polarised	y-polarised	1/3

Table 5.1: Raman gain coefficient for rotational SRS for different states of polarisation of the pump and Stokes beams, in the presence of the pump, Stokes and Anti-Stokes fields and away from phase-matching

ferent pump light polarisations and away from phase matching are summarised in Table 5.1. These values correspond eventually to the ratios of spontaneous Raman cross-sections.

From the above, it is obvious that the gain for rotational SRS will be affected by any change in the state of polarisation of the pump field due to the presence of fibre birefringence. That the fibre is birefringent was immediately clear, as circularly polarised input pump light was found to be elliptical at the fibre output. In order to investigate the effect of the fibre birefringence on the SRS gain, the Raman length (Equation 5.14) can be compared to the beat-length, L_B, of the fibre. For $L_R \gg L_B$, any polarisation effects are expected to average out as the state of polarisation of the laser field is varied.

The birefringence of the HC-PCF was estimated by direct measurement of the fibre beat-length using the following method. Exerting pressure at some point in the fibre will cause stress-induced birefringence, which in turn will affect the polarisation state of the output light. For an otherwise perfectly cylindrically symmetric fibre core, moving the pressure point along the fibre would not result in any additional change in the polarisation of the output light. However, in the presence of intrinsic birefringence in the fibre structure, the state of polarisation of the output light should change as the pressure point moves along the fibre. This change of polarisation is monitored by using a linear polariser at the fibre output at a fixed angle with respect to the direction of the output beam. As the polarisation of light changes periodically with the movement of the pressure point in a birefringent fibre, the component of the output light polarised parallel to the plane of the linear polariser will also vary periodically. From the variation of the output intensity recorded after the polariser, an estimate of the beat-length of the fibre can be deduced.

The experimental set-up for measuring the fibre birefringence is shown in Figure 5.10(a). The polarisation of the input beam was changed to circular with a quarter-wave plate and a linear Glan polariser was used at the output to select a specific plane of polarisation of the output beam. The input beam was modulated by means of an optical chopper connected to a lock-in amplifier. A pointed stub was mounted onto a translation stage and was used to apply pressure at a certain point of the fibre so as to induce some degree of extrinsic birefringence at that point. The stub was moved in steps of 2 mm. The light emerging from the fibre was collected and collimated by a microscope objective and passed through the linear polariser. The laser used was the same Nd:YVO_4 laser at 1047 nm, but operating in CW mode. The output light was split into two beams by a beam-splitter and one beam was sent to a CCD camera connected to a monitor in order to image the near-field intensity pattern at the fibre output. The other beam was coupled by means of another microscope objective lens to a single-mode conventional fibre pigtailed to a femtowatt receiver. The signal from the receiver was fed to the lock-in amplifier. The voltage read on the lock-in amplifier was acquired at each step of the moving stub.

The variation of the voltage with the position of the pressure point along the fibre is shown in Figure 5.10(b). The period of the signal, and thus the fibre beat-length, was found to be 30 mm. This is an order of magnitude smaller than the Raman length (250 mm, see also Equation 5.14) and helps explain the small role of the fibre birefringence in these experiments. The gain reduction even in the steady-state observed in Figure 5.8 may be affected by the fibre birefringence, however it should be noted that this may also be related to some uncertainty on the exact magnitude of the gain coefficient, which is found in the literature to vary between 1-5 cm/GW [67, 32]. Fibre birefringence should always be taken into consideration when a HC-PCF is used in SRS. The birefringence of a HC-PCF is found to be strongly dependent on wavelength, and it is one of the reasons why many fewer Raman bands were observed in [12] with a pump wavelength of 1064 nm, where the beat-length is much larger than at 1047 nm.[3]

[3]From discussions with Dr F. Benabid

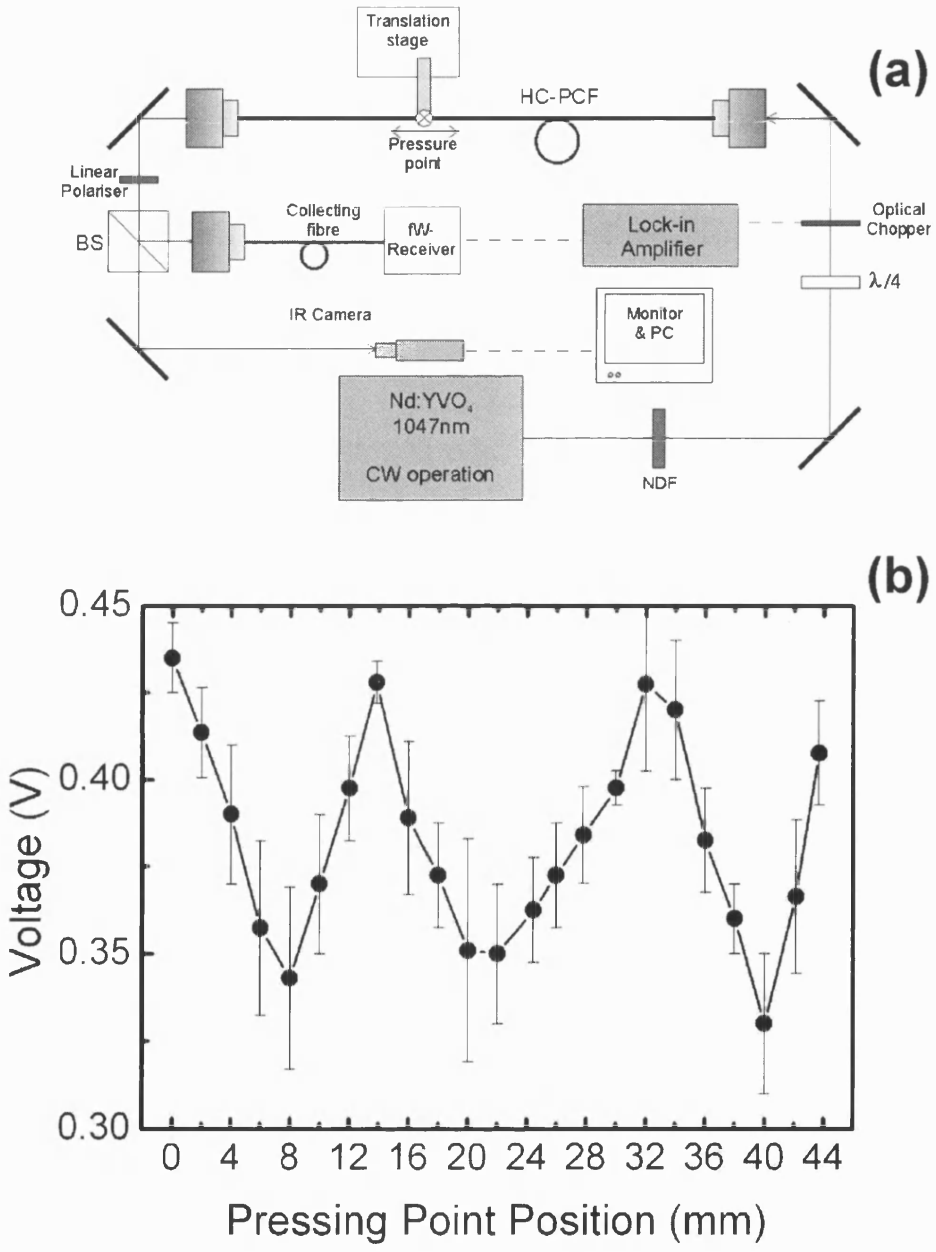

Figure 5.10: (a) Set-up for measurement of the fibre beat-length. (b) Variation of the detected signal with the position of the moving pressure point along the fibre for estimation of the fibre beat-length. The laser wavelength is 1047 nm. The period of the variation gives the fibre beat-length and is in the region 30-32 mm

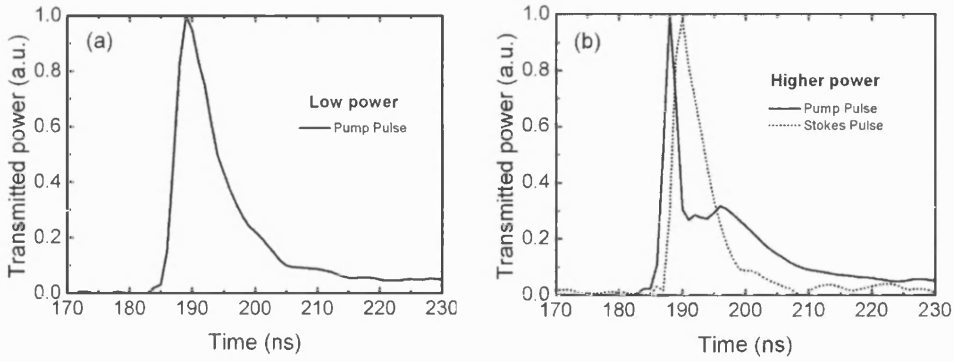

Figure 5.11: Temporal profiles of the pump (solid line) and Stokes (dotted line) pulses at (a) low and (b) high gain. The intensity peaks of the pulses are normalised to the peak of the pump pulse. At higher input powers when the Stokes pulse grows significantly, depletion of the pump pulse in the time domain is observed

5.2.5 Temporal profiles of the Raman pulses

The temporal shape of the Raman pulses was also investigated. Using interference filters of 10 nm spectral width, the different components of the emerging pulses at the fibre output were sent to InGaAs photodetectors. The traces of the pump and first-order Stokes pulses were recorded using a digital oscilloscope at low and high input pump powers (Figure 5.11). In the case shown here, the input pulse width is 7 ns. As the Stokes pulse builds up, depletion of the pump pulse is observed. Just as described theoretically [73], the Stokes pulse rises sharply at the peak of the pump pulse and then drops quickly at the trailing edge, following the shape of the pump pulse.

The delay between the peaks of the two pulses is 2 ns. The theoretically predicted position of the peak of the Stokes pulse with respect to the peak of a Gaussian pump pulse of width τ in a dispersionless medium is given by [73]:

$$t_D = \frac{\tau}{2} \left(\frac{1}{2} \ln G_{ss} \right)^{1/2} , \tag{5.18}$$

where G_{ss} is the steady-state Stokes gain calculated at the peak of the pump pulse. For $G_{ss} = 30$, the theoretical Stokes delay is 3.9 ns, longer than that found experimentally. This is believed to be mainly because of the non-Gaussian shape of the input pump pulse shown in Figure 5.11(a).

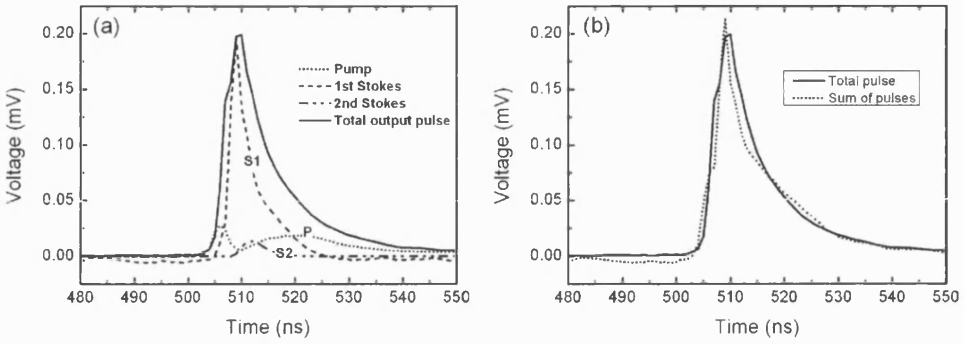

Figure 5.12: (a) Temporal shapes of the pump, first-order and second-order Stokes pulses together with the overall pulse shape at the fibre output. (b) The sum of the different Raman components quite accurately reconstructs the total transmitted pulse

The Stokes pulse width is measured to be about 5 ns for the higher input powers and thus some temporal narrowing is observed, in accordance with both theoretical and experimental observations in transient SRS [73, 76]. In the steady-state temporal broadening is found to occur for the Stokes pulse [69]. This observation corroborates the previously discussed conclusions from SRS threshold data, where transient SRS was found to take place for pulse widths less than 12 ns.

Using the same method as above, the temporal profiles of the pump, first-order and second-order Stokes pulses as well as that of the overall pulse coming out of the fibre were acquired. The voltage reading of the oscilloscope trace was calibrated with respect to the power incident on the photodetector – neutral density filters were used just before the photodetector to avoid saturation. Oscilloscope calibration also accounted for the detection efficiency of InGaAs at different wavelengths and for the absorption introduced by the different interference filters used to isolate the SRS components. These pulse shapes are shown in Figure 5.12. In the same figure the sum of the different Raman temporal traces is compared to the trace of the total transmitted pulse. The latter is quite accurately reconstructed by the sum of the constituent pulses.

Back-reflected pulses

The pulses travelling in the backward direction were also collected and analysed (see Figure 5.1). The temporal profiles of the backward travelling pulses are shown in Figure 5.13(a). The two peaks correspond to light back-reflected at the windows of the two gas cells as marked in the inset picture. The time interval between them ($\approx$ 80 ns) was measured to correspond exactly to the difference in propagation distance between the two pulses (twice the length of the 12 m-long fibre). No other backward travelling pulse was detected and no backward SRS was observed.

The different Raman components of the back-reflected pulses were isolated using interference filters. In the same figure it is shown that the pulse back-reflected at the output cell window was strong enough to generate new backward-travelling SRS waves. In the same manner as the forward-travelling pulses, the back-reflected pulse at the pump wavelength is also depleted when exiting the fibre due to the build-up of the Stokes pulse. Spectra of the back-reflected light were acquired. A typical example taken for a pulse width of 10 ns is shown in Figure 5.13(b).

5.2.6 Selective Raman excitation

It has so far been demonstrated how the very high FOM of the HC-PCF affects both the efficiency and the dynamics of the SRS process. The fibre also affects the SRS spectrum via its transmission bandwidth: if the pump wavelength is varied, different SRS bands will suffer different attenuation rates. Selective generation of specific SRS bands can thus be achieved by tuning the pump wavelength. In the experiments described in this section, the pump wavelength is scanned across the transmission bandwidth of the hydrogen-filled HC-PCF; as a consequence, the excitation of a single SRS band of para-hydrogen was observed for the first time.

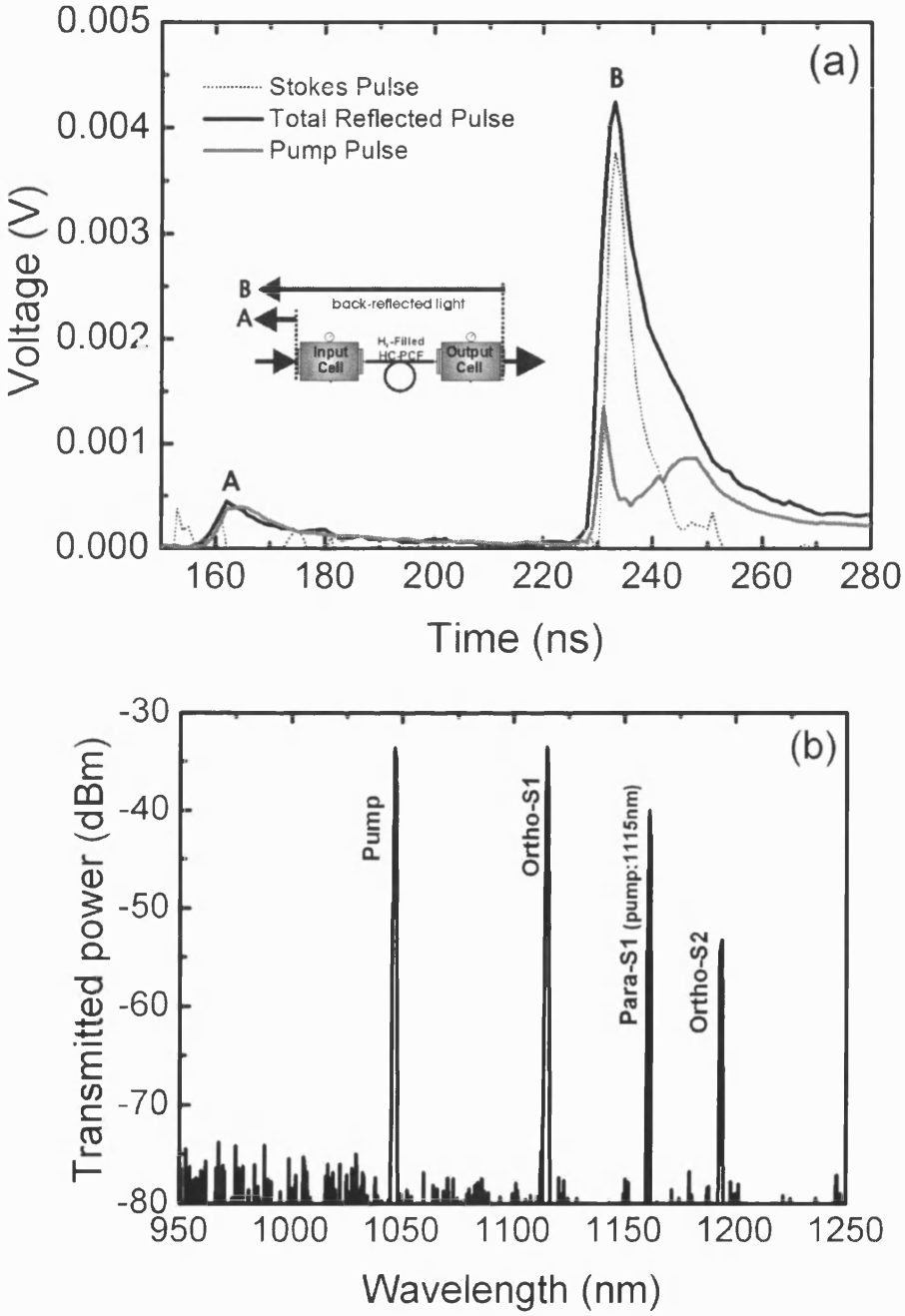

Figure 5.13: (a) Temporal shapes of the backward travelling pulses back-reflected at the gas cell windows as shown in the picture. (b) Typical spectrum of the back-reflected light, consisting of several Raman frequencies

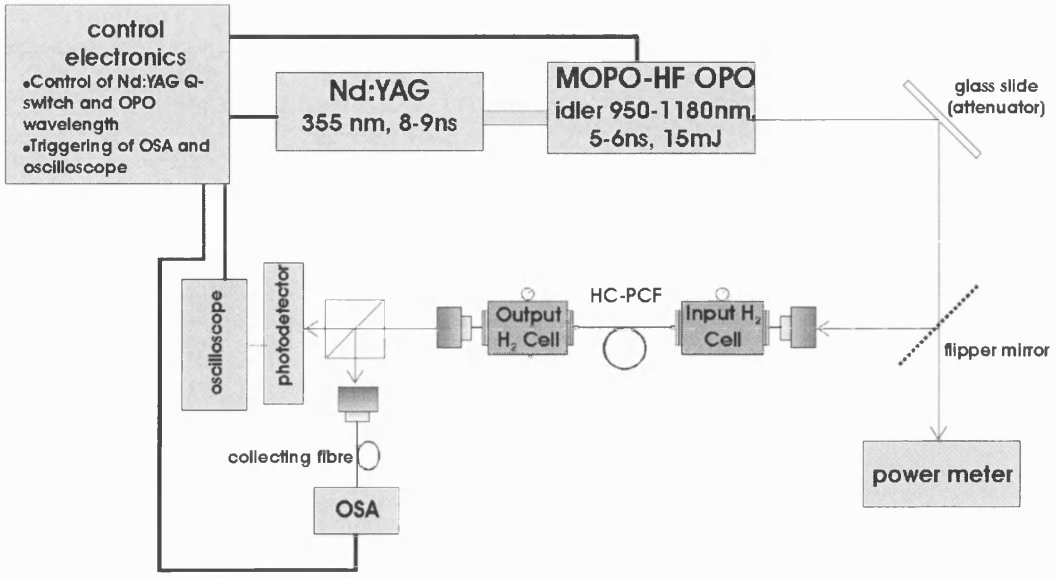

Figure 5.14: Experimental set-up using the OPO as the pump source

Experimental set-up and procedure

The experimental set-up is shown in Figure 5.14. The pump source was the output (idler) beam of the Quanta Ray MOPO-HF (master oscillator/power oscillator high-finesse) optical parametric oscillator (OPO) by Spectra-Physics. In the system used in these experiments, the signal and idler wavelengths can be varied in the ranges 450-690 nm and 735-1800 nm respectively. The wavelength tuning is controlled electronically and is completely automated. The linewidth is sub-0.075 cm^{-1}.

The HC-PCF used was the same as in the previous experiments and its length was 5 m. The hydrogen pressure was 13 bar. The pump wavelength was scanned in the range 950-1180 nm. The output of the OPO (pulse duration 5-6 ns, pulse energy of 15 mJ, peak power 5 MW) was attenuated – typically down to 15 μJ (5 kW peak power) – and then sent to a flipper mirror. The diameter of the output beam was about 5 mm. One path of the beam was passed through a pair of lenses acting as a telescope and then coupled into the HC-PCF with a microscope objective lens (the telescope was used to reduce the beam size and increase the coupling efficiency, which, however, remained low – less than 10%). The other beam was used to monitor the input power. The output of the beam was split into two beams again with a beam-splitter. One beam was sent to a photodetector connected to an oscilloscope and the other beam was sent to an

OSA. The detectors and the OSA were triggered by the control electronics of the MOPO-HF system to the Q-switch of the Nd:YAG laser (the laser pump of the OPO).

Results and discussion

The evolution of the various components with pump wavelength is shown in Figure 5.15(a). The transmitted power at each SRS component is shown normalised to that of the output pump power. In the same figure the attenuation spectrum of the fibre is plotted. Up to a pump wavelength of 1060 nm the waves at both the first- (S1) and the second-order (S2) Stokes frequencies of the $S_{00}(1)$ transition of ortho-hydrogen are present in the output spectrum. For a pump wavelength of 990 nm they both exceed the output pump power. At a pump wavelength of 1060 nm the ortho-S2 wave becomes completely suppressed as the fibre attenuation dominates over the Raman gain. In parallel, the ortho-S1 power decreases as well, but suffers much smaller loss, and is still present in the spectrum. The ortho-S1 wave becomes suppressed when it reaches a wavelength of 1256 nm (pump wavelength 1170 nm).

Interestingly, at 1143 nm pump wavelength the S1 wave of the $S_{00}(0)$ transition of para-hydrogen is detected (with its wavelength at 1190 nm). As the pump wavelength increases the para-S1 wave is amplified and reaches a maximum value (at pump wavelength 1170 nm) just as the ortho-S1 wave is simultaneously vanishing. Around this region of pump wavelength, only the para-S1 Raman component is present. To the author's knowledge, this is the first time that the para-S1 Stokes wave has been uniquely generated in normal hydrogen gas without any Raman components of ortho-hydrogen being present in the SRS spectrum.

This behaviour of the SRS peaks as the pump wavelength is varied is a result of the respective behaviour of the Raman gain for each one of the SRS bands. The exponential gain factor for the Stokes intensity is:

$$G' = g_R \frac{P_P}{A_{eff}} \frac{1 - \exp(-\alpha_P L)}{\alpha_P} - \alpha_S L \,, \tag{5.19}$$

where $\alpha_{P,S}$ the exponential loss coefficient at the pump or Stokes frequency respectively. This is valid for constant pump power, where the Stokes power is

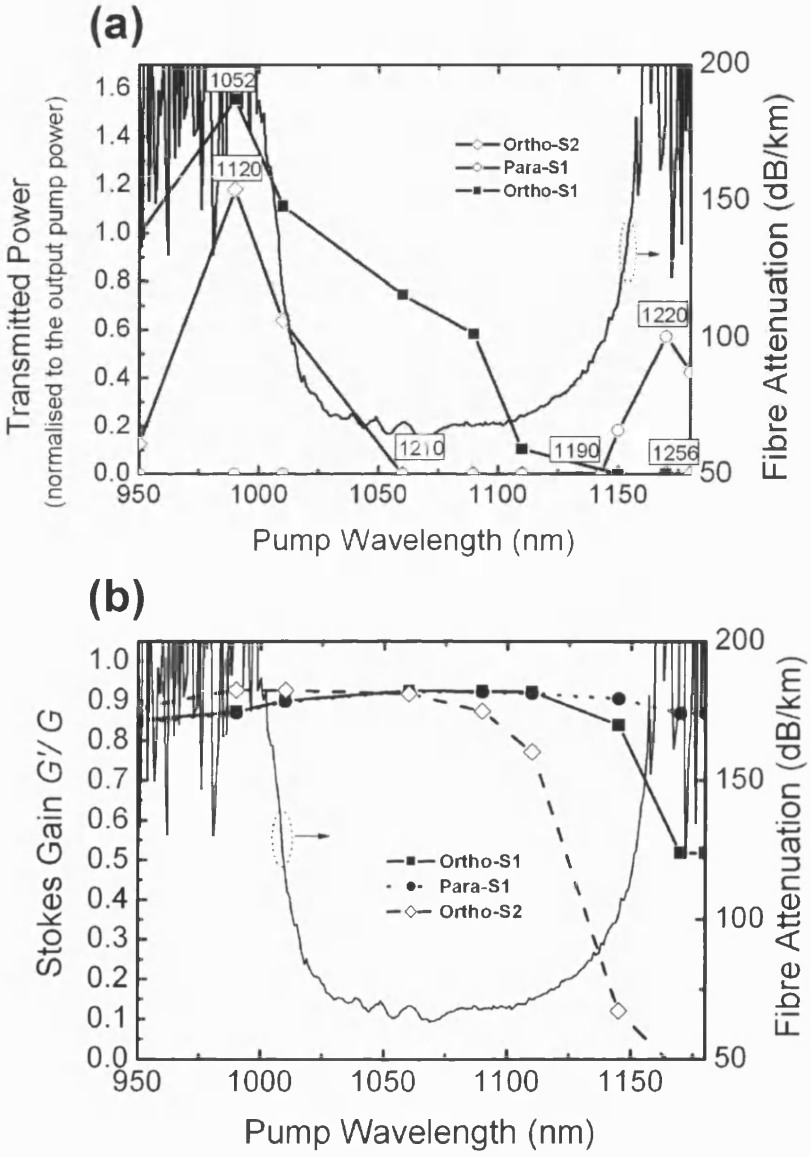

Figure 5.15: (a) Evolution of the measured peak power of the Stokes components at the output of the hydrogen-filed HC-PCF as the pump wavelength is scanned in the region 950-1180 nm. The transmitted power is normalised to the acquired pump power at the output of the fibre. The numbers in boxes show the wavelength that the different SRS components acquire at the particular pump wavelength. The figure also shows the loss spectrum of the fibre (right-hand axis). (b) Raman gain of the Stokes intensities of the two rotational Raman transitions and fibre loss spectrum against pump wavelength. The input pump power is 15 W, while the Raman intensity gain coefficient g_R for the $S_{00}(0)$ transition is taken as one third of that of the $S_{00}(1)$ transition, due to the 1:3 ratio of para- and ortho-hydrogen

of the form $P_S(L) \propto e^{G'}$. This gain is plotted for the observed Stokes frequencies against the pump wavelength in Figure 5.15(b). For the estimation of the gain of the second-order Stokes wave, the field at the first-order Stokes frequency was taken as the (constant) pump source. The plotted gain is normalised to the lossless steady-state gain $G = g_R \frac{P_P}{A_{eff}} L$ for an input pump power of 15 W.

In this last plot 5.15(b), the ortho-S2 gain drops dramatically after a pump wavelength of about 1070 nm, which is exactly where its power drops to zero in Figure 5.15(a). Similarly, the ortho-S1 gain drops significantly after a pump wavelength of 1150 nm, which is again the point at which its signal disappears on Figure 5.15(a). On the other hand, the para-S1 gain remains relatively flat over the range of pump wavelengths. Even so, the para-Stokes signal emerges in Figure 5.15(a) only after the more efficient transitions of ortho-hydrogen are suppressed. However, it must be noted that the Stokes gain estimated here is only approximately valid. An accurate calculation would require the solution of the full set of coupled differential equations of the waves present in the nonlinear medium – pump, ortho-S1, ortho-S2 and para-S1 waves – in which the fibre loss spectrum is also taken into account for each of these waves.

5.3 Summary

By pumping a hydrogen-filled photonic bandgap HC-PCF with long, quasi-CW pulse a comb-like SRS spectrum of nine purely rotational Raman lines was generated. Raman transitions of both ortho- and para-hydrogen were observed. The pump energy threshold for the generation of the 1st-order ortho-Stokes band was about 90 nJ. Such a spectrum can be useful for various applications, such as pulse synthesis and compression, if the different components are fixed in phase [53, 52]. The generation of the SRS spectrum is attributed to the very high FOM achievable with the HC-PCF. This leads to SRS generation over long distances and at low powers. In this operation regime, the dynamics of Stokes amplification were found to exhibit a novel behaviour, where transient SRS takes place at pulses as long as 14 ns. This was both demonstrated experimentally and corroborated theoretically.

Apart from its high FOM, the HC-PCF affects the SRS process via its trans-

mission spectrum. By using a pump beam with tunable wavelength, the usually dominant SRS lines of ortho-hydrogen were suppressed as their wavelength moved into edge of the bandgap; at the same time the Stokes band of ortho-hydrogen was enhanced until it became the only component of the SRS spectrum when the other bands were suppressed.

Chapter 6

Hollow-core photonic crystal fibres for laser manipulation of micrometre-sized particles

The last two chapters described nonlinear light/matter interactions (in particular SRS) in HC-PCFs. This chapter will look at a linear type of interaction inside a HC-PCF: laser-induced particle guidance. Calculations of the optical forces acting on dielectric spheres guided inside a HC-PCF are presented.[1] The calculations are compared with experimental results [9, 10, 48]. It is also shown that, by using a HC-PCF, particle guidance with low power requirements over extremely long distances is achievable.

6.1 Optical forces on a dielectric sphere

Every photon of wavelength λ carries a momentum of magnitude h/λ. When light is scattered by a particle, there is a change in the momentum of the scattered light. The optical or radiation pressure forces exerted on the scattering particle are a result of the momentum transfer from light to the particle. The most general way to derive the optical forces on a particle of arbitrary size is the

[1]The calculations presented in this chapter were carried out by the author and have been published in [10, 77, 48]. The author has also taken some part in the experiments of [9]

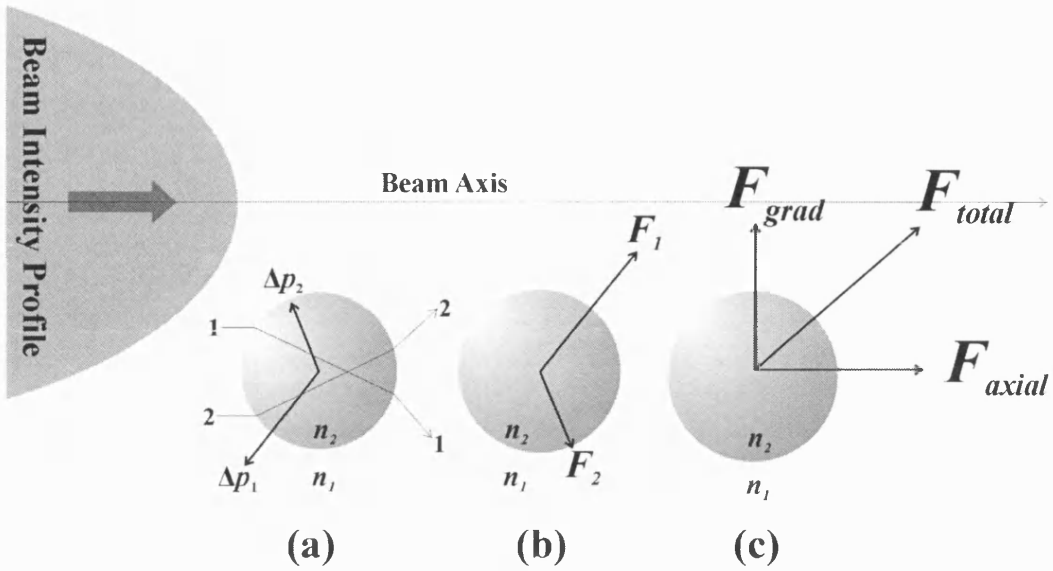

Figure 6.1: Optical forces on a dielectric sphere illuminated by a laser beam in the RO approach. See text for more details

generalised Lorenz-Mie theory (GLMT) [78]. However, due to the complexity of the numerical calculations involved in this approach, it is customary to study the particle/laser interaction for two specific cases: firstly, for particles much larger than the wavelength of the laser light, geometric optics can be used to a good approximation. Secondly, Rayleigh scattering theory can be used for particles much smaller than the wavelength [79].

The laser guidance mechanism as described by the ray optics (RO) approach [34] is now briefly outlined. A beam, with an intensity maximum on its propagation axis (for example, the lowest-order Gaussian laser mode) propagates in a medium of refractive index n and illuminates a dielectric spherical particle of index n_p ($n_p > n$) located off the beam axis (Figure 6.1). The rays 1 (closer to the intensity maximum) and 2 (away from the intensity maximum) hit the particle surface symmetrically about its centre. For a highly transparent particle we can neglect any reflections at the surface of the sphere. As ray 1 is refracted twice on the surface of the sphere, there is a change of the momentum of light Δp_1 in the direction shown in Figure 6.1(a). $-\Delta p_1$ is the amount of momentum transferred by the light ray to the particle. Therefore, a force F_1 is exerted on the sphere in the opposite direction to Δp_1, as in Figure 6.1(b). This force tends to drive the particle towards the beam axis and along the direction of the beam propagation. Similarly, ray 2 will also exert a force on the particle (F_2), but this force will tend to push the particle away from the beam axis. However, due to the intensity

profile of the beam, F_2 will always be smaller than F_1. After summing over all such symmetrical pairs of rays, one finds that the total force F_{total} will tend to push the sphere towards the beam axis and in the direction of propagation of the laser beam, as shown in Figure 6.1(c).

The total radiation force on the sphere F_{total} can be decomposed into a component parallel (axial force) and normal (gradient force) to the beam axis. Based on the RO approach several models have been proposed that take into account the diffraction of a freely propagating Gaussian beam [80] and others that treat the incident rays as streams of photons [81].

When the particle is much smaller than the wavelength, its interaction with the laser beam is treated in terms of Rayleigh scattering. In this wave-optic regime, the axial force depends linearly on the polarisability α of the particle and the laser power, while the gradient force depends on the polarisability and the radial intensity gradient of the beam [79].

6.2 Particle guidance in a HC-PCF

6.2.1 Previous work

Particle guidance in a HC-PCF was first demonstrated in the experimental work of [9, 10]. Before the advent of this type of fibre the only alternative for laser guidance of dielectric particles had been the use of hollow capillaries [36, 82], which of course suffer from the limitations described in Section 2.5 of Chapter 2.

6.2.2 Experimental background

In the experimental work presented in [9, 10], on which the calculations of this chapter are based, dry polystyrene spheres of 5 μm diameter were levitated in air and then guided inside the core of a HC-PCF over a distance of 15 cm. The experimental configuration is shown in Figure 6.2. The laser used was an Ar^+ laser of power $P_0 = 80$ mW and a wavelength of 514.5 nm. The diameter of the

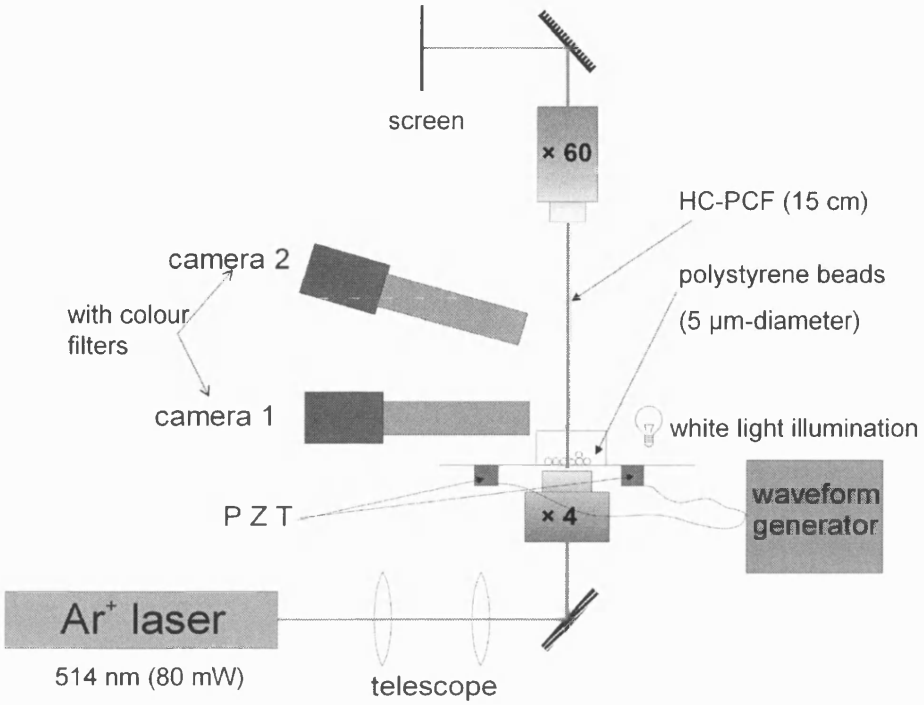

Figure 6.2: The experimental set-up for particle levitation and guidance used in [9]

fibre core was 20 μm and the fibre loss rate was 5 dB/m. The polystyrene spheres were deposited on a glass slide resting on piezoelectric elements vibrating at a resonant frequency of about 80 kHz. This was done to break any van der Waals or electrostatic bonds between the particles and/or between the glass slide and the particles. The fibre was mounted perpendicularly with its input end-face 0.5-1 mm above the glass plate. Thus, the optical scattering force is in the opposite direction to the gravitational force. Cameras were used for the acquisition of real-time video streams of the particle motion.

Figure 6.3(a) shows a sequence of a polystyrene sphere being levitated from the glass slide on which it rested and coupled into the HC-PCF by means of the radiation forces exerted on the particle by the Ar^+ laser beam. The velocity dz/dt of the particle in the vicinity of the input end of the fibre was measured to be 1.2-1.5 cm/s. Figure 6.3(b) shows a sequence of a polystyrene sphere being guided inside the hollow core of the HC-PCF. The particle velocity inside the fibre was measured to be 1 cm/s.

This is the experimental background for particle guidance in a HC-PCF. The

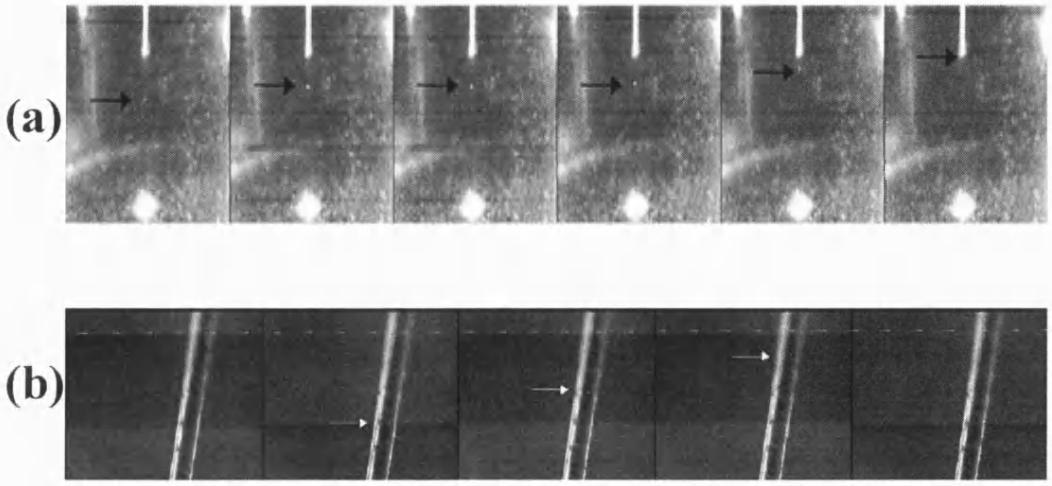

Figure 6.3: (a) Optical levitation of a polystyrene microsphere from the glass plate on which it rested to the entrance of the HC-PCF. (b) Sequence of video frames showing guidance of a microsphere inside the core of the HC-PCF by means of radiation pressure of the laser light guided in the fibre

following will give a calculation of the forces acting on the sphere outside and inside the fibre.

6.2.3 Forces outside the fibre

In this section the budget of forces acting on the sphere outside the fibre during the levitation process is calculated. These forces include the gravitational force, the van der Waals attraction to the glass substrate and hydrodynamic forces, and of course the optical forces induced by the laser beam. In this and all the following sections, z is the laser beam axis (outside the fibre) or the fibre axis (inside the fibre). r is the transverse distance from the beam axis. The point $(r, z) = (0, 0)$ is the centre of the laser beam waist located at the fibre entrance.

In the perpendicular configuration of Figure 6.2, the gravitational force F_g is in the opposite direction to the optical scattering force that causes the particle to levitate. This force is:

$$F_g = \frac{4}{3}\pi a^3 \rho_p g \cong 0.22 \text{ pN} , \tag{6.1}$$

where $a = 2.5$ μm is the radius and $\rho_p = 1.06$ g/cm^3 the density of the polystyrene sphere. As will shortly be shown, this force is too weak compared with the optical force ($\sim$ 10 pN) to have any effect on the levitation process. It can potentially

be important inside the HC-PCF, when the fibre loss causes the optical force to decrease with length.

When dielectric particles are to be levitated in air, the attractive forces between the particles and the substrate have to be overcome. These forces can be several orders of magnitude higher than the radiation forces. In the present experiment, the dominant force is the surface tension on the polystyrene because of its contact with the glass slide. While the optical forces are in the order of $10^{-12} - 10^{-11}$ N, surface tension can be up to 10^{-4} N [83].

Furthermore, the van der Waals force between the particle and the substrate is given by [83]:

$$F_{vdW} = \frac{A_{132}\, a}{6\, x_0^2} \,, \tag{6.2}$$

with A_{132} the Hamaker constant between materials 1 and 2 surrounded by material 3 ($A_{132} \sim 10^{-20} - 10^{-19}$) and x_0 the distance between the sphere and the plate (typically a few Å on contact). This gives an order of magnitude $F_{vdW} \sim 10^{-7}$ N. A similar attractive force acts between two polystyrene spheres. For the size of spheres used in the experiment the electrostatic forces are negligible and become significant only above a critical sphere radius $a_{cr} \approx 0.5$ mm. It is noteworthy that, in water, the surface tension disappears, while the Hamaker constant drops about one order of magnitude.

Therefore, when working in air the particle substrate must be vibrated by PZT elements operating on resonance, where the vibration is highly nonlinear and large accelerations can be achieved. This will give the particles the necessary thermal energy to overcome all the above mentioned attractive forces opposing the induced radiation pressure.

In order to estimate the drag, the type of flow must be established. This is done by calculating the Reynolds number *Re*. Outside the fibre, as the sphere is being levitated, the Reynolds number is given by [84]:

$$Re = \frac{Va\rho}{\eta} = \frac{Va}{v} \,, \tag{6.3}$$

where $V = \mathrm{d}z/\mathrm{d}t$ is the particle velocity and ρ the density of the surrounding fluid. η is the viscosity of the surrounding fluid and $v = \eta/\rho$ the kinematic viscosity ($v = 15 \times 10^{-6}$ m^2/s for air at 20°C). For $a = 2.5$ μm, $\rho = 0.0013$ g/cm^3

and $V \sim 1$ cm/s, one finds $Re \sim 0.0001$. for such a low Reynolds number the flow is laminar [84] and the drag F_D is given by Stokes law:

$$F_D = 6\pi\eta a V \approx 8.5 \text{ pN} . \tag{6.4}$$

The radiation forces exerted on the polystyrene spheres outside the HC-PCF during the levitation process were computed using two different models based on the RO approach. The first model, which only calculates the axial force for particles on the beam axis, is the one found in [80]. In this model the basic RO approach [85] is extended to include the diffraction of the propagating Gaussian beam.

By numerically solving the force Equation C.2 of Appendix C [80], the plot shown in Figure 6.4 was obtained for the present experimental conditions ($w_0 = 10\mu$m and 80 mW power). The plot shows the axial force, F_z versus axial distance z from the beam waist. z is negative when the sphere is located in the convergent part of the focused beam, and positive when the sphere is in the divergent part of the beam. The illuminated particles were taken to be polystyrene spheres (density of spheres $\rho_p = 1.10$ g·cm^{-3}, refractive index $n_p = 1.55$ at 514.5 nm) with a diameter of $2a = 5$ μm in air ($\rho = 0.0013$ g·cm^{-3}, $n = 1.00$), located on the beam axis, while the wavelength is $\lambda = 514.5$ nm.

In [9] the force on the particle was measured using video frames (in the same way as with the measurement of the particle velocity):

$$F_{z,measured} = \frac{4}{3}\pi a^3 \rho_p \frac{\mathrm{d}^2 z}{\mathrm{d}t^2} , \tag{6.5}$$

In Figure 6.4 the experimental data from [9] of the measured force on the polystyrene sphere are compared with the theoretical prediction. The discrepancy between theory and experiment is due to the fact that the measured force is the total force acting on the particle:

$$F_{z,measured} = F_{optical} - F_g - 6\pi\eta a \frac{\mathrm{d}z}{\mathrm{d}t} , \tag{6.6}$$

that is, including the contribution of the gravitational force (~0.22 pN) and the drag.

Table 6.1 summarises the force budget acting on the sphere in the axial direction

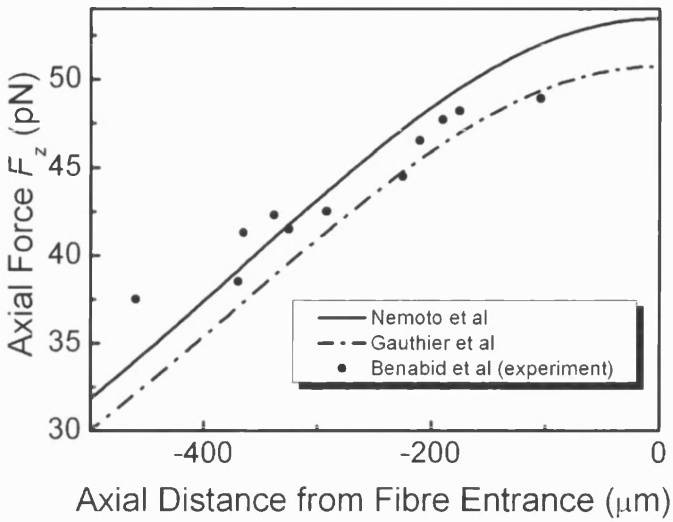

Figure 6.4: Calculated optical force acting on the polystyrene sphere in the axial direction using the model of [80] (solid curve, Equation C.2) and the model of [81] (dot-dashed curve, Equation C.12). The solid circles are the experimental points of [9]

Type of Force	**Force Magnitude (N)**
Gravitational Force	2.2×10^{-13}
Stokes Drag	8.5×10^{-12} (for 1 cm/s particle velocity)
Surface Tension	10^{-4} (on contact with glass substrate in air)
van der Waals	10^{-7} (on contact with glass substrate in air)
Optical Force	$(3-5) \times 10^{-11}$ (for 80 mW laser power)

Table 6.1: Table giving the budget of forces acting on the sphere outside the fibre during the levitation process

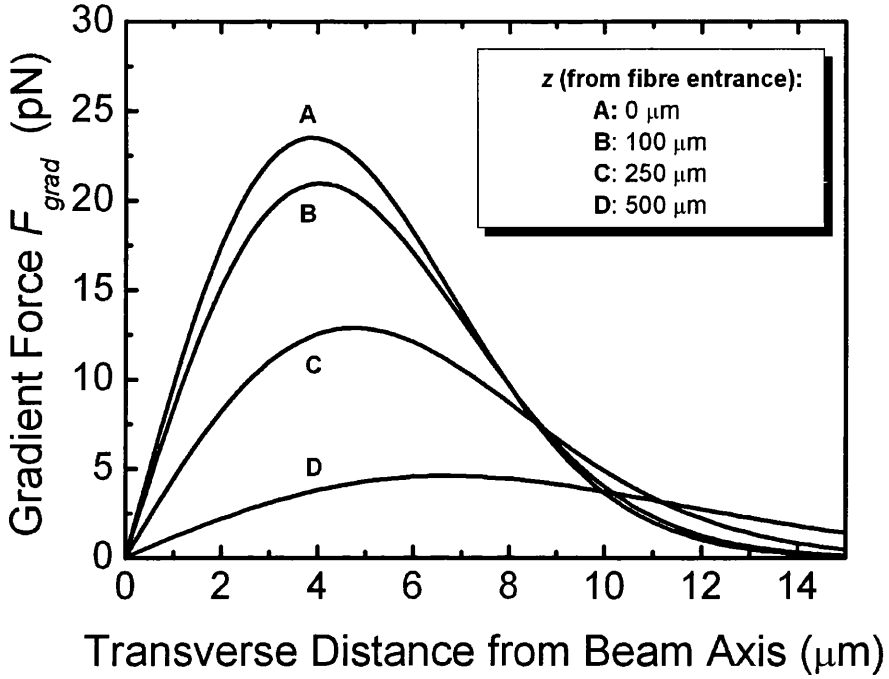

Figure 6.5: Calculated gradient force acting on the sphere outside the fibre for different distances from the fibre entrance, where the beam waist is located. The model used was that of [81] (Equation C.19)

outside the fibre. For a moderate laser power of only 80 mW, the only competitors to the optical force is the surface tension and van der Waals attraction between the particle and the glass substrate. Levitation in air is therefore possible by means of the laser-induced optical force, once of course the van der Waals force is broken by vibrating the substrate as already described. The minimum laser power required to overcome all the non-optical forces (apart from the surface tension and van der Waals force) is 13.5 mW for the present experimental conditions (5-μm-diameter polystyrene spheres in air).

For the transverse force outside the fibre a different model was used (the previous model only gives the axial force): it is called the enhanced RO model and was introduced by Gauthier and Wallace [81]. Even though it is still a RO model, it treats the light rays as streams of photons crossing a dielectric sphere (see Appendix C).

The gradient force (Equation C.19 in Appendix C [81]) is plotted in Figure 6.5 against the transverse offset r for different axial (z) positions of the particle along

the beam axis. The transverse offset is the distance between the centre of the sphere and the beam axis. The beam waist radius is 10 μm. In all cases the transverse force is a restoring one that traps the particle in the centre of the beam. Clearly, the strongest restoring force occurs when the particle is located at the beam focus, since the transverse intensity gradient of the beam is then at its maximum. The resolution of the video frames was not high enough to allow the measurement of the transverse position of the particle and of the gradient force acting on it.

6.2.4 Forces inside the fibre

It has been noted that a decrease in the velocity of the sphere was observed when it entered the fibre. This is the result of two factors: firstly, a drop in the laser power inside the fibre due to coupling losses (the coupling efficiency was about 60-70%). Secondly, an increase in the drag on the particle inside the fibre core. This results from the proximity of the particle to the inner surface of the fibre core (the so-called wall effect [84]).

Inside the fibre, where the particle is contained in the cylindrical core, the flow is described by the relative particle Reynolds number [84]:

$$Re_p = \frac{2a\ |V_0\,(1 - b^2/R_0^2) - V)|}{v}\ , \tag{6.7}$$

where V_0 is the fluid velocity, R_0 the fibre core radius and b the distance between the fibre axis and the centre of the sphere. For motion through a stationary fluid ($V_0 = 0$), the last equation reduces to $Re_p = 2aV/v = 0.00034 \cdot V$. This means that the flow is still laminar inside the fibre, but now the Stokes drag becomes:

$$F_D = 6K\pi\eta a\,\frac{\mathrm{d}z}{\mathrm{d}t}\ , \tag{6.8}$$

where K is a correction factor that accounts for the effect of the container walls. For a sphere moving axially inside a cylindrical container this factor is given by the empirical formula [84]:

$$K = \left[1 - 2.1044\frac{a}{R_0} + 2.0877\left(\frac{a}{R_0}\right)^3 - 6.9481\left(\frac{a}{R_0}\right)^5 - \ldots\right]^{-1}\ . \tag{6.9}$$

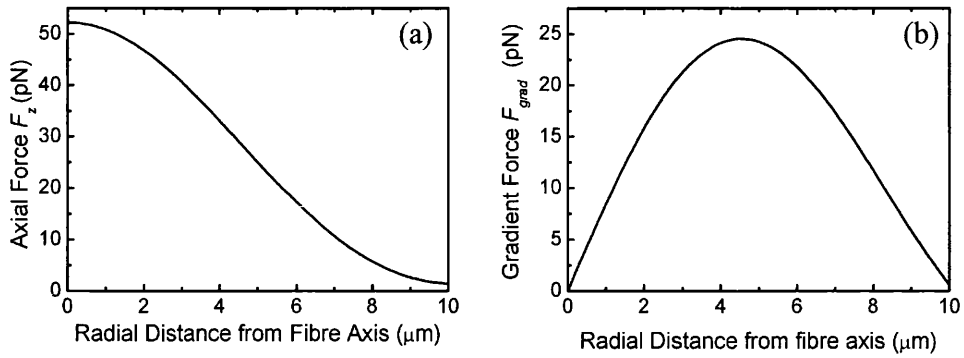

Figure 6.6: Radial variation of the calculated axial (a) and gradient (b) radiation force acting on the polystyrene sphere inside the HC-PCF. The model used was that of [81] but modified for an undiffracted beam with a zero-order Bessel intensity distribution

Substituting $a = 2.5$ μm and $R_0 = 10$ μm gives $K = 2$, and so the Stokes's drag inside the fibre is twice as much as outside the fibre.

The models used so far for calculating the optical forces are only applicable for levitation outside the fibre. Inside the HC-PCF the lowest-loss mode has a Bessel intensity distribution (see Section 2.2) and there is no diffraction of the illuminating beam. In order to model the radiation forces on the polystyrene sphere inside the fibre, the equations of [81] were modified (see also Section C.2 in Appendix C). In particular, the intensity distribution was changed from that of the lowest-order Gaussian mode to:

$$I(r,z) \approx \frac{P_0}{\pi R_0^2} J_0^2\left(2.4\frac{r}{R_0}\right) \exp(-\alpha_L z) \ , \tag{6.10}$$

with J_0 the zero-order Bessel function and α_L the exponential loss coefficient of the HC-PCF at the operating wavelength. This approach is different from the one in [9] where, as an approximation, the equations relating to a Rayleigh particle were used. Under the present experimental conditions (a sphere radius of 5 μm in a HC-PCF with $R_0 = 10$ μm), the axial and gradient forces are plotted against transverse distance from the fibre axis at the fibre entrance in Figure 6.6. Further along the fibre, the effect of the fibre loss rate will reduce the magnitude of the forces. Moreover, the presence of the dielectric sphere itself will possibly have an effect on the propagating mode, acting as a local disturbance [86]. Finally, it can be noted that the results of Figure 6.6 are in very good agreement with those found in [9], even though equations for Rayleigh spheres were used in the latter.

Type of Force	Force Magnitude (N)
Gravitational Force	2.2×10^{-13}
Stokes Drag	1.7×10^{-11} (for 1 cm/s particle velocity)
Optical Scattering Force	5×10^{-11} (at the fibre entrance for 80 mW laser power)

Table 6.2: Table giving the budget of forces acting on the sphere in the vertical (axial) direction inside the fibre

Table 6.2 summarises the budget of forces acting on the particle inside the fibre.

Figure 6.7(a) shows the effect of the size of the HC-PCF core on the magnitude of the restoring gradient force. For a core diameter of 6 μm the force can be an order of magnitude higher than in the present experiment.

The maximum guidance length achievable inside a HC-PCF is found by equating the optical force with the gravitational force, F_g, and is given by:

$$L_{max} = \frac{1}{\alpha} \ln\left(\frac{F_0}{F_g}\right) , \tag{6.11}$$

with α the exponential decay rate and F_0 the peak of the transverse force. In a vertical configuration, like the one employed in the present experiments, with a fibre of a moderate attenuation rate of 1 dB/km, the maximum levitation height attainable is 2 m. In a horizontal configuration, inside a contemporary HC-PCF with an attenuation rate of $\sim$ 1 dB/km, the guidance length is found to be (using the results of Figure 6.6(b) with F_0 = 25 pN) up to 8 km – about 6 orders of magnitude longer than the guidance length achieved with a focused beam, given that the particle remains transversely stable. These results hold for the present experimental conditions (5-μm-diameter polystyrene spheres in air and 80 mW laser power at 514.5 nm).

Furthermore, the HC-PCF offers the possibility of guiding particles around bends in the fibre: the centrifugal force mV^2/R is about 2 orders of magnitude lower than the gravitational force and 4 orders of magnitude lower than the radial optical force (estimated for a critical bend radius of 1 cm and particle velocity of the order of cm/s) [9].

The transverse trapping stability inside the fibre is checked by estimating the

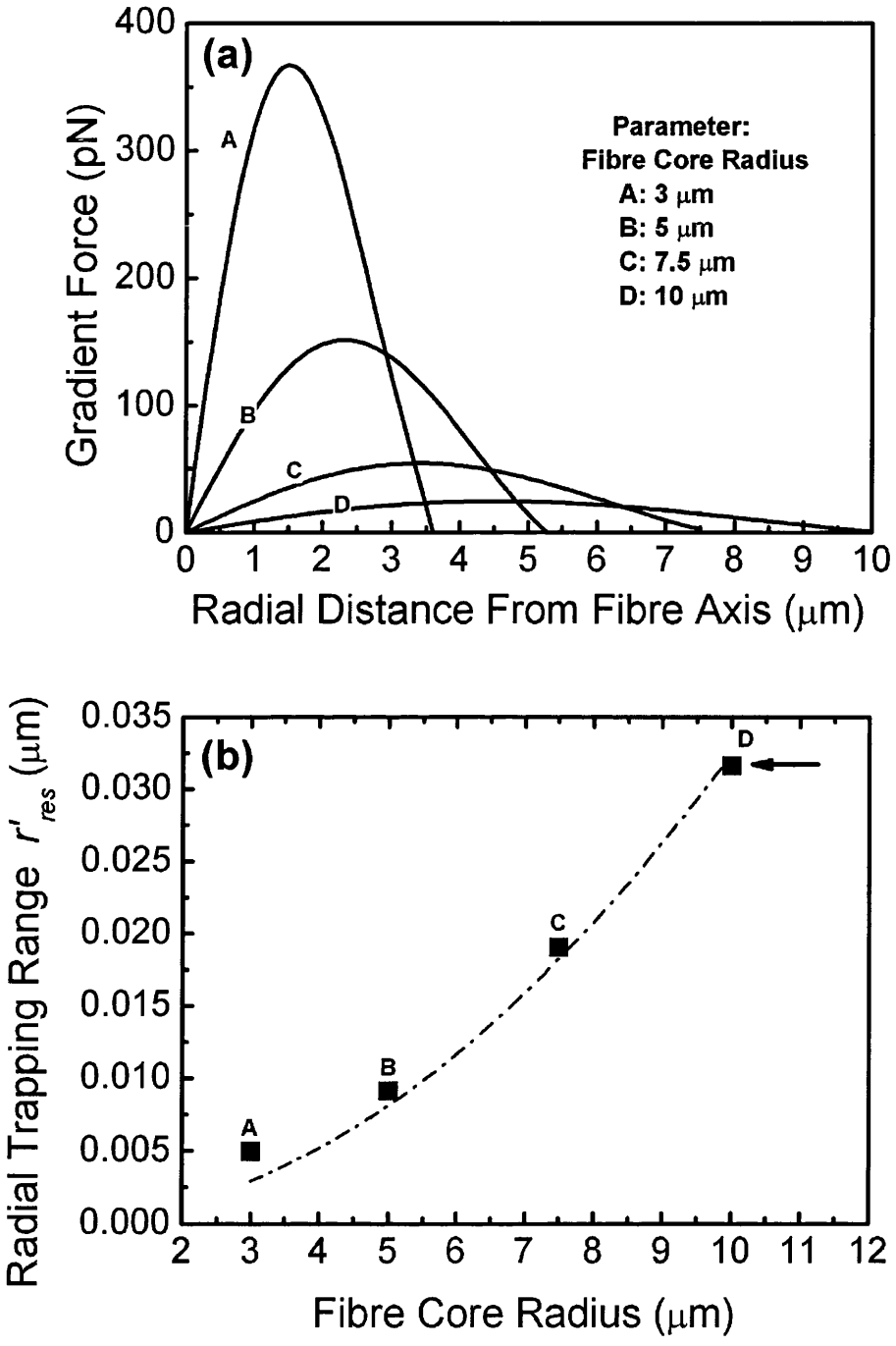

Figure 6.7: (a) The gradient optical force acting on the polystyrene sphere with a radius of 2.5 μm inside HC-PCFs with different core radii. (b) Restoring range of the radial force versus fibre core radius (points). The arrow marks the operation point in the experiments. The line shows a quadratic fit to the data (this type of dependence on core size was predicted in [9])

radial restoring range of the gradient force, within which the optical force overcomes the thermal motion of the sphere. It is assumed that for small (≤ 2 μm) transverse displacements from the beam axis (where the gradient force is almost linear with r) the potential energy of the restoring gradient force is that of an harmonic oscillator. The numerical data calculated above (Figure 6.6(b)) are fitted to that of a spring force, $\vec{F}_r = -\kappa \cdot r$, where κ is the spring constant. The spring constant thus derived was found to be:

$$\kappa = 8 \times 10^{-6} \text{ N/m} . \tag{6.12}$$

The potential energy of the oscillator is given by:

$$W_{opt} = \frac{1}{2}\kappa r^2 . \tag{6.13}$$

The thermal energy on the other hand, is:

$$W_{th} = k_B T , \tag{6.14}$$

where $k_B = 1.3807 \times 10^{-23}$ J/K is Boltzmann's constant and T, the ambient temperature. From this, one gets $W_{th} \cong 4 \times 10^{-21}$ J. Equating the two energies gives the restoring range of the radial force, r_{res}, from the beam axis:

$$r_{res} \cong 0.032 \ \mu\text{m} . \tag{6.15}$$

This is the restoring range around the intensity maximum in the present experimental conditions, where the laser power is 80 mW. By equating the restoring range with the fibre radius (5 μm) one finds that the corresponding spring constant is 3×10^{-9} N/m. This, in turn, corresponds to a laser power of only 0.3 mW, which demonstrates the low power requirements for particle guidance inside a HC-PCF.

Even though the experimental restoring range (Equation 6.15) is enough to prevent the particle from hitting the core walls, it can be further improved by using fibres with smaller cores. Using the method just described, the restoring range was calculated for different core radii. The results are shown in Figure 6.7(b).

6.3 Summary and conclusions

The optical forces on a dielectric sphere being levitated in air and guided inside a HC-PCF by means of radiation pressure forces were calculated. Apart from the laser-induced forces, the gravitational, van der Waals and Stokes drag forces were also estimated. The models used were based on ray optics, a valid assumption for spheres with 5 μm diameter illuminated by a laser beam of wavelength 514.5 nm. The agreement with experimental data [9] was very good. It was also found that, inside a state-of-the-art HC-PCF, the minimum laser power required to transversely trap and guide a polystyrene sphere like the one used in the experiments is only 0.3 mW, while the maximum guidance length in a horizontal configuration for a laser power of 80 mW can be up to several kilometres – 6 orders of magnitude longer than the length attainable with a focused beam. These findings demonstrate that very efficient particle manipulation can be achieved inside a HC-PCF.

Chapter 7

Summary and future work

7.1 Summary

This thesis focused on the investigation of super-enhanced laser/matter interactions inside hollow-core photonic crystal fibres (HC-PCFs). After exploring the effect that any changes in the refractive index contrast might have on the transmission properties of the fibre, efficient vibrational and rotational SRS generation in a HC-PCF was demonstrated. Finally, the efficiency of using a HC-PCF for laser-induced particle guidance was also investigated.

Refractive index scaling and bandgap-guidance in liquid

The first experimental observation of refractive index scaling laws [41] in photonic bandgap fibres was demonstrated [39] in Chapter 3. Such scaling laws are of great usefulness for applications that require the filling of HC-PCFs with different materials, especially if this brings about a considerable change in the refractive index contrast of the fibre. An experimental demonstration of these laws was carried out by replacing the air in HC-PCFs with heavy water, thus lowering the refractive index contrast of the fibre structure. White light and supercontinuum transmission spectra were taken before and after filling the fibres. The transmission bands of the water-filled HC-PCFs were shifted in frequency by a

factor that was found to agree very well with the scalar-wave index-scaling laws. Finally, it is noted that apart from the demonstration of index-scaling, these experiments showed photonic bandgap-guidance in liquid. This can potentially open up possibilities for new fibre devices, as will be mentioned later.

Stimulated Raman scattering in hydrogen-filled HC-PCF

The first experiments ever carried out on gas-based nonlinear optics in HC-PCF [11, 48] were presented in Chapter 4: a HC-PCF that guides light by means of a low density-of-states (the Kagomé fibre) was filled with H_2 gas and pumped by a low-energy Q-switched Nd:YAG laser. Stokes and Anti-Stokes bands of vibrational stimulated Raman scattering (SRS) were generated with a record low energy threshold for Stokes generation of only 800 nJ. The parametric generation and amplification of the Anti-Stokes band was facilitated by the tight phase matching conditions inside the fibre core. Measurements of the transmitted energy point towards the existence of a nonlinear loss mechanism that may be associated with self-focusing.

In another series of experiments (Chapter 5), a bandgap-guiding HC-PCF was again filled with H_2 gas for the study of rotational SRS. This time, the fibre had a much narrower transmission spectrum than the previous fibre, so that only rotational SRS bands would be transmitted. The resultant SRS spectrum consisted of a spectral comb of nine purely rotational Raman lines with a strong presence of the usually suppressed lines of para-hydrogen. The energy threshold for the generation of the 1st-order Stokes band was only 90 nJ. The very long interaction length and the low input power establish a new dynamic regime for the SRS process: transient SRS was observed at pulse widths as long as 14 ns, that is, 2 orders of magnitude higher than the Raman dephasing time. This was also corroborated theoretically. Effects such as the fibre GVD and birefringence were estimated to have only a small effect on the SRS gain. The transmission window can also allow the selective excitation of certain SRS bands and the suppression of others: by tuning the input pump wavelength closer to the bandgap edge of the fibre, the SRS bands of ortho-hydrogen were suppressed in favour of the Stokes band of para-hydrogen. Eventually, and for the first time in normal hydrogen, the para-hydrogen Stokes component became the only component present in the SRS spectrum.

Optical forces in laser guidance of particles using a HC-PCF

Linear light/matter interactions, such as laser-induced particle manipulation, are also enhanced inside a HC-PCF. In the work presented in Chapter 6, the optical forces on a dielectric particle being guided in HC-PCF were calculated using two different ray-optical models. The agreement with experimental data was very good. The force calculations also demonstrated the high efficiency of particle guidance in a HC-PCF: the maximum guidance length that can be achieved was found to be up to several kilometres – 6 orders of magnitude longer than the length attainable with other conventional techniques.

7.2 Future work

Refractive index scaling and bandgap-guidance in liquid

Following the index-scaling experiments described in this work, further research has already taken place in low-index-contrast PCFs, made of glasses with an index contrast of only 1% [87]. Other new research possibilities are also open: first of all, there can be further experimental study of the vector and scalar effects in bandgap structures, for example by continuously varying the index contrast of the PCF and studying its transmission properties. Furthermore, by choosing the right fibre structure and low-index medium, UV transmission may be achieved; in the case of silica and air this would require the fabrication of an impossibly small structure, but UV transmission becomes practical in the ultra-low-contrast case. Finally, by using a suitable liquid crystal to fill the air-holes of a HC-PCF and applying an external field, tunable bandgap fibre devices may be fabricated.

Gas-based nonlinear optics in hydrogen-filled HC-PCF

The unprecedented enhancement of the nonlinear interaction between light and dilute materials, such as gases, in a HC-PCF has opened up novel regimes for gas-based nonlinear optics. In SRS, further improvement can be achieved by using the lowest-loss HC-PCFs available (with a attenuation rate of 1.7 dB/km)

and narrower linewidth lasers. Further research can also be carried out on the effect of gas pressure, since the Raman gain coefficient depends on pressure as $g_R(p) \propto p/\Gamma(p)$ [71]. The pressure effect can be further enhanced by the ability of the HC-PCF to be loaded at high pressures (at least up to 50 bar). Also, setting-up a linear pressure gradient along the fibre may lead to pulse chirping [88].

Especially in rotational SRS, Raman-based mode-locked gas lasers [53] might be developed by generating SRS spectra of multiple lines at a very low energy threshold. All-fibre devices consisting of gas-filled HC-PCFs with their end-faces sealed and spliced to conventional fibres have already been demonstrated experimentally [89].

The use of gas-filled HC-PCFs can also lead to significant progress in virtually all types of gas-based nonlinear optics. For example, it can be used for the generation of high-order harmonics in the spectral range of UV and soft X-rays, by pumping inert gases with femtosecond pulses [55].

PCF for laser-induced manipulation of particles and atoms

The use of a HC-PCF can be extended to all the applications of laser-induced manipulation of particles, including those in microengineering and biology. Further studies can be carried out on the effect of the guided particle on the propagating mode [86]. Finally, HC-PCFs can also be used for guiding neutral atoms and can potentially be very useful in the study of cold atoms [38] and Bose-Einstein condensates (BEC [90, 91, 92]).

Appendix A

Equations for stimulated Raman scattering

A.1 Classical description of SRS

Nonlinear polarisation

When an electromagnetic field propagates inside a medium, the electric polarisation vector $\mathbf{P}$ of the latter can be written as a sum of its linear, $\mathbf{P}^L$, and nonlinear, $\mathbf{P}^{NL}$, polarisation:

$$\begin{aligned} \mathbf{P} &= \mathbf{P}^L + \mathbf{P}^{NL} \\ &= \epsilon_0[\chi^{(1)}(\omega)\cdot\mathbf{E} + \chi^{(2)}(\omega) : \mathbf{EE} + \chi^{(3)}(\omega) \vdots \mathbf{EEE} + \ldots] , \end{aligned} \tag{A.1}$$

with ϵ_0 the dielectric constant, $\chi^{(n)}(\omega)$ the nth-order susceptibility tensor of the medium and $\mathbf{E}$ the electric field vector of the electromagnetic radiation. The term $\epsilon_0\chi^{(1)}(\omega)\cdot\mathbf{E}$ accounts for the linear response of the medium, while the higher order terms describe its nonlinear response to the electric field.

In the current notation, the real-valued electric field $\mathbf{E}_j(\mathbf{r},t)$ is written as:

$$\mathbf{E}_j(\mathbf{r},t) = \frac{1}{2}\left\{\mathbf{A}_j(\mathbf{r})\exp[i(\mathbf{k}_j\mathbf{r}-\omega_j t)] + \mathbf{A}_j^*(\mathbf{r})\exp[-i(\mathbf{k}_j\mathbf{r}-\omega_j t)]\right\}$$

$$= \text{Re}\left\{\mathbf{A}_j(\mathbf{r})\exp[i(\mathbf{k}_j\mathbf{r}-\omega_j t)]\right\} \ , \tag{A.2}$$

with $\mathbf{A}_j(\mathbf{r})$ the complex field amplitude. Also, the nth order susceptibility tensor acting on the product of the fields $\mathbf{E}(\omega_1)\mathbf{E}(\omega_2)\cdots\mathbf{E}(\omega_n)$, with $\omega_1+\omega_2+\cdots+\omega_n = \omega$, is written as $\chi^{(n)}(\omega;\omega_1,\omega_2,\ldots,\omega_n)$. For negative frequencies, the complex conjugate of the electric field amplitude is taken [93].

The polarisation at the Stokes frequency $\mathbf{P}_S$ of a volume of hydrogen gas when the electric field frequencies present are the pump ω_P and Stokes ω_S frequencies will now be examined. Since H_2 is a centro-symmetric molecule, the second-order susceptibility vanishes [58]. Nonlinear terms higher than third-order can also be neglected. The third-order susceptibility at the Stokes frequency is a sum of a non-resonant term $\chi^{(3)}_{NR}(\omega_S;\omega_S,-\omega_S,\omega_S)$ and a resonant term $\chi^{(3)}_R(\omega_S;\omega_P,-\omega_P,\omega_S)$ (the latter accounts for Raman scattering).

The polarisation vector of the medium becomes a sum of a linear term $\mathbf{P}^L_S$, a non-resonant nolinear term $\mathbf{P}^{NL}_{S,NR}$ and a resonant nonlinear term $\mathbf{P}^{NL}_{S,R}$:

$$\begin{aligned}\mathbf{P}_S(\mathbf{r},t) \ = \ \text{Re}\{\epsilon_0 [\underbrace{\chi^{(1)}(\omega_S;\omega_S)\cdot\mathbf{A}_S}_{\mathbf{P}^L_S} + \underbrace{\chi^{(3)}_{NR}(\omega_S;\omega_S,-\omega_S,\omega_S)\vdots\mathbf{A}_S\mathbf{A}^*_S\mathbf{A}_S}_{\mathbf{P}^{NL}_{S,NR}} + \\ + \underbrace{\chi^{(3)}_R(\omega_S;\omega_P,-\omega_P,\omega_S)\vdots\mathbf{A}_P\mathbf{A}^*_P\mathbf{A}_S}_{\mathbf{P}^{NL}_{S,R}}]\exp[i(\mathbf{k}_S\mathbf{r}-\omega_S t)]\} \ ,\end{aligned} \tag{A.3}$$

where $\mathbf{A}_P$ and $\mathbf{A}_S$ are the (complex) amplitudes at the pump and Stokes frequencies respectively.

Coupled wave equations

The wave equation for the electric field as it propagates in the nonlinear medium can be found by starting from Maxwell's equations for the propagation of an electromagnetic field in a medium without free charges:

$$\nabla\times\mathbf{E}(\mathbf{r},t) \ = \ -\frac{\partial\mathbf{B}(\mathbf{r},t)}{\partial t} \ , \tag{A.4}$$

$$\nabla\times\mathbf{H}(\mathbf{r},t) \ = \ \epsilon_0\frac{\partial\mathbf{E}(\mathbf{r},t)}{\partial t}+\frac{\partial\mathbf{P}(\mathbf{r},t)}{\partial t} \ . \tag{A.5}$$

The magnetic induction $\mathbf{B}$ relates to the magnetic field strength $\mathbf{H}$ via the relationship: $\mathbf{B} = \mu_0\mathbf{H}$, with μ_0 the magnetic permeability of vacuum. The polarisation can be written as a sum of its linear and nonlinear term: $\mathbf{P} = \epsilon_0\chi^{(1)}\mathbf{E}+\mathbf{P}^{NL}$.

By operating on the first equation with $\nabla\times$, the second with $\mu_0\partial/\partial t$ and subtracting, after using the identity $\nabla \times \nabla \times \mathbf{A} = \nabla(\nabla \cdot \mathbf{A}) - \nabla^2\mathbf{A}$, the nonlinear wave equation is obtained:

$$\nabla^2\mathbf{E}(\mathbf{r},t) = \frac{\epsilon(\omega)}{c^2}\frac{\partial^2}{\partial t^2}\mathbf{E}(\mathbf{r},t) + \mu_0\frac{\partial^2}{\partial t^2}\mathbf{P}^{NL}(\mathbf{r},t) \ , \tag{A.6}$$

with $\epsilon(\omega) = 1+\chi^{(1)}(\omega)$ the dielectric tensor and $c = (\epsilon_0\mu_0)^{-1/2}$ the speed of light in vacuum. Each one of the electric field vectors incident and scattered during the SRS process will obey the wave Equation A.6.

Due to its interaction with the electromagnetic field, a diatomic molecule such as H_2 can make a transition to an excited state of molecular motion, like those shown in Figure 4.3 on page 48. The hydrogen nuclei will, thus, be displaced with respect to each other from their initial positions. The wave equation for the normal coordinate of the nuclear displacement $\mathbf{Q}(\mathbf{r},t) = \mathbf{R}(\mathbf{r},t)(2\rho)^{1/2}$, with $\mathbf{R}$ the relative displacement of the nuclear positions and ρ the reduced mass density, will be [49]:

$$\frac{\partial^2}{\partial t^2}\mathbf{Q} + 2\Gamma\frac{\partial}{\partial t}\mathbf{Q} + \omega_R^2\mathbf{Q} + \beta^2\nabla^2\mathbf{Q} = -\frac{\partial}{\partial Q}\mathbf{H}_{int} \ . \tag{A.7}$$

$\mathbf{H}_{int}$ is the interaction Hamiltonian between the electromagnetic wave and the medium. In the above equation of motion of the normal coordinate the second term in the LHS describes the damping of the nuclear oscillation (which has a resonance at the Raman frequency ω_R) while the fourth term is added phenomenologically to describe the spatial propagation of the $\mathbf{Q}$ field. The Raman-interaction Hamiltonian (for a single molecule) is given by [49, 69]:

$$\mathbf{H}_{int} = \mathbf{ME} = \left(\frac{\partial\mathbf{a}}{\partial Q}\right)_{Q=0} \vdots \mathbf{QEE} \ , \tag{A.8}$$

where $\mathbf{M}$ is the dipole moment and $\mathbf{a}$ is the optical polarisability tensor of the molecule. The latter is written as a power series expansion in $\mathbf{Q}$ [69]:

$$\mathbf{a} = \mathbf{a}_0 + \left(\frac{\partial\mathbf{a}}{\partial Q}\right)_{Q=0}\mathbf{Q} + \dots \ . \tag{A.9}$$

The macroscopic electric polarisation of the entire medium (consisting of N molecules) is:

$$\mathbf{P} = N\mathbf{a}\mathbf{E} = \underbrace{N\mathbf{a}_0 \cdot \mathbf{E}}_{\mathbf{P}^L} + \underbrace{N\left(\frac{\partial \mathbf{a}}{\partial Q}\right)_{Q=0} : \mathbf{Q}\mathbf{E}}_{\mathbf{P}^{NL}} . \tag{A.10}$$

Inserting Equations A.8 and A.9 in the wave equation A.7 gives:

$$\frac{\partial^2}{\partial t^2}\mathbf{Q} + 2\Gamma\frac{\partial}{\partial t}\mathbf{Q} + \omega_R^2\mathbf{Q} + \beta^2\nabla^2\mathbf{Q} = -N\left(\frac{\partial \mathbf{a}}{\partial Q}\right)_{Q=0} : \mathbf{E}\mathbf{E} . \tag{A.11}$$

Furthermore, Equation A.10 can be used in the nonlinear wave equation (Equation A.6) for the electric field. For co-propagating electromagnetic fields at frequencies ω_P and ω_S and a sound wave at ω_v (with $\omega_P = \omega_S + \omega_v$) one finally gets:

$$\nabla^2\mathbf{E}_P - \frac{\epsilon(\omega)}{c^2}\frac{\partial^2}{\partial t^2}\mathbf{E}_P = \mu_0\frac{\partial^2}{\partial t^2}N\left(\frac{\partial \mathbf{a}}{\partial Q}\right)_{Q=0} : \mathbf{Q}\mathbf{E}_S , \tag{A.12}$$

$$\nabla^2\mathbf{E}_S - \frac{\epsilon(\omega)}{c^2}\frac{\partial^2}{\partial t^2}\mathbf{E}_S = \mu_0\frac{\partial^2}{\partial t^2}N\left(\frac{\partial \mathbf{a}}{\partial Q}\right)_{Q=0} : \mathbf{Q}^*\mathbf{E}_P , \tag{A.13}$$

$$\frac{\partial^2}{\partial t^2}\mathbf{Q} + 2\Gamma\frac{\partial}{\partial t}\mathbf{Q} + \omega_R^2\mathbf{Q} + \beta^2\nabla^2\mathbf{Q} = -N\left(\frac{\partial \mathbf{a}}{\partial Q}\right)_{Q=0} : \mathbf{E}_P\mathbf{E}_S^* . \tag{A.14}$$

These are the coupled wave equations for the electric and molecular motion fields. They are coupled together via the nonlinear term of the polarisability of the medium. For example, the second coupled equation shows that the interference between the molecular motion field $\mathbf{Q}$ and the electric pump field $\mathbf{E}_P$ drives the electric field $\mathbf{E}_S$ at the Stokes frequency. The interference of the two electric fields, on the other hand, drives the molecular motion, as described by the last coupled equation.

Solutions to these coupled equations are of the form:

$$\mathbf{E}_{P,S}(\mathbf{r},t) = \mathbf{A}_{P,S}\exp[i(\mathbf{k}_{P,S}\mathbf{r} - \omega_{P,S}t)] , \tag{A.15}$$

$$\mathbf{Q}(\mathbf{r},t) = \mathbf{Q}_v\exp[i(\mathbf{k}_v\mathbf{r} - \omega_v t)] , \tag{A.16}$$

for which the frequency and phase matching conditions hold:

$$\omega_P = \omega_S + \omega_v , \tag{A.17}$$

$$\mathbf{k}_P = \mathbf{k}_S + \mathbf{k}_v \ . \tag{A.18}$$

Link between polarisability and Raman susceptibility

In the beginning of this section, the nonlinear polarisation of the medium in the case of Raman scattering was described via the Raman susceptibility tensor $\chi_R^{(3)}$. The latter is rigorously derived quantum mechanically [93]. Here a link will be established between this quantum mechanical quantity and the molecular polarisability of classical physics.

If the expression for $\mathbf{Q}$ (A.16) is inserted into the wave equation A.14, one gets:

$$\mathbf{Q} = -\frac{N\left(\frac{\partial \mathbf{a}}{\partial Q}\right)_{Q=0} : \mathbf{E}_P\mathbf{E}_S^*}{\omega_v^2 - \omega_R^2 + \beta^2 k_v^2 + i2\omega_v\Gamma} = -\frac{N\left(\frac{\partial \mathbf{a}}{\partial Q}\right)_{Q=0} : \mathbf{E}_P\mathbf{E}_S^*}{D^*} \ . \tag{A.19}$$

Substituting this into A.13 gives:

$$\nabla^2\mathbf{E}_S - \frac{\epsilon(\omega)}{c^2}\frac{\partial^2}{\partial t^2}\mathbf{E}_S = \mu_0\frac{\partial^2}{\partial t^2}\,\chi_R^{(3)}(\omega_S;\omega_P,\omega_P,-\omega_S) \vdots \mathbf{E}_P\mathbf{E}_P\mathbf{E}_S^* \ . \tag{A.20}$$

If the non-resonant polarisation term is ignored, one finds [49]:

$$\chi_R^{(3)} = -N^2\frac{\left(\frac{\partial \mathbf{a}}{\partial Q}\right)_{Q=0}\left(\frac{\partial \mathbf{a}}{\partial Q}\right)_{Q=0}}{D^*} \ . \tag{A.21}$$

This last relationship provides a link between the classical picture of molecular polarisability and the quantum picture of the resonant Raman susceptibility.

A.2 Generation of 1st-order Stokes radiation

Here the equation governing the growth of the 1st-order Stokes band will be derived for the steady-state case, that is when the temporal variation of the pump field envelope can be neglected. This will lead to a useful exponential equation for the growth of the field and to the introduction of the Raman intensity gain. These equations are used throughout Chapters 4 and 5.

In order to investigate the growth of the wave generated at the Stokes frequency, the nonlinear wave equation A.6 will be solved for the electric field described by Equation A.15. It is found that:

$$\nabla^2 \mathbf{E}_S = \left[\nabla^2 \mathbf{A}_S + 2i(\mathbf{k}_S \nabla \mathbf{A}_S) - k_S^2 \mathbf{A}_S\right] \exp[i(\mathbf{k}_S \mathbf{r} - \omega_S t)] \ , \quad \text{(A.22)}$$

$$\frac{\partial^2}{\partial t^2}\mathbf{E}_S = \left(\frac{\partial^2}{\partial t^2}\mathbf{A}_S + 2i\omega_S \frac{\partial}{\partial t}\mathbf{A}_S - \omega_S^2 \mathbf{A}_S\right) \exp[i(\mathbf{k}_S \mathbf{r} - \omega_S t)] \ . \quad \text{(A.23)}$$

The slowly-varying envelope approximation is now used:

$$\left|\nabla^2 \mathbf{A}_S\right| \ll |(\mathbf{k}_S \nabla)\mathbf{A}_S| \ . \quad \text{(A.24)}$$

Moreover, in the steady-state, $\partial \mathbf{A}_S / \partial t \rightarrow 0$. Also from the form of Equation A.3, it is found that $\partial^2 \mathbf{P}_S^{NL} / \partial t^2 = -\omega_S^2 \mathbf{P}_S^{NL}$. From these, the nonlinear wave equation becomes:

$$2i(\mathbf{k}_S \nabla)\mathbf{A}_S + i\epsilon''(\omega_S)\frac{\omega_S^2}{c^2}\mathbf{A}_S = -\mu_0 \omega_S^2 \mathbf{P}_S^{NL} \exp[-i(\mathbf{k}_S \mathbf{r} - \omega_S t)] \ . \quad \text{(A.25)}$$

For the derivation of the above, the dielectric tensor is written as $\epsilon = \epsilon' + i\epsilon''$, and use is made of the relations:

$$n(\omega) = \sqrt{\epsilon'(\omega)} \ , \quad \text{(A.26)}$$

$$k(\omega) = \frac{\omega \, n(\omega)}{c} \ . \quad \text{(A.27)}$$

For propagation only in the z-direction, the nonlinear wave equation becomes:

$$\frac{\mathrm{d}}{\mathrm{d}z}\mathbf{A}_S + \alpha \mathbf{A}_S = i\zeta \mathbf{P}_S^{NL} \exp[-i(\mathbf{k}_S \mathbf{r} - \omega_S t)] \ , \quad \text{(A.28)}$$

where:

$$\alpha = \frac{\epsilon''(\omega_S)\, \omega_S^2}{2\, k_S\, c^2} \ , \quad \text{(A.29)}$$

$$\zeta = \frac{\omega_S}{2\epsilon_0\, n(\omega_S)\, c} \ . \quad \text{(A.30)}$$

Inserting the nonlinear terms of Equation A.3 into the A.28 yields:

$$\frac{\mathrm{d}}{\mathrm{d}z}\mathbf{A}_S + \alpha \mathbf{A}_S = i\epsilon_0 \zeta \left(\chi_{NR}^{(3)} |\mathbf{A}_S|^2 \mathbf{A}_S + \chi_R^{(3)} |\mathbf{A}_P|^2 \mathbf{A}_S\right) \ . \quad \text{(A.31)}$$

The solution to this equation is:

$$\begin{aligned}\mathbf{A}_S(z) &= \mathbf{A}_S(0)\exp\left[\left(-\epsilon_0\zeta\,\chi_R''\left|\mathbf{A}_P\right|^2-\alpha\right)z\right]\times \\ &\quad\times\exp\left[i\epsilon_0\zeta\left(\chi_R'\left|\mathbf{A}_P\right|^2+\chi_{NR}^{(3)}\left|\mathbf{A}_S\right|^2\right)z\right]\ ,\end{aligned} \tag{A.32}$$

where the Raman susceptibility is written as $\chi_R^{(3)}=\chi_R'+i\chi_R''$. The non-resonant susceptibility has a real value. Therefore, the terms proportional to $\chi_{NR}^{(3)}$ and χ_R' only modify the refractive index and introduce a nonlinear phase-shift via the optical Kerr effect. The term in α clearly describes the linear attenuation of the propagating Stokes wave. If χ_R'', on the other hand, is negative, then the Stokes amplitude experiences exponential amplification. The Raman amplitude gain is then:

$$G_A=-\epsilon_0\zeta\chi_R''\left|\mathbf{A}_P\right|^2 z\ . \tag{A.33}$$

Writing the square of the pump amplitude in terms of the field intensity, $I_P=\frac{1}{2}\epsilon_0\epsilon(\omega_P)c\left|\mathbf{A}_P\right|^2$ [45], the intensity of the Stokes field builds up as $I_S=\exp G$, with G the Raman intensity gain:

$$G=-\frac{2\omega_S\,\chi_R''}{\epsilon_0 n(\omega_S)\,\epsilon(\omega_P)\,c^2}\ I_P z=g_R\,I_P\,z\ , \tag{A.34}$$

where g_R is the plane-wave Raman intensity gain coefficient, with units m/W.

A.3 Generation of 1st-order Anti-Stokes radiation

In this section the equation for the growth of the 1st-order Anti-Stokes field will be derived, as it is used in Chapter 4.

The generation of radiation at the Anti-Stokes frequency can be described as a four-wave mixing (FWM) process between two pump photons, a Stokes and an Anti-Stokes photon with:

$$\omega_{AS}=\omega_P+\omega_P-\omega_S\ . \tag{A.35}$$

The nonlinear polarisation, $\mathbf{P}_{AS}$, once the non-resonant terms are neglected, will

be:

$$\mathbf{P}_{AS} = \epsilon_0 \chi_R^{(3)}(\omega_{AS}; \omega_P, \omega_P, -\omega_S) \vdots \mathbf{E}_P \mathbf{E}_P \mathbf{E}_S^* . \tag{A.36}$$

The Anti-Stokes wave will obey a nonlinear wave equation like Equation A.31. Inserting the nonlinear polarisation into this wave equation (where the linear loss term is left out), and integrating for constant $\mathbf{A}_P$ and $\mathbf{A}_S$ and for $\mathbf{A}_{AS}(0) = 0$, will give:

$$\mathbf{A}_{AS}(z) = \zeta \epsilon_0 \chi_R(\omega_{AS}) \mathbf{A}_P \mathbf{A}_P \mathbf{A}_S^* \, z \, \frac{\exp(i\Delta k z) - 1}{\Delta k z} . \tag{A.37}$$

Rewriting the above in terms of field intensities yields:

$$I_{AS}(z) = \frac{\omega_{AS}^2 \left|\chi_R(\omega_{AS})\right|^2}{\epsilon_0^2 \, \epsilon^2(\omega_P) \, \epsilon(\omega_S) \, c^4} I_P^2 I_S \, z^2 \, \mathrm{sinc}^2 \left(\frac{\Delta k z}{2} \right) , \tag{A.38}$$

with $\mathrm{sinc}x = (\sin x)/x$ and:

$$\Delta k = k_{AS} - (2k_P - k_S) - \Delta k^{NL} , \tag{A.39}$$

with Δk^{NL} the nonlinear phase mismatch due to nonlinear phase modulation.

Appendix B

Raman gain versus pulse width

This appendix will present the equations of Reference [69], which were used in Chapter 5 for the theoretical calculation of the Raman gain for different pulse widths, as plotted in Figure 5.6 on page 72.

The electric field of the Stokes wave is found to be:

$$E_S \approx E_{S0} + E_{S0} a \int_0^{\tau_0} \exp(-\tau^2)\, I_1(a\tau) \mathrm{d}\tau \ , \tag{B.1}$$

where E_{S0} is the field magnitude of the spontaneous Raman noise and I_1 is the first-order modified Bessel function. Moreover:

$$\begin{aligned} a^2 &= 4 g_R I_P z \\ &= 4\, g_R \frac{P_P}{A_{eff}} L_{eff} \ , \qquad \text{(B.2)} \\ \tau_0^2 &= \Gamma \tau \ . \qquad \text{(B.3)} \end{aligned}$$

Assuming an exponential growth from noise for the Stokes wave, the quantity:

$$\ln\left(\frac{E_S}{E_{S0}}\right) = \ln\left[1 + a \int_0^{\tau_0} \exp(-\tau^2)\, I_1(a\tau) \mathrm{d}\tau\right] \ , \tag{B.4}$$

represents the Raman gain.

In Figure 5.6, the above equation was numerically calculated and plotted against τ for different interaction lengths using the program Mathematica v4.1. The

following values were used in the calculation: $g_R = 3$ cm/GW, $P_P = 10$ W, $A_{eff} = \pi R_0^2$ with $R_0 = 3.5$ μm and $\Gamma = (2\pi T_2)^{-1}$ with $T_2 = 200$ ps.

According to [69], E_S in the steady-state is independent of τ, while in the transient regime, it varies approximately as $\sqrt{\tau}$. The points where the Raman gain becomes independent of τ are pointed out in Figure 5.6.

Appendix C

Equations of optical forces on a dielectric sphere

In this Appendix the equations used for calculating the optical forces on a dielectric microsphere in Chapter 6 will be presented. The equations are taken from References [80, 81]. The symbols for the various quantities are the same as the ones used in the references where these equations come from.

C.1 Equation of forces outside the fibre

C.1.1 The ray optics (RO) model

The model of Nemoto and Togo [80] follows the same basic arguments as [34, 85]. The axial radiation force $\mathrm{d}F_z(r,z)$ exerted on a unit surface $\mathrm{d}A$ of a dielectric particle inside a medium with refractive index n_1, around a point A with coordinates (r,z) from the beam waist centre, illuminated by a laser beam of intensity profile $I(r,z)$ will be (Figure C.1):

$$\mathrm{d}F_z(r,z) = \frac{n_1 I(r,z)}{c}\mathrm{d}A \ . \tag{C.1}$$

For a Gaussian laser beam, the axial force is given by integrating the above over the entire surface of the sphere:

$$F_z = \frac{4n_1P_0}{c}\int_0^{\tau}\left(\frac{a}{w}\right)^2 \exp\left(-\frac{2r^2}{w^2}\right) H(\theta)\mathrm{d}\theta \ , \tag{C.2}$$

with:

$$\begin{aligned}
H(\theta) &= \cos\alpha_1 \sin\theta\{\cos(\alpha_1-\theta)+R\cos(\alpha_1+\theta)-T^2[\cos(\alpha_1+\theta-2\alpha_2)+ \\
&\quad +R\cos(\alpha_1+\theta)]/(1+R^2+2R\cos 2\alpha_2)\} \ , && \text{(C.3)}\\
r &= a\sin\theta \ , && \text{(C.4)}\\
z &= d-a\cos\theta \ , && \text{(C.5)}\\
\alpha_1 &= \alpha+\theta \ , && \text{(C.6)}\\
\alpha_2 &= \sin^{-1}[(n_1/n_2)\sin\alpha_1] \ , && \text{(C.7)}\\
\alpha &= \sin^{-1}(r/\rho) \ , && \text{(C.8)}\\
w &= w_0[1+(\lambda z/\pi w_0^2)^2]^{1/2} \ , && \text{(C.9)}\\
\rho &= z[1+(\pi w_0^2/\lambda z)^2] \ , && \text{(C.10)}\\
R &= \{[\tan(\alpha_1-\alpha_2)/\tan(\alpha_1+\alpha_2)]^2+ \\
&\quad +[\sin(\alpha_1-\alpha_2)/\sin(\alpha_1+\alpha_2)]^2\}/2 \ , && \text{(C.11)}
\end{aligned}$$

with d the distance of the on-axis centre of the sphere from the beam waist, a the sphere radius, ρ the radius of curvature of the phase front that passes through point A, w_0 the beam waist size, R the average reflectance for p and s polarisations, $T \equiv 1-R$ the transmittance. τ is the maximum permissible value of θ.

In the present calculations the approximation $\tau = \pi/2$ was taken. The following values were used: $\lambda = 514.5$ nm, $P_0 = 80$ mW, $n_1 = 1$, $n_2 = 1.53$ and $a = 2.5$ μm.

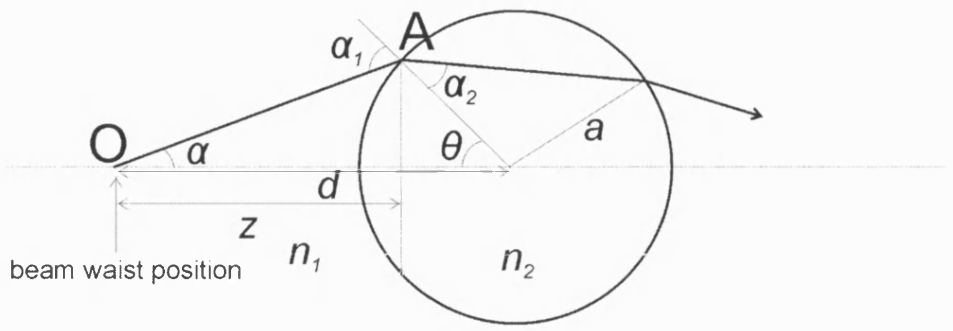

Figure C.1: Beam trajectory as it passes through the dielectric sphere in the RO model [80]

C.1.2 The enhanced RO model

Axial force

In the enhanced RO model of Gauthier and Wallace [81] the beam is regarded as a stream of photons and the laser power is correlated with the photon flux through the sphere, while the optical force is calculated from the momentum change of the refracted photons (Figure C.2). The equations for the axial force are:

$$F_z = F_{1rz} + F_{1tz} + F_{2rz} + F_{2tz}, \tag{C.12}$$

with

$$F_{1rz} = \int_0^{\pi/2} \frac{\pi}{c} n_0[1+\cos(2\theta_1)] I(\rho,z) \left|r_1\right|^2 R^2 \sin(2\theta_1) \mathrm{d}\theta_1 \ , \tag{C.13}$$

$$F_{1tz} = \int_0^{\pi/2} \frac{\pi}{c} [n_0 - n_s\cos(\theta_1-\theta_2)] I(\rho,z) \left|t_1\right|^2 R^2 \sin(2\theta_1) \mathrm{d}\theta_1 \ , \tag{C.14}$$

$$F_{2rz} = \int_0^{\pi/2} \frac{\pi}{c} n_s[\cos(\theta_1-\theta_2) + \cos(3\theta_2-\theta_1)] \times \\ \times I(\rho,z) \left|r_1\right|^2 \left|t_1\right|^2 R^2 \sin(2\theta_1) \mathrm{d}\theta_1 \ , \tag{C.15}$$

$$F_{2tz} = \int_0^{\pi/2} \frac{\pi}{c} \{n_s\cos(\theta_1-\theta_2) - n_0\cos[2(\theta_1-\theta_2)]\} \times \\ \times I(\rho,z) \left|r_1\right|^2 \left|t_1\right|^2 R^2 \sin(2\theta_1) \mathrm{d}\theta_1 \ . \tag{C.16}$$

Outside the fibre the intensity profile of the laser beam is the lowest-order Gaussian:

$$I(\rho,z) = \frac{P_0}{\pi w(z)^2} \exp\left[\frac{-2\rho}{w(z)^2}\right] \ , \tag{C.17}$$

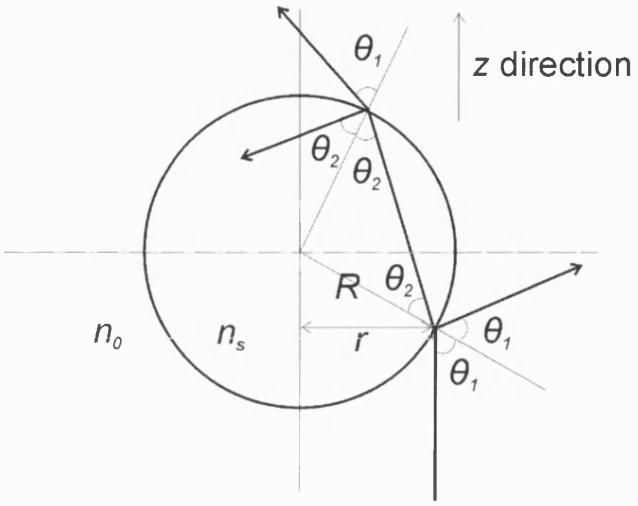

Figure C.2: Beam trajectory as it passes through the dielectric sphere in the enhanced RO model [81]

with ρ the radial distance from the beam's axis and $w(z)$ given by Equation C.9. $|r_1|^2$ is the power reflectance coefficient and is calculated from the Fresnel coefficients:

$$|r_1|^2 = \frac{(n_0 n_s)^2[\cos^2\theta_1 - \cos^2\theta_2]^2}{\{n_0 n_s[\cos^2\theta_1 + \cos^2\theta_2] + (n_0^2 + n_s^2)\cos\theta_1\cos\theta_2\}^2} \ , \tag{C.18}$$

and $|t_1|^2 = 1 - |r_1|^2$.

Gradient force

The gradient force is written as:

$$F_r = F_{1rr} + F_{1tr} + F_{2rr} + F_{2tr} \ , \tag{C.19}$$

where:

$$F_{1rr} = -\int_0^{\pi/2}\int_0^{2\pi} I(\rho,z)\frac{n_0}{2c}\sin(2\theta_1)\,|r_1|^2\,R^2\cos\phi\sin(2\theta_1)\mathrm{d}\phi\mathrm{d}\theta_1 \ , \tag{C.20}$$

$$F_{1tr} = \int_0^{\pi/2}\int_0^{2\pi} I(\rho,z)\frac{n_s}{2c}\sin(\theta_1-\theta_2)\,|t_1|^2\,R^2\cos\phi\sin(2\theta_1)\mathrm{d}\phi\mathrm{d}\theta_1 \ , \tag{C.21}$$

$$F_{2rr} = \int_0^{\pi/2}\int_0^{2\pi} I(\rho,z)\frac{n_s}{2c}[\sin(3\theta_2-\theta_1) - \sin(\theta_1-\theta_2)] \times \\ \times\,|r_1|^2\,|t_1|^2\,R^2\cos\phi\sin(2\theta_1)\mathrm{d}\phi\mathrm{d}\theta_1 \ , \tag{C.22}$$

$$F_{2tr} = \int_0^{\pi/2}\int_0^{2\pi} \frac{I(\rho,z)}{2c}\{n_0 \sin[2(\theta_1-\theta_2)] - n_s \sin(\theta_1-\theta_2)\} \times \\ \times |r_1|^2 |t_1|^2 R^2 \cos\phi \sin(2\theta_1) \mathrm{d}\phi \mathrm{d}\theta_1 \ . \quad \text{(C.23)}$$

ϕ is the angle between the direction of the radial momentum component and the radial direction of Figure C.2. In the general case in which the sphere is off the beam axis:

$$\rho(\theta_1,\phi) = (a^2 + R^2\sin^2\theta_1 + 2aR\sin\theta_1\cos\phi)^{1/2} \ , \quad \text{(C.24)}$$

where a is the offset between the maximum of the Gaussian beam profile and the sphere's central axis.

C.2 Forces inside the fibre

At the fibre entrance ($z = 0$), the beam profile is that of a diffractionless beam with profile:

$$I(\rho) = \frac{P_0}{\pi R_0^2} J_0^2\left(2.405\frac{\rho}{R_0}\right) \ , \quad \text{(C.25)}$$

where J_0 is the zero-order Bessel J function, R_0 is the fibre core radius and ρ is given by Equation C.24. Therefore the equations of the previous section had to be modified to account for the change in the beam profile. By substituting the above value of $I(\rho)$ in Equations C.12 and C.19 and integrating over the entire range of θ_1 and ϕ for both the axial and gradient force, the radial profile of the optical forces was calculated at the fibre entrance.

Appendix D

List of publications

D.1 Papers in journals

G. Antonopoulos, F. Benabid, T. A. Birks, D. M. Bird, J. C. Knight, and P. St. J. Russell. Experimental demonstration of the frequency shift of bandgaps in photonic crystal fibers due to refractive index scaling. Submitted to *Optics Express*, 2005.

F. Benabid, G. Antonopoulos, J. C. Knight, and P. St. J. Russell. Stokes amplification regimes in quasi-CW pumped hydrogen-filled hollow-core PCF. *Physical Review Letters* 95(21):213903-1-4, 2005.

F. Benabid, J. C. Knight, G. Antonopoulos, and P. St. J. Russell. Stimulated Raman scattering in hydrogen-filled hollow-core photonic crystal fiber. *Science*, 298:399402, 2002.

D.2 Publications in conferences

G. Antonopoulos, F. Benabid, J. C. Knight, and P. St. J. Russell. Efficient generation and tailoring of rotational SRS spectra generated in hydrogen-filled hollow-core photonic crystal fibre. In *PECS-VI, 6th International Symposium on*

Photonic and Electromagnetic Crystal Structures, Aghia Pelaghia, Crete, 2005.

F. Benabid, G. Antonopoulos, J. C. Knight, and P. St. J. Russell. Stokes amplification regimes in rotational SRS in hydrogen Gas filled hollow-core PCF pumped with quasi-cw pulses. In *Conference on Lasers and Electro-Optics*, Paper CTuJ3. Baltimore, 2005.

G. Antonopoulos, F. Benabid, T. A. Birks, D. M. Bird, G. Bouwmans, J. C. Knight, and P. St. J. Russell. Experimental demonstration of refractive index scaling in photonic bandgap fibers. In *Conference on Lasers and Electro-Optics*, Paper CThHH1. San Francisco, 2004.

G. Antonopoulos, F. Benabid, J. C. Knight, and P. St. J. Russell. Quasi-CW purely rotational stimulated Raman scattering in H_2-filled hollow-core photonic crystal fibre. In *POWAG 2004 Conference*, Bath, 2004.

G. Antonopoulos, F. Benabid, T. A. Birks, D. M. Bird, J. C. Knight, and P. St. J. Russell. Experimental demonstration of the bandgap shift in hollow-core photonic crystal fibres due to refractive index scaling. In *PREP2004 Conference* Paper OP7, pages 53-54, University of Hertfordshire, 2004.

F. Benabid, G. Antonopoulos, J. C. Knight, and P. St. J. Russell. Applications of hollow-core photonic crystal fiber. In *Conference on Lasers and Electro-Optics*, Baltimore, 2003.

F. Benabid, G. Antonopoulos, J. C. Knight, and P. St. J. Russell. Particle levitation and guidance in hollow-core photonic crystal fiber. In *Photonex*, 2002.

F. Benabid, G. Antonopoulos, J. C. Knight, and P. St. J. Russell. Particle levitation and guidance in hollow-core photonic crystal fibre. In *Photon02 Conference (Structured Optical Materials)*. Paper OP3a.6.4, page 92. Cardiff, 2002

References

[1] K. C. Kao and G. A. Hockham. Dielectric-fibre surface waveguides for optical frequencies. In *Proc. IEE*, 1966.

[2] P. St. J. Russell. Photonic crystal fibers. *Science*, 299:358–362, 2003.

[3] E. Yablonovitch. Inhibited spontaneous emission in solid-state physics and electronics. *Physical Review Letters*, 58(20):2059–2062, 1987.

[4] S. John. Strong localization of photons in certain disordered dielectric superlattices. *Physical Review Letters*, 58(23):2486–2489, 1987.

[5] P. R. Villeneuve and M. Piché. Photonic band gaps in two-dimensional square and hexagonal lattices. *Physical Review B*, 46(8):4969–4972, 1992.

[6] T. A. Birks, P. J. Roberts, P. St. J. Russell, D. M. Atkin, and T. J. Shepherd. Full 2-D photonic bandgaps in silica/air stuctures. *Electronics Letters*, 31(22):1941–1943, 1995.

[7] R. F. Cregan, B. J. Mangan, J. C. Knight, T. A. Birks, P. St. J. Russell, P. J. Roberts, and D. C. Allan. Single-mode photonic band gap guidance of light in air. *Science*, 285:1537–1539, 1999.

[8] B. J. Mangan, L. Farr, A. Langford, P. J. Roberts, D. P. Williams, F. Couny, M. Lawman, M. Mason, S.Coupland, R. Flea, H. Sabert, T. A. Birks, J. C. Knight, and P. St.J. Russell. Low loss (1.7 dB/km) hollow core photonic bandgap fiber. In *Optical Fiber Communication Conference*. Paper PDP24, 2004.

[9] F. Benabid, J. C. Knight, and P. St. J. Russell. Particle levitation and guidance in hollow-core photonic crystal fiber. *Optics Express*, 10(21):1195–1203, 2002.

[10] F. Benabid, G. Antonopoulos, J. C. Knight, and P. St. J. Russell. Particle levitation and guidance in hollow-core photonic crystal fibre. In *Photon02 Conference (Structured Optical Materials)*, page 92, Cardiff, 2002. Paper OP3a.6.4.

[11] F. Benabid, J. C. Knight, G. Antonopoulos, and P. St. J. Russell. Stimulated Raman scattering in hydrogen-filled hollow-core photonic crystal fiber. *Science*, 298:399–402, 2002.

[12] F. Benabid, G. Bouwmans, F. Couny, J. C. Knight, and P. St. J. Russell. Ultra-high efficiency laser wavelength conversion in a gas-filled hollow-core photonic crystal fiber by pure stimulated rotational Raman scattering in molecular hydrogen. *Physical Review Letters*, 93:123903–1–4, 2004.

[13] E. Hecht. *Optics*. Addison Wesley, NY, 4th edition, 2002.

[14] J. C. Knight, T. A. Birks, P. St. J. Russell, and D. M. Atkin. All-silica single-mode optical fiber with photonic crystal cladding. *Optics Letters*, 21:1547–1549, 1996.

[15] T. A. Birks, J. C. Knight, and P. St. J. Russell. Endlessly single-mode photonic crystal fiber. *Optics Letters*, 22(13):961–963, 1997.

[16] W.H. Reeves, J.C. Knight, P.St. J. Russell, and P.J. Roberts. Demonstration of ultra-flattened dispersion in photonic crystal fibers. *Optics Express*, 10(14):609–613, 2002.

[17] W. H. Reeves, D. V. Skryabin, F. Biancalana, J. C. Knight, P. St. J. Russell, F. G. Omenetto, A. Efimov, and A. J. Taylor. Transformation and control of ultra-short pulses in dispersion-engineered photonic crystal fibres. *Nature*, 424:511–515, 2003.

[18] A. Ortigosa-Blanch, J. C. Knight, W. J. Wadsworth, J. Arriaga, B. J. Mangan, T. A. Birks, and P. St. J. Russell. Highly birefringent photonic crystal fibers. *Optics Letters*, 25:1325–1327, 2002.

[19] W. J. Wadsworth, R. M. Percival, G. Bouwmans, J. C. Knight, T. A. Birks, T. D. Hedley, and P. St. J. Russell. Very high numerical aperture fibers. *IEEE Photonics Technology Letters*, 16(30):843–845, 2004.

[20] T. D. Hedley, D. M. Bird, F. Benabid, J. C. Knight, and P. St. J. Russell. Modelling a novel hollow-core photonic crystal fibre. In *Conference on Lasers and Electro-Optics*, Baltimore, 2003.

[21] J. M. Pottage, D. M. Bird, T. D. Hedley, T. A. Birks, J. C. Knight, and P. J. Roberts. Robust photonic band gaps for hollow core guidance in PCF made from high index glass. *Optics Express*, 11:2854–2861, 2003.

[22] E. A. J. Marcatili and R. A. Schmeltzer. Hollow metallic and dielectric waveguides for long distance optical transmission and lasers. *Bell System Technical Journal*, pages 1783–1809, 1964.

[23] F. Couny, H. Sabert, P. J. Roberts, D. P. Williams, A. Tomlinson, B. J. Mangan, J. C. Knight, T. A. Birks, and P. St. J. Russell. Visualizing the photonic band gap in hollow core photonic crystal fibers. *Optics Express*, 13(2):558–563, 2005.

[24] C. Kittel. *Introduction to Solid State Physics.* Wiley, New York, 1971.

[25] C. M. Smith, N. Venkataraman, M. T. Gallagher, D. Müller, J. A. West, N. F. Borrelli, D. C. Allan, and K. W. Koch. Low-loss hollow-core silica/air photonic bandgap fibre. *Nature*, 424:657–659, 2003.

[26] A. W. Snyder and J. D. Love. *Optical Waveguide Theory.* Chapman & Hall, 1983.

[27] G. P. Agrawal. *Nonlinear Fiber Optics.* Academic Press, 2001.

[28] A. Ghatak and K. Thyagarajan. *Introduction to Fiber Optics.* Cambridge University Press, 1998.

[29] F. Benabid and P.St. J. Russell. Hollow core photonic crystal fibers: a new regime for nonlinear optics and laser-induced guidance. In *International Conference on Transparent Optical Networks*, Invited Paper We.A2.1. Wraclow, 2004.

[30] P. J. Roberts, F. Couny, H. Sabert, B. J. Mangan, D. P. Williams, L. Farr, M. W. Mason, A. Tomlinson, T. A. Birks, J. C. Knight, and P. St.J. Russell. Ultimate low loss of hollow-core photonic crystal fibres. *Optics Express*, 13(1):236–244, 2005.

[31] P. Rabinowitz, A. Kaldor, R. Brickman, and W. Schmidt. Waveguide H_2 Raman laser. *Applied Optics*, 15:2005–2006, 1976.

[32] L. S. Meng, P. A. Roos, and J. L. Carlsten. Continuous-wave rotational Raman laser in H_2. *Optics Letters*, 27(14):1226–1228, 2002.

[33] J. K. Brasseur, K. S. Repasky, and J. L. Carlsten. Continuous-wave Raman laser in H_2. *Optics Letters*, 23(5):367–369, 1998.

[34] A. Ashkin. Acceleration and trapping of particles by radiation pressure. *Physical Review Letters*, 24(4):156–159, 1970.

[35] W. H. Wright, G. J. Sonek, Y. Tadir, and M. W. Berns. Laser trapping in cell biology. *IEEE Journal of Quantum Electronics*, 26:2148–2157, 1990.

[36] M. J. Renn, O. Vdovic, C. E. Wieman, D. Z. Anderson, and E. A. Cornell. Laser guidance and trapping of mesoscale particles in hollow-core optical fibers. *Physical Review Letters*, 82(7):1574–1577, 1999.

[37] M. J. Renn and R. Pastel. Particle manipulation and surface patterning by laser guidance. *Journal of Vacuum Science and Technology B*, 16(6):3859–3863, 1998.

[38] S. Chu, J. E. Bjorkholm, A. Ashkin, and A. Cable. Experimental observation of optically trapped atoms. *Physical Review Letters*, 57(3):314–317, 1986.

[39] G. Antonopoulos, F. Benabid, T. A. Birks, D. M. Bird, G. Bouwmans, J. C. Knight, and P. St. J. Russell. Experimental demonstration of refractive index scaling in photonic bandgap fibers. In *Conference on Lasers and Electro-Optics*, Paper CThHH1. San Francisco, 2004.

[40] G. Antonopoulos, F. Benabid, T. A. Birks, D. M. Bird, J. C. Knight, and P. St. J. Russell. Experimental demonstration of the bandgap shift in hollow-core photonic crystal fibres due to refractive index scaling. In *PREP2004 Conference*, pages 53–54, University of Hertfordshire, 2004. Paper OP7.

[41] T. A. Birks, D. M. Bird, T. D. Hedley, J. M. Pottage, and P. St. J. Russell. Scaling laws and vector effects in bandgap-guiding fibres. *Optics Express*, 12(1):69–74, 2003.

[42] J. D. Joannopoulos, R. D. Meade, and J. N. Winn. *Photonic Crystals.* Princeton University Press, 1995.

[43] J. Riished, J. Broeng, and A. Bjarklev. All silica photonic bandgap fiber. In *Conference on Lasers and Electro-Optics*, Paper CTuC5. Baltimore, 2003.

[44] R. T. Bise, R. S. Windeler, K. S. Kranz, C. Kerbage, B. J. Eggleton, and D. J. Trevor. Tunable photonic bandgap fiber. In *Optical Fiber Communication Conference*, pages 466–468, 2002.

[45] H. J. Pain. *The Physics of Vibrations and Waves.* John Wiley and Sons Ltd, 3rd edition, 1983.

[46] W. J. Wadsworth, N. Joly, J. C. Knight, T. A. Birks, F. Biancalana, and P. St. J. Russell. Supercontinuum and four-wave mixing with Q-switched pulses in endlessly single-mode photonic crystal fibres. *Optics Express*, 12(2):299–309, 2004.

[47] J. Riishede, N. A. Mortensen, and J. Laegsgaard. A poor man's approach to modelling micro-structured fibres. *Journal of Optics A: Pure and Applied Optics*, 5:534–538, 2003.

[48] F. Benabid, G. Antonopoulos, J. C. Knight, and P. St. J. Russell. Applications of hollow-core photonic crystal fiber. In *Conference on Lasers and Electro-Optics*, Baltimore, 2003.

[49] Y. R. Shen and N. Bloembergen. Theory of stimulated Brillouin and Raman scattering. *Physical Review*, 137(6A):1787–1805, 1965.

[50] M. Kalamiotou. *Introduction to Molecular Physics.* Lecture notes. Athens University Press, Athens, 1992.

[51] S. E. Harris and A. V. Sokolov. Broadband generation with refractive index control. *Physical Review A*, 55(6):4019–4022, 1997.

[52] S. E. Harris and A. V. Sokolov. Subfemtosecond pulse generation by molecular modulation. *Physical Review Letters*, 81(14):2894–2897, 1998.

[53] A. V. Sokolov, D. D. Yavuz, and S. E. Harris. Subfemtosecond pulse generation by rotational molecular modulation. *Optics Letters*, 24(8):557–559, 1999.

[54] R. W. Hellwarth. Theory of phase conjugation by stimulated scattering in a waveguide. *Journal of the Optical Society of America*, 8:1050–1056, 68 1978.

[55] V. Krylov, O. Ollikainen, U. P. Wild, A. Rebane, V. G. Bespalov, and D. I. Staselko. Femtosecond stimulated Raman scattering in pressurized gases in the ultraviolet and visible spectral ranges. *Journal of the Optical Society of America B*, 15(12):2910–2916, 1998.

[56] D. C. Hanna, D. J. Pointer, and D. J. Pratt. Stimulated Raman scattering of picosecond light pulses in hydrogen, deuterium and methane. *IEEE Journal of Quantum Electronics*, 22(2):332–336, 1986.

[57] K. Sentrayan, L. Major, A. Michael, and V. Kushawaha. Liquid nitrogen and room-temperature SRS gain in isotopic hydrogen molecules. *Journal of Physics D: Applied Physics*, 25:1697–1701, 1992.

[58] Y. R. Shen. *The Principles of Nonlinear Optics.* John Wiley and Sons Ltd, New York, 1984.

[59] P. L. Kelly. Self-focusing of optical beams. *Physical Review Letters*, 15(26):1005–1008, 1965.

[60] O. Rahn and M. Maier. Raman-limited beam diameters in the self-focusing of laser light. *Physical Review A*, 9(3):1427–1437, 1974.

[61] G. Tempea and T. Brabec. Theory of self-focusing in a hollow waveguide. *Optics Letters*, 23(10):762–764, 1998.

[62] G. Fibich and A. L. Gaeta. Critical power for self-focusing in bulk media and in hollow waveguides. *Optics Letters*, 25(5):335–337, 2000.

[63] F. Benabid, G. Antonopoulos, J. C. Knight, and P. St. J. Russell. Stokes amplification regimes in quasi-CW pumped hydrogen-filled hollow-core PCF. Accepted for publication in *Physical Review Letters*, 2005.

[64] G. Antonopoulos, F. Benabid, J. C. Knight, and P. St. J. Russell. Efficient generation and tailoring of rotational SRS spectra generated in hydrogen-filled hollow-core photonic crystal fibre. In *PECS-VI, 6th International Symposium on Photonic and Electromagnetic Crystal Structures*, Aghia Pelaghia, Crete, 2005.

[65] G. Antonopoulos, F. Benabid, J. C. Knight, and P. St. J. Russell. Quasi-CW purely rotational stimulated Raman scattering in H_2-filled hollow-core photonic crystal fibre. In *POWAG 2004 Conference*, Bath, 2004.

[66] R. W. Minck, E. E. Hagenlocker, and W. G. Rado. Stimulated pure rotational Raman scattering in deuterium. *Physical Review Letters*, 17(5):229–231, 1966.

[67] M. R. Perrone, V. Piccino, G. De Nunzio, and V. Nassisi. Dependence of rotational and vibrational Raman scattering on focusing geometry. *IEEE Journal of Quantum Electronics*, 33(6):938–944, 1997.

[68] F. De Tomasi, D. Diso, M. R. Perrone, and M. L. Protopapa. Stimulated rotational and vibrational Raman scattering by elliptical polarized pump radiation. *Physical Review A*, 64:023812–1–7, 2001.

[69] C.-S. Wang. Theory of stimulated Raman scattering. *Physical Review*, 182(2):482–494, 1969.

[70] M. G. Raymer and J. Mostowski. Stimulated Raman scattering: Unified treatment of spontaneous initiation and spatial propagation. *Physical Review A*, 24(4):1980–1993, 1981.

[71] R. J. Heeman and H. P. Godfried. Gain reduction measurements in transient stimulated Raman scattering. *IEEE Journal of Quantum Electronics*, 31(2):358–364, 1995.

[72] E. E. Hagenlocker, R. W. Minck, and W. G. Rado. Effects of phonon lifetime on stimulated optical scattering in gases. *Physical Review*, 154(2):226–234, 1967.

[73] R. L. Carman, F. Shimizu, C. S. Wang, and N. Bloembergen. Theory of Stokes pulse shapes in transient stimulated Raman scattering. *Physical Review A*, 2(1):60–72, 1970.

[74] S. A. Akhmanov, K. N. Drabovich, A. P. Sukhorukov, and A. S. Chirkin. Stimulated Raman scattering in a field of ultrashort light pulses. *Soviet Physics Journal of Experimental and Theoretical Physics*, 32(2):266–273, 1971.

[75] R. Holmes and A. Flusberg. Rotationally invariant theory of stimulated Raman scattering. *Physical Review A*, 37(5):1588–1596, 1988.

[76] R. L. Carman and M. E. Mack. Experimental investigation of transient stimulated Raman scattering in a linearly dispersionless medium. *Physical Review A*, 5(1):341–348, 1972.

[77] F. Benabid, G. Antonopoulos, J. C. Knight, and P. St. J. Russell. Particle levitation and guidance in hollow-core photonic crystal fiber. In *Photonex*, 2002.

[78] G. Gouesbet, B. Maheu, and G. Gréhan. Light scattering from a sphere arbitrarily located in a Gaussian beam, using a Bromwich formulation. *Journal of the Optical Society of America A*, 5(9):1427–1443, 1988.

[79] H. C. van de Hulst. *Light Scattering by Small Particles.* Dover Publications Inc., NY, 1981.

[80] S. Nemoto and H. Togo. Axial force acting on a dielectric sphere in a focused laser beam. *Applied Optics*, 37(27):6386–6394, 1998.

[81] R. C. Gauthier and S. Wallace. Optical levitation of spheres: analytical development and numerical computations. *Journal of the Optical Society of America B*, 12(9):1680–1686, 1995.

[82] M. J. Renn, E. A. Donley, E. A. Cornell, C. E. Wieman, and D. Z. Anderson. Evanescent-wave guiding of atoms in hollow optical fibers. *Physical Review A*, 53(2):648–651, 1996.

[83] D. J. Quesnel and D. S. Rimai. *Fundamentals of Particle Adhesion.* Global Press, 2001. Available through the Adhesion Society at adhesionsociety.org.

[84] J. Happel and H. Brenner. *Low Reynolds Number Hydrodynamics.* Prentice-Hall, Englewood Cliffs, NJ, 1965.

[85] A. Ashkin. Forces of a single-beam gradient laser trap on a dielectric sphere in the ray optics regime. *Biophysical Journal*, 61:569–582, 1992.

[86] R. Gómez-Medina, P. San José, A. García-Martín, M. Lester, M. Nieto-Vesperinas, and J. J. Sáenz. Resonant radiation pressure on neutral particles in a waveguide. *Physical Review Letters*, 86(19):4275–4277, 2001.

[87] A. Argyros, T. A. Birks, S. G. Leon-Saval, C. M. B. Cordeiro, F. Luan, and P. St.J. Russell. Photonic bandgap with an index step of one percent. *Optics Express*, 13(1):309–314, 2005.

[88] A. Rundquist, C. G. Durfee, Z. Chang, C. Herne, S. Backus, M. M. Murnane, and H. C. Kapteyn. Phase-matched generation of coherent soft x-rays. *Science*, 280:1412–1415, 1998.

[89] F. Benabid, F. Couny, J. C. Knight, T. A. Birks, and P. St. J. Russell. Compact, stable and efficient all-fibre gas cells using photonic crystal fibres. *Nature*, 434:488–491, 2005.

[90] M. H. Anderson, J. R. Ensher, M. R. Matthews, C. E. Wieman, and E. A. Cornell. Observation of Bose-Einstein condensation in dilute atomic vapor. *Science*, 269:198–201, 1995.

[91] C. C. Bradley, C. A. Sackett, J. J. Tollett, and R. G. Hulet. Evidence of Bose-Einstein condensation in an atomic gas with attractive interactions. *Physical Review Letters*, 75(9):1687–1691, 1995.

[92] K. B. Davis, M.-O. Mewes, M. R. Andrews, N. J. van Druten, D. S. Durfee, D. M. Kurn, and W. Ketterle. Bose-Einstein condensation in a gas of sodium atoms. *Physical Review Letters*, 75(22):3969–3973, 1995.

[93] P. N. Butcher and D. Cotter. *The Elements of Nonlinear Optics*. Cambridge University Press, Cambridge, 1991.